THÈSE

Pour obtenir le grade de

DOCTEUR DE L'UNIVERSITÉ GRENOBLE ALPES

Spécialité : **SIGNAL IMAGE PAROLE TELECOMS**

Arrêtée ministériel : 25 mai 2016

Présentée par

Eduardo Alejandro TUSA JUMBO

Thèse dirigée par **Jocelyn CHANUSSOT**
et codirigéee par **Jean-Matthieu MONNET, Mauro DALLA MURA et Jean-Baptiste BARRÉ**

préparée au sein du **INRAE de Grenoble, UR LESSEM et du GIPSA-LAB**
dans **l'École Doctorale: Électronique, Électrotechnique, Automatique et Traitement du Signal (EEATS)**

Apport de la fusion LiDAR - hyperspectral pour la caractérisation géométrique et radiométrique des arbres.

Fusion of 3D point clouds and hyperspectral data for the extraction of geometric and radiometric features of trees

Thèse soutenue publiquement le **"17 décembre 2020"**,
devant le jury composé de :

Mme. Florence TUPIN
Professeur, Télécom ParisTech, Présidente

Mme. Nesrine CHEHATA
Maître de Conférences, Bordeaux INP, EA GE, Rapportrice

Mme. Sylvie DURRIEU
Ingénieur HDR, INRAE, UR. TETIS, Rapportrice

Mr. Markus HOLLAUS
Maître de Conférences, Université Technologique de Vienne, Examinateur

Mr. Emmanuel TROUVÉ
Professeur, Université Savoie Mont-Blanc, Examinateur

Mr. Jocelyn CHANUSSOT
Professeur, Grenoble INP, GIPSA-LAB, Directeur de thèse

Mr. Jean-Matthieu MONNET
Ingénieur de recherche, INRAE UR. LESSEM, Co-Encadrant de thèse

Mr. Mauro DALLA MURA
Maître de Conférences, Grenoble INP, GIPSA-LAB, Co-Encadrant de thèse

Mr. Jean-Baptiste BARRÉ
Ingénieur de recherche, IGE Grenoble, Co-Encadrant de thèse

"Alva, Contardo, Karla, Fernanda, Santiago y Martin."

Acknowledgement

First of all, I would like to thank all the members of my committee, for having kindly accepted to evaluate my work. In the same line of work assessing, I would like to thank to Grégoire Vincent and Jean-Baptiste Féret for being part of my individual follow-up committee and for sharing their feedback every time that we were in touch. Also for welcoming me in Montpellier and let me work together with Anthony and Mélaine. I would also like to thank to Michael Dalponte on behalf of the Fondazione Mach, Italy, for replying my questions, for his close cooperation in my work and for sharing his valuable data.

I would like to express my profound gratitude to my supervisors Jocelyn, Jean-Matthieu, Mauro and Jean-Baptiste. Thank you very much for your support, your commitment, your patience, your time and your willingness with our research project and with me. Together with you and your great network of collaborators, I have learned different facets of research in remote sensing. Thanks for the meetings in GIPSA and INRAE, for the field trips in the mountainous forest and to host me every moment during my stay in France. I take this opportunity to thank LabEx OSUG@2020 for supporting my work through the Investissements d'avenir under Grant ANR10 LABX56.

Thank you to all the people in INRAE for your kind collaboration to work with me, especially Eric Mermin, Pascal Tardif, Sophie Labonne, Eric Maldonado, Giles Favier, Catherine Lukie, Laurent Borgniet, Franck Bourrier, Georges Kunstler, Frédéric Berger, Sylvain Dupier, David Toe, Nathaly Rolland, and also the heads of LESSEM, Emmanuelle George, Thomas Spiegelberger, Eric Perret. Thanks to my officemates for sharing the time to talk to me in any language: Nathalie Bertrand, Philomène Favier, Vivien Cros, Robin Mainieri. Thanks to my dear friends that I see every day in the hallways or the cafeteria: María Belén, Mithila, Taline, Manon, Lucas, Alice, Delphine, Grace, Laura, Nadège, Na, Nour, Cécile, Erwan; and also my friends in GIPSALAB: Mohamad, Daniele, Julien.

A big thank to my roommates in Grenoble: Oscar, Mathias, Qiangqiang, Camille. Thanks to my family for being in touch every single day since I have started this big personal challenge: my parents, my sisters, my nephews, my uncles, my aunts, my cousins.

Thanks to the Université Grenoble Alpes and the Universidad Técnica de Machala for being part of this great story.

Contents

1 Introduction

The main topic of this PhD is the fusion of 3D point cloud and hyperspectral data for the extraction of geometric and radiometric features of forest trees. In this introduction chapter, it is our main interest to explain the importance of studying forests by establishing the mutual influence with the environment and other life forms, including the human activities along the time. That would be the starting point to highlight the value of forests, in particular, mountain forests. We describe the contribution of the remote sensing technologies to improve the task of monitoring mountain forests at individual tree-level. We introduce independently the benefits and shortcomings of LiDAR and hyperspectral data, and how the integration of these two type of data can solve the characterization of individual trees. We will also give the details of the general organization of the manuscript by answering the proposed research questions.

Sommaire

1.1 Forest

Forests trees are the predominant terrestrial ecosystem that are distributed across the Earth. According to the Global Forest Resources Assessment report presented by the Food and Agriculture Organization of the United Nations (FAO) [1] in 2020, forest is defined as "*Land spanning more than* 0.5 *hectares with trees higher than* 5 *meters and a canopy cover of more than* 10%*, or trees able to reach these thresholds in situ. It does not include land that is predominantly under agricultural or urban land use*" [2]. The world has a total forest area of 4.06 billion hectares (*ha*), which represents 31% of the total land area [1,3].

Although forests are not distributed equally among the world's people or geographically, the forest area is equivalent to 0.52 *ha* per person. Almost half the forest area is relatively intact, and more than one-third is primary forest. Different ecozones at different latitudes and elevations are formed distinctly [1]. The tropical forest has the largest proportion of the world's forest area (45%) near the equator, followed by the boreal near the poles, temperate at mid-latitudes, and subtropical domains as it is illustrated in Figure 1.1. Higher elevation areas support forests similar to those at higher latitudes, and the precipitation also affects forest composition.

1.1.1 The ancient relationship between forest and climate

Forest trees have played an important role in our planet's life and environment evolution. The world's first trees dominated Earth in the Mid Devonian period, 393 - 383 million years ago [4,5]. Evidences from Catskill region near Cairo NY, USA, show extensive root systems containing the genus *Archaeopteris*, a group that has much more modern characteristics, with leaves and root systems comparable to subsequently dominant seed plants, such as spruces or pines. Paleontologist studies [6,7] point out that these trees formed the first forests that became crucial in absorbing carbon dioxide from the atmosphere, adding oxygen to the atmosphere, affecting the climate and influencing conditions that fostered the emergence of other life forms.

The Devonian Plant Hypothesis offers an explanation of environmental changes associated with the evolution of forest trees [8]. Climate changes and mass extinctions occurred during the late Devonian period due to the increase in plant material. This contributed to reducing global temperatures, and potentially caused short but intense periods of glaciation. *Archaeopteris* might have been able to form extensive forest ecosystems with properties such as 20 *m* height trunks and 1.6 *m* deep root systems. This suggests *Archaeopteris* influenced the ecology of late Devonian plant communities and Devonian landscapes, and probably played weathering role similar to present trees [4].

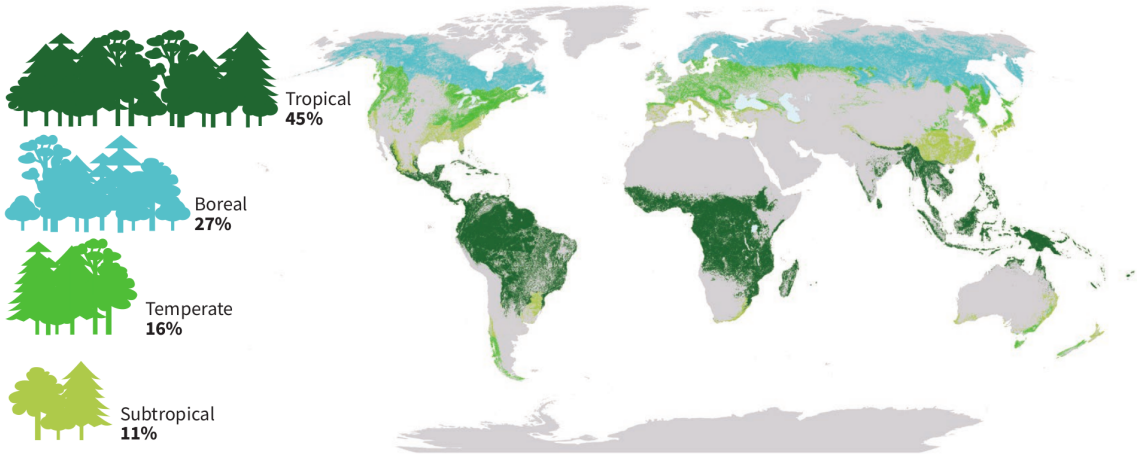

Figure 1.1: Proportion and distribution of global forest area by climatic domain, 2020 [1].

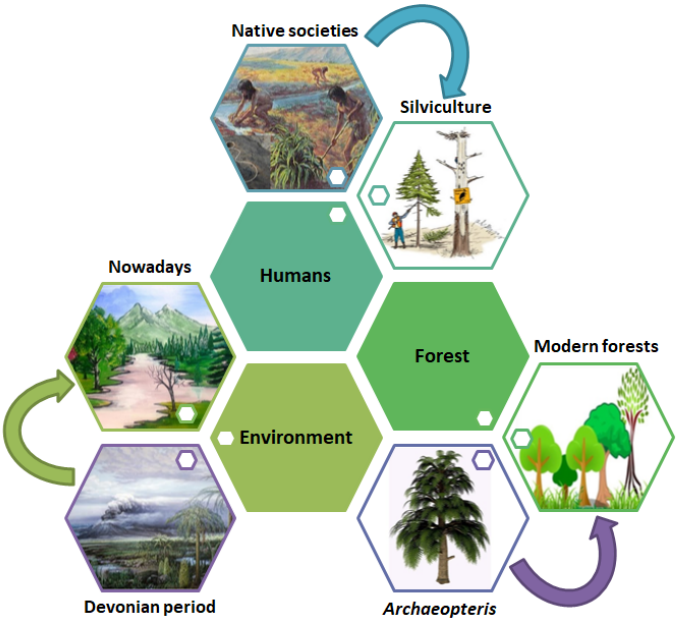

Figure 1.2: An ancient and close relationship: Archaeopteris, the ancestors of modern forests trees, influenced the environment of late Devonian period, which favored other life forms.

Nowadays, climate change is a topical issue discussed in the Paris agreement, where leaders committed to limit global temperature rise well below 2.0 degrees Celsius [9]. This agreement supports the UN-REDD program, which is a collaborative initiative from United Nations on reducing emissions from deforestation and forest degradation in developing countries [10]. It highlights the enormous need of sustainable management of forests by leveraging the tree benefits in temperature moderation, air purification, biodiversity preservation and reduction of noise pollution [11]. In this way, UN-REDD emphasizes the mitigation role of forest trees towards meeting up to a quarter of greenhouse gas emissions reductions up to 2030 [12] for preserving life on Earth. Figure 1.2 presents this ancient interaction among forest trees, the environment and the human activities.

1.1.2 The need for forest mapping and management

From ancient times, the encounter between humans and forest trees has been complex. Trees were tremendously relevant for almost all human activities: making clothes; providing food, fuel and fodder; constructing houses; making tools, weapons and wheels; providing shelter and shade [13]. Studies from the Amazon forests reveal that Brazil nut tree growth reflects human occupation intensity and management 400 years ago [14, 15]. When ancient humans constructed dwellings within the forest, they created gaps in the canopy, allowing for additional light to cultivate preferred species [15]. This confirms the influence of human populations and their management practices for plant domestication, plant dispersal, forest management, and landscape alteration since the time of native societies.

It is difficult to set up when forestry began. Agriculture and forestry initially evolved through practical experience with results strongly influenced by physical conditions and existing cultural, political, and economic factors. The roots of modern forestry and silviculture stem from developments in western Europe, from the late Middle Ages onward [16]. Forestry is defined as the science, art, and practice of creating, managing, using and conserving forests and associated resources for human benefit to achieve desired goals, needs and values [17]. A branch of forestry is silviculture, which is a field of study that deals with the knowledge and techniques used to establish and manipulate vegetation and to direct stand and tree development to create or maintain desired conditions [18].

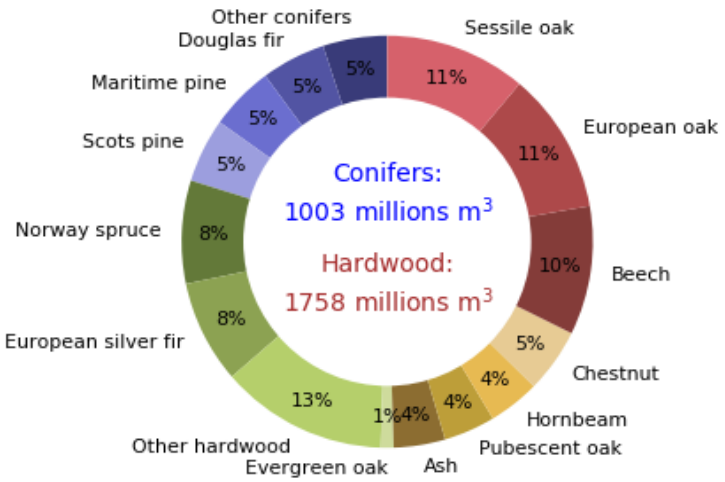

Figure 1.3: Distribution of wood volume per species at the national scale in France according to forest inventory memory released by the IGN (Institut national de l'information géographique et forestière) in 2019 [19].

Globally, about 1.15 billion *ha* of forest is managed primarily for the production of wood and non-wood forest products [1]. The wood volume provided from the mountain forests is 745 millions m^3, which is equivalent to 31% of the total area in France [20, 21]. The forest inventory of IGN [19] provides an estimation of the wood stock as it is presented in Figure 1.3. The volume per hectare, deciduous volume or conifer volume can be derived through extrapolation of field inventories. In the context of this project, mountain forests in metropolitan France call our attention for three reasons: it is an important source of wood, which is superior that the national average; it is a key element of the landscape, which is of enormous relevance for the inhabitants of these territories [22]; and it is a biodiversity area hosting numerous endangered species. In alpine areas, silviculture is mostly driven by large trees of certain species which value makes forest management economically sustainable [23]. The ability to identify and characterize those trees in very heterogeneous forests has great interest for forest operation planning [24].

Trees are renewable resources with an enormous impact to individuals and communities. From an industrial point of view, the need of determining wood quality becomes imperative for the serviceability of end products, and it is influenced by the forest management practices. Wood quality can be quantified [25], for instance, the quality of structural timber can be described by the stiffness, the straightness, and the stability; which are related to the wood density and driven by radial (pith-to-bark) and axial (top-to-bottom) variations in cell anatomical and chemical properties [26]. Therefore, the final price and quality of the wood are associated to the knots, intermode length and wood density. In fact, a good understanding of crown architecture can serve as a base to model the wood quality [27].

FAO [1] defines an individual tree as "*a woody perennial with a single main stem, or in the case of coppice with several stems, having a more or less definite crown*". Although this definition denotes a compositional and structural description, it does not consider quantitative aspects such as radiometric or geometric features. It reveals conceptual vagueness relative to an objective physical property [28], which is not precise for inventory purposes. This leads us to quantify a set of measurements in order to characterize trees, for instance: tree height, stem length, crown length, diameter at breast height, and crown area [29]. From these measurements, it is possible to estimate more complex tree variables such as above-ground biomass of trees [30, 31].

(a) Plot 3b (b) Plot 4

Figure 1.4: Forest inventory carried by the staff of INRAE (Institut national de recherche pour l'agriculture, l'alimentation et l'environnement) in the site of Chamrousse in summer 2018.

1.1.3 The scope of forest inventories

The purpose of ensuring sustainable forestry management requires to assess the current forest conditions, extent and quantity through inventory plots as we observe in Figure 1.4. Forest inventory is used to understand the development of forest trees by estimating means and totals for measures of forest characteristics over a defined area [32–34]. The possibility of monitoring individual tree architecture has great potential [35, 36]. For instance, information on tree crown 3D architecture will help researchers understand the mechanisms underlying competition and growth [37, 38]. Besides, the ability to monitor forest growth and mortality at the tree level will help forest managers to understand and then prevent the effects of climate change on stand dynamics.

Our understanding of the effect of competition on tree growth is mostly based on field diameter measurements [38]. Tree growth models are important tools to predict the development of each tree within a forest [39]. This type of models consists of diameter and height increment functions to forecast the growth and the mortality probability for each tree in a predefined time interval [40]. The tree growth is not independent of its neighbor's growth. There is a competition for performing photosynthesis and for accessing to the light and mineral nutrients. The link between the stand level and the individual tree level can be given by important competition variables described by the crown ratio and the open grown trees overlapping [41]. An accurate tree characterization provides relevant inputs to support these deterministic models. Such knowledge will help forest managers adapt their practices toward species mixture, which is often proposed as a way to improve forest resilience in the context of climate change [42], or different diameter structures [43].

In a field survey, forestry technicians collect data on the ground by applying sampling procedures [44]. Conventionally, systematic sampling is more efficient for representing land distribution. The sampling units may be stands, plots, strips or points; by having circular, rectangular or square plots [33, 44]. The size and the number of plots are defined according to the expected number of measurements, the parameters of interest and the statistical precision. However, field-based inventories are time-consuming and labor-intensive to be collected, providing rough estimates of stand attributes with typical limitations in the sampling because of terrain or vegetation factors [45]. Due to the large extensions of forest, measurements from the ground represent a real challenge for human intervention, involve important costs in employing measurement crews and provide a limited number of individual stands [30]. Remote sensing technologies are applied either for full-cover (entire area of interest) or sampling approaches (sample area). The advancements of remote sensing offer a faster and less expensive collection and analysis of georeferenced data [46] from ground-based, atmospheric and Earth-orbiting platforms [47] for large areas.

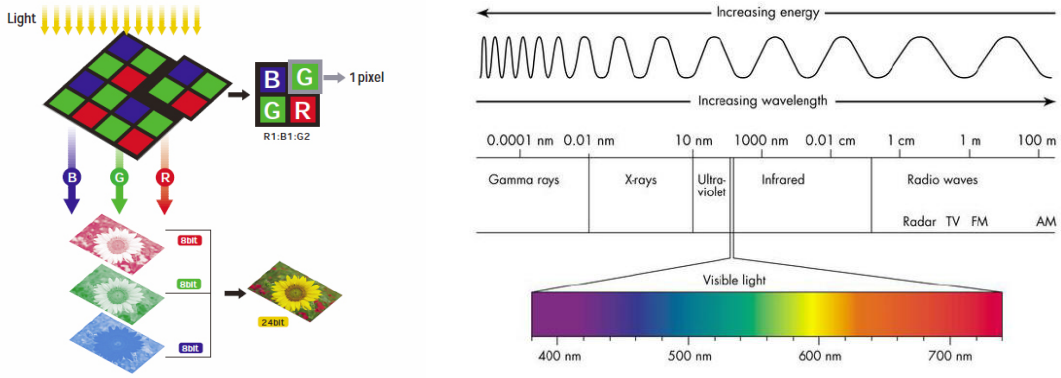

(a) The RGB color model involves the combination of red, blue and green bands from the visible spectrum.

(b) Electromagnetic spectrum of different ranges of energy described by the wavelength values [51].

Figure 1.5: (a) Illustration of the visual color perception model incorporated in the RGB cameras. (b) Description of the electromagnetic spectrum according to different ranges of energy characterized by the wavelength.

1.2 Principles of remote sensing

The remote sensing term was first conceived by Evelyn Pruitt of the US Office of Naval Research in the 1950s [48]. It is defined as the science of information acquisition concerning the Earth's surface without having contact with it [49,50]. This technology makes use of the properties of electromagnetic wave emitted, reflected or diffracted by the sensed objects [51]; for the purpose of processing, analyzing and employing this information [52]. The human visual perception is able to retrieve information in the visible light from the electromagnetic spectrum (see in Figure 1.5) in the range between 400 - 700 *nm*. The color information that we perceive, can be represented by combining the data that comes from three channels or bands: blue (B, 440 - 510 *nm* [53]), green (G, 540 - 560 *nm* [54]) and red (R, 630 - 685 *nm* [53]). In this way, RGB camera in Figure 1.5(a) combines the RGB bands for approaching our visual perception. The advantage of the instrumentation in remote sensing is these devices are designed to detect all other forms of electromagnetic energy beyond the visible light. For instance, it is possible to cover the infrared information in the range of 700 - 1000 *nm* of the electromagnetic spectrum in Figure 1.5(b).

Remote sensing instruments can be divided into two groups: passive and active sensors [50, 51]. Passive sensors use natural energy from the sun as a source of illumination. In this group, there are radiometers for measuring the intensity of electromagnetic radiation in select bands; and spectrometers, which are designed to detect, measure, and analyze the spectral content of reflected electromagnetic radiation [55, 56]. In a different manner, active sensors are characterized by providing their own source of illumination, and by measuring the energy that is reflected back. This group includes different types of radio detection and ranging (radar) sensors, altimeters, and scatterometers. The majority of active sensors operate in the microwave band of the electromagnetic spectrum, which gives them the ability to penetrate the atmosphere under most conditions [55, 56]. In forest monitoring, the main goal is to extract forest variables by taking advantage of the instruments carried aloft in spaceborne [57, 58] or airborne acquisitions such as Goddard's LiDAR, Hyperspectral and Thermal (G-LiHT), which provides an analytical framework for plant species composition, plant functional types, biodiversity, biomass and carbon stocks, and plant growth [59]. Following the remote sensing instrumentation, we review the principles of two types of technologies: hyperspectral imaging and LiDAR.

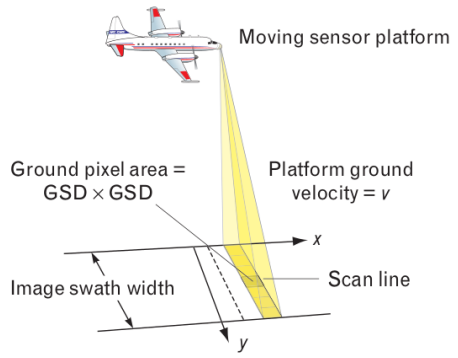

(a) A cross-track line recorded by a push-broom imaging sensor on the aircraft [64].

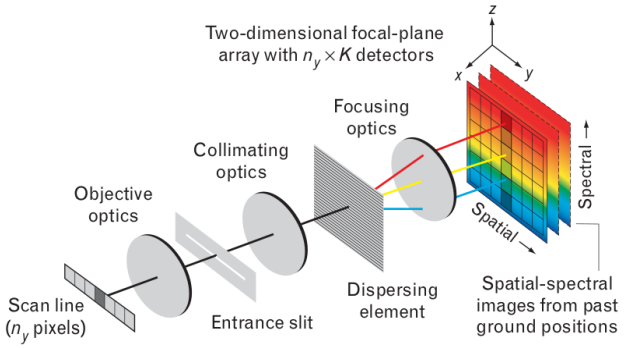

(b) Light dispersion onto a two-dimensional array of detectors in an imaging spectrometer [64].

Figure 1.6: Mechanism for hyperspectral data acquisition on the aircraft. (a) The geometry of the push-broom data-collection. (b) An imaging spectrometer disperses light onto a two-dimensional array of detectors.

1.2.1 Hyperspectral imaging

Hyperspectral imaging was first mentioned in the scientific community for discussing the results of imaging spectrometry in 1985 [60]. This passive remote sensing technology deals with the information extracted from objects or scenes lying on the Earth surface, by measuring the radiance acquired by airborne or spaceborne sensors [61] in hundreds of contiguous, registered, spectral bands [60]. A hyperspectral image is formed by two spatial dimensions and one spectral dimension [62]. Taking advantage of this information, we are able to monitor phenomena that could not be detected with a broadband imaging system [47]. We focus on those bands covering the visible, near-infrared, and shortwave infrared spectral bands in the range from 300 to 2500 *nm* [63].

Push-broom imaging sensor is a common format for hyperspectral data acquisition on the aircraft, as it is observed in Figure 1.6. A cross-track line of spatial pixels is decomposed into K spectral bands. The area coverage rate is the swath width times the platform ground velocity v. The area of a pixel on the ground is the square of the ground sample distance (GSD), as we see in Figure 1.6(a). The spectral decomposition is carried out by using any of several mechanisms, such as a diffraction grating or a wedge filter [64]. An imaging spectrometer disperses light onto a two-dimensional array of detectors. The spatial dimension contains n_y elements in the cross-track axis, and the spectral dimension is formed by K elements; by obtaining a total of $N = K \times n_y$ detectors, as it is represented in Figure 1.6(b).

For forestry purposes, hyperspectral data provides absorption features of the vegetation, which are associated to the biochemical attributes to estimate foliage components. In Figure 1.7, we show the mean spectral signatures of four main species of the Chamrousse site in the Northern Alpes, France. In addition to the RGB bands, another two important regions are identified from research studies: red-edge band in 690 - 710 *nm* [54] and near-infrared (NIR) in the range of 760 - 850 *nm* [53]. This information is relevant for forest applications [49, 65] for detecting plant stress [66], measuring chlorophyll content [54, 67–71], identifying small differences in percent of green vegetation cover [69, 72–76], discriminating land-cover types [77–80], sensing subtle variations in leaf pigment concentrations [54, 68, 69, 73, 81–83], improving the detection of changes in sparse vegetation, assessing absolute water content in leaves [73, 84], among others. In this context, spectral information collected from forests is sensitive to the complexity of the canopy structure, because of the disparate configuration of trees [85]. Foliage and branches may be interfered with background reflectance when interacting with incoming radiation, which introduces uncertainty in the measurements [86, 87]. Depending on the application, it is important to ensure

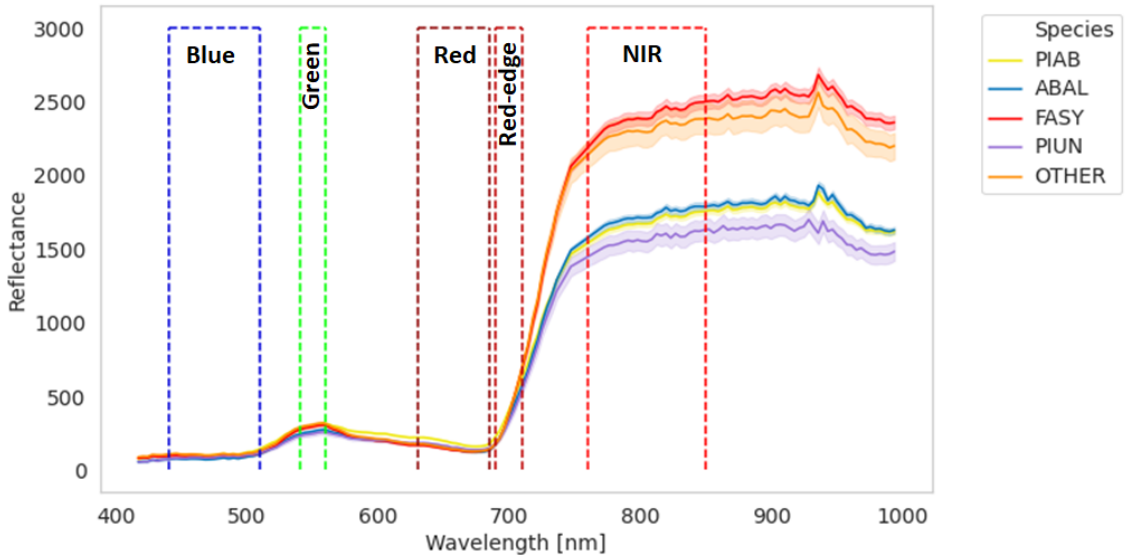

Figure 1.7: Mean spectral signatures of four main species located in the Chamrousse site, in the Northern Alpes, France: ● Abies alba (ABAL), ● Fagus sylvatica (FASY), ● Picea abies (PIAB), ● Pinus uncinata (PIUN) and ● "other" species. The spectral bands of blue, green, red, red-edge and NIR are higlighted in their respective ranges.

the most effective and efficient use of hyperspectral information. Data processing methods are concerned on extracting feature descriptors by identifying and removing the redundant bands [88]. In this thesis, the hyperspectral limitations are addressed by integrating complementary and independent information for exploring the vertical dimension of the canopy through the LiDAR data.

1.2.2 LiDAR

The laser technology was firstly approached by Charles Townes and Arthur Schawlow in Bell Labs in 1958 [89]. Among the innovative results of this emerging technology, a new generation of sensors and instruments are available nowadays. For instance, LiDAR technology has contributed in different applications such as: topographic mapping, flood risk assessments, watershed analysis, forestry modeling and analysis, habitat ecology, landslide investigation, 3D building modelling, road extraction and snow depth measurement [89–91]. LiDAR is an acronym for light detection and ranging [47]. The airborne LiDAR provides the explicit 3D coordinates (x, y, z) of a point cloud, return intensity, return number, number of returns, point classification, among other attributes [92]. In comparison with other remote sensing modalities, the depth measurement provided by airborne laser scanning (ALS) is clearly unique [47]. The term airborne laser is frequently associated to those systems that acquire LiDAR data from aircraft. The basis of all ALS systems is emission of a short-duration pulse of laser light and measurement of the elapsed time between emission and detection of the reflected light back at the sensor [62].

A common LiDAR system in Figure 1.8 consists of a laser scanner coupled with Global Positioning System and Inertial Navigation System (GPS/INS) navigation components, as a means of geo-referencing the position and orientation of the platform's movement [89, 93]. A wide swath is produced by the laser scanner mounted on the platform over which the distances to the mapped surface are measured [89]. The distances from the sensor to the mapped surface are computed by the time-of-flight between the laser pulse transmission and detection [90, 94]. Figure 1.8(a) shows the data acquisition for three scenarios. In the first scenario, the laser pulse creates three distinct echoes after hitting the canopy. A remaining fraction of the laser pulse hits the ground providing rise to a last echo. In the second scenario, the laser beam is reflected from a sloping surface, yield-

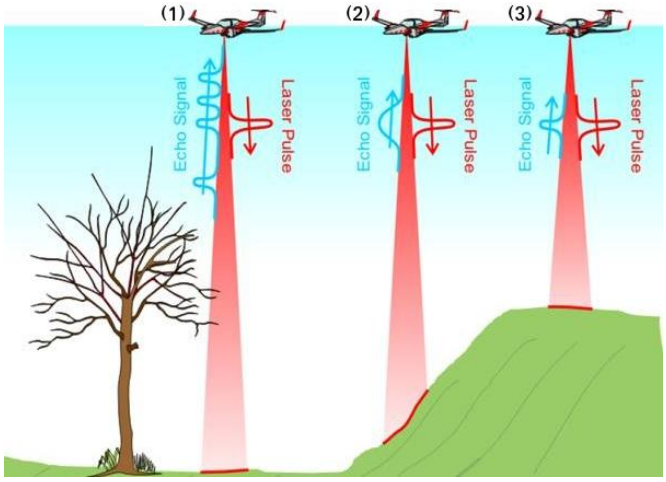

(a) (1) Laser pulse creates three distinct echoes from canopy. (2) The laser beam is reflected from a sloping surface. (3) The pulse is reflected from a flat surface [94].

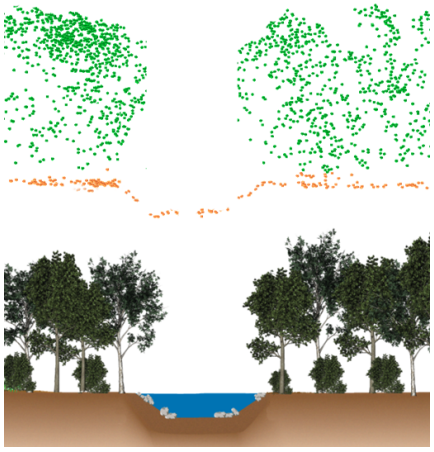

(b) Cross section showing LiDAR point cloud data (above) and the corresponding landscape profile (below).

Figure 1.8: (a) LiDAR data acquisition for three scenarios. (b) LiDAR point cloud profile visualization.

ing an extended echo pulse width. In the third scenario, the pulse is reflected from a flat surface, resulting in a single echo with a similar amplitude as of the outgoing laser pulse. Then all types of information are used in the post-processing in order to calculate the coordinates of the 3D point cloud as we observe in Figure 1.8(b).

LiDAR data is a useful tool to describe the 3D topographic profile of the Earth's surface, vegetation cover, and man-made objects [89], hence, the 3D structure of forest. In fact, LiDAR technology has provided outstanding results for estimating measurements of tree height [45, 95–98], canopy size [45, 96–98], and modeling [99], forest inventory [45, 95, 97], forest fuel modeling [100, 101], forest structure characterization [102], etc. Describing the forest at the tree level rather than with statistical point cloud metrics makes it easier to propose relevant conservation actions to forest managers. In the last years, decision makers benefited from available forest inventory approaches based on ALS [103]. The density improvement of ALS data collections makes the inventory more intuitive by applying individual tree crown (ITC) segmentation techniques [104]. However, the spectral and spatial information from LiDAR data is limited to describe general groups of species, for instance, conifers and broadleaves [85]. Then, the integration of LiDAR data with hyperspectral images can be more efficient for describing species composition.

1.3 Motivation

Forests have played a key role for the planet evolution, influencing all life forms and becoming primary source for supplying human needs. Therefore, it makes sense that these environments were tremendously affected over time. For instance, the forest cover in France decreased during the middle age as consequence of the intensity of land use, such as agriculture and human settlements [105]. The pressure on forest came to a maximum at the beginning of the industrial revolution before coal and oil were used as energy sources. Mining, glass making, brick making, and the metal working industries were dependent on wood or on charcoal made from wood [16].

Forest area has been increasing from now on, especially after the interruption of traditional farming practices [106]. The distance from core areas of economic and urban development produced agricultural land abandonment, mainly in remote areas, such as mountains; where agriculture is not economically sustainable [107, 108]. This goes hand in hand with the advancement of efficient policies oriented to lower fossil emissions by using forests, either as substitution for non-renewable sources or for carbon storage [109, 110].

Mountain forests provide environmental ecosystem services (EES) to communities: supplying of recreational landscapes [111], protection against natural hazards [112, 113], supporting biodiversity conservation [114], among others. Forest stands are also characterized by the species mixture and complex distribution of canopy structure [102]. In order to manage forests in such a way to balance and maintain those EES through space and time [112, 115], a good knowledge of the resource (location) is required.

Mountain forests stands are very heterogeneous and timber harvesting is really challenging in these areas due to the slope and terrain roughness [116]. As a consequence, timber harvesting is economically possible but for trees of higher value. This is why we are interested to map each tree and estimate its characteristics, including quality, which is related to its shape and growth conditions. Forest trees are well described by biophysical and biochemical parameters [85, 86]. For instance, the tree height, the crown length, the crown area, the crown radius, the diameter at breast height are biophysical descriptors of individual trees. The species composition at leaf level are characterized by the biochemistry of the foliage components, which can be described by the pigment concentration, the water content or the dry matter content [85].

Field inventories are not able to provide a wall to wall cover of detailed tree-level information on a large scale due to topography conditions in mountainous regions, which usually incur much higher expenses. On the other hand, remote sensing tools seem to be a promising technology characterized by the time efficient and the affordable costs for studying forests areas. For instance, LiDAR data provide detailed information from the vertical distribution and location of the trees [85, 86]. This makes it suitable for single tree detection and crown delineation [45, 96–98], from which is possible to derive biophysical parameters. However, single-wavelength measurements by LiDAR systems do not provide enough information for estimating biochemical properties, which limits the potential for mapping forest tree species [85, 86]. Hyperspectral data are associated to absorption features in the canopy reflectance spectrum, which generate abundant information for the characterization of tree species at pixel level [85]. However, the complexity of canopy structure and the illumination conditions influence the spectral measurements, beyond the limitations in exploring the vertical dimension and the spatial resolution.

The development of hyperspectral and LiDAR sensors has captured the attention of several scientific contributions that seek the fusion of this information with applications to sustainable management of forests for trees characterization. Hyperspectral and LiDAR systems provide independent and complementary data that are relevant for the assessment of biophysical and biochemical attributes of forested areas [85]. To go further, the following questions are addressed in this work. First, if the method to be used for data fusion is according to the variables to predict, *how data processing methods are applied in each level of data fusion for forest monitoring?* Within this purpose, different taxonomies have been proposed to group methods toward data fusion [87, 117, 118] for forest monitoring [119, 120].

The performance of these methods is associated to the spatial and spectral resolution of the remote sensing data. LiDAR data acquisitions of high spatial resolution provide the conditions to delineate individual trees with high accuracy. Then, if we consider the shape and the size of individual trees, *how a crown shape model can improve the segmentation of individual tree crowns?* Finally, if LiDAR and hyperspectral data can be used to estimate biophysical and biochemical parameters, *which combination of feature sets contribute to characterize the forest tree species composition?* The purpose of this thesis is to answer these three questions by reviewing and exploring unsupervised and supervised machine learning techniques (Figure 1.9).

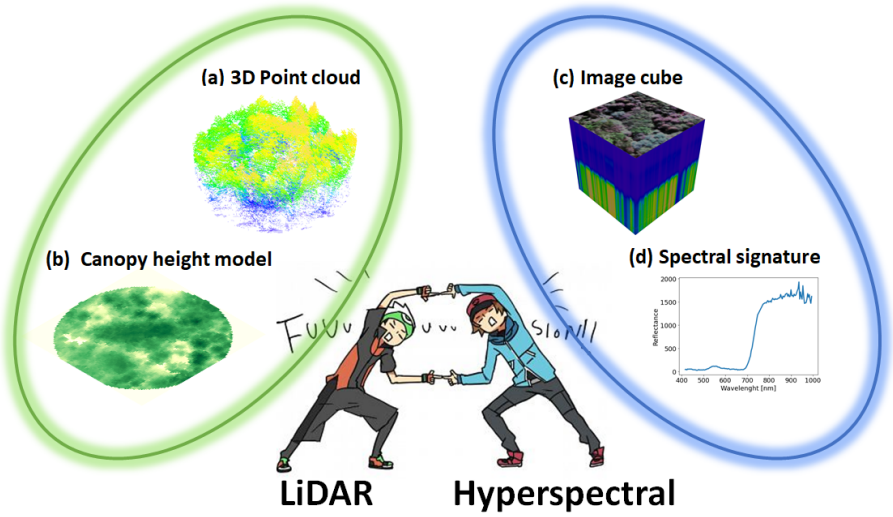

Figure 1.9: Data fusion of LiDAR and hyperspectral data: (a) 3D point cloud from LiDAR data. (b) 2D LiDAR representation in the canopy height model. (c) Image cube representation of all the bands in the hyperspectral image. (d) Spectral signature of a pixel in the hyperspectral image.

To answer the first question, a literature review of data fusion of LiDAR and hyperspectral data for forest monitoring, has been organized in different methods and levels. Most of the authors converge at three levels of data representation [87, 117–120]: low level or observation level, medium level or feature level, and high level or decision level. The first level consists of the integration of reflectance information and the coordinates of LiDAR points for alignment [117]. Although, the output of this level of fusion by itself does not provide explicit information for forest application, the corrected data reduces geometric and radiometric distortions. The second level is about the extraction of feature descriptors to form a new set of data representation [117]. At this level of fusion, a new feature set derived from the LiDAR and hyperspectral data, can provide more consistent and discriminatory information to establish relationships with forest tree composition. The majority of fusion schemes reaches the decision level, in which each modality is processed independently to develop rule-based models [117–119]. Several studies use the supervised methods to integrate features from different remote sensing modalities for species mapping [69, 121–135], the estimation of functional, physiological [54, 73, 136–149] and structural attributes [150–158], above-ground biomass and carbon density [74, 159–162], and land cover maps [77–80].

Airborne data vendors provide remote sensing acquisitions processed at low level fusion by applying geometric and radiometric corrections [77], and by exploiting the high spatial resolution of LiDAR data. In fact, if LiDAR technology can describe in detail the canopy vertical distribution [85], it seems consistent to use these data to answer the second question, *how a crown shape model can improve the segmentation of individual tree crowns?* In several studies, the individual tree crown (ITC) delineation can be posed as a 3D segmentation approach using a LiDAR point cloud [163]. Studies for automatic segmentation of trees [96, 97] extract tree crown shape information by using allometric equations in order to estimate the parameters of the algorithms. We propose a new framework for ITC delineation by introducing a crown shape model [164]. A proper ITC delineation provides accurate estimation of the crown architecture given by the tree height, the crown area, the crown radius and the crown height [45, 96–98]. In addition to that, the information obtained from the ITC delineation can serve as an input for later stages of processing LiDAR and hyperspectral data at decision level fusion, such as tree species classification [159, 165].

To answer the third question, *which combination of feature sets contribute to characterize the forest tree species composition?*, we focus on the data fusion at medium and high level. At medium level, we proceed to extract feature descriptors from each modality [69, 130, 132, 135]. Features

can be computed at point, pixel and object (tree) level. Dechesne *et al*. [165] suggest to rasterize the point features from LiDAR data in order to be aligned with the hyperspectral grid. From the hyperspectral data, we extract vegetation indices that has been demonstrated in other studies to characterize forest tree species [69, 74, 76]. We propose an approach for selecting features that produce a better forest tree species classification. The present dissertation contributes to the understanding of forest characteristics by exploiting hyperspectral images and LiDAR data, by combining these two modalities to derive tree species composition within a heterogeneous canopy of a mixed forest.

1.4 Objectives

In this thesis, we present the integration of remotely sensed data for the analysis of forest areas. In particular, we focus our attention on hyperspectral and LiDAR data that are of primary importance in the study of forest areas. Our attention is also devoted to the use of unsupervised and supervised machine learning techniques for the use of the information contained in such data acquired over forest areas. To summarize, the thesis objectives answer the three scientific challenges described in Section 1.3, more specifically, we address the following questions:

- *Q1. How data processing methods are applied in each level of data fusion for forest monitoring?*

  The last review of data fusion for forest monitoring was carried in 2014 [87]. Since then, new contributions have emerged to tackle this problem [166, 167]. We propose a literature review on the integration of hyperspectral imaging and LiDAR data by grouping data processing methods in general process at each level of data fusion, by illustrating the potential relationships found in these studies. Although different authors propose a variety of taxonomies for data fusion, we classified our reviewed methods according to three levels: low level or observation level, medium level or feature level, and high level or decision level. This review examines the relationship between the three levels of fusion and the methods used in each considered approach. A set of 50 contributions oriented to forest monitoring applications that combines hyperspectral images and LiDAR data at different levels of fusion are reviewed. This work was published in the book series "Data Handling in Science and Technology" in January 2020 and the work is presented in Chapter 2:

  TUSA, E., LAYBROS, A., MONNET, J. M., DALLA MURA, M., BARRÉ, J. B., VINCENT, G., DALPONTE, M., FÉRET, J. B. CHANUSSOT, J. (2020). FUSION OF HYPERSPECTRAL IMAGING AND LIDAR FOR FOREST MONITORING. IN *Data Handling in Science and Technology* (VOL. 32, PP. 281-303). ELSEVIER.

- *Q2. How a crown shape model can improve the segmentation of individual tree crowns?*

  Ferraz *et al*. [96, 97] proposed the adaptive 3D mean shift (AMS3D) for ITC delineation. This approach is based on adaptive kernel size that is suitable for tropical forests, but it could lead to an undersegmentation effect by merging adjacent coniferous tree crowns. We present an AMS3D approach based on the adaptation of the kernel profile size through an ellipsoid crown shape model, which fits the coniferous tree crowns that are present in temperate forests. The algorithm parameters are estimated based on allometry equations derived from 22 forest plots in two study sites described in Chapter 3. The ellipsoid crown shape model with a superellipsoid (SE) kernel profile of n = 1.5 presents the highest recall and the best Jaccard index, especially for conifers. This work was published in the journal "IEEE Geoscience and Remote Sensing Letters" in August 2020 and it is presented in Chapter 4:

TUSA, E., MONNET, J. M., BARRÉ, J. B., DALLA MURA, M., DALPONTE, M., CHANUSSOT, J. (2020). INDIVIDUAL TREE SEGMENTATION BASED ON MEAN SHIFT AND CROWN SHAPE MODEL FOR TEMPERATE FOREST. *IEEE Geoscience and Remote Sensing Letters*.

- *Q3. Which combination of feature sets contribute to characterize the forest tree species composition?*

  We aim to investigate the integration of feature descriptors from HI and LiDAR by using the intra-set and inter-set feature importance by using random forest (RF) score and 5-fold cross validation. We consider the following feature sets: 160 hyperspectral bands (HI), 61 vegetation indices detailed in chapter 2, the principal components (PC) obtained by using robust PCA (rPCA) [127] from HI, 72 LiDAR features explained in [165], and their PC by using rPCA. Previously, the dataset is created from the field inventory information by projecting the tree crowns, by selecting the non-overlapping pixels and by removing pixels associated to non-vegetation, low objects and shadow. RF is aplied for the feature classification [76]. The overall accuracy of tree species classification at pixel-level was 78.1%. Our approach showed that 78.3% of trees were correctly assigned overall, by having conifers such as Norway Spruce (*Picea abies*) and mountain pine (*Pinus uncinata*) with producer's accuracies above 90%. This approach was presented in the conference "XXIV International Society for Photogrammetry and Remote Sensing (ISPRS) Congress" in August 2020 and the work is detailed in Chapter 5:

  TUSA, E., MONNET, J. M., BARRÉ, ,J.B., M, D. M., CHANUSSOT, J. (2020). FUSION OF LIDAR AND HYPERSPECTRAL DATA FOR SEMANTIC SEGMENTATION OF FOREST TREE SPECIES. *Int. Arch. Photogramm. Remote Sens. Spatial Inf. Sci., XLIII-B3-2020, 487–494, 2020*. DOI:HTTP://DX.DOI.ORG/10.5194/ISPRS-ARCHIVES-XLIII-B3-2020-487-2020

1.5 Thesis structure

This work is divided in 6 chapters:

- Chapter 2 presents and discusses the existing methods for data fusion by defining three levels: low- or observation-level, medium- or feature-level and high- or decision level. Different forest monitoring applications are reviewed according to these levels of fusion.
- Chapter 3 describes the datasets used for the algorithm assessment: the study areas composition, the field data procedures and instruments, and the specifications of the remote sensing instruments.
- Chapter 4 presents the ITC delineation method based on 3-D Adaptive Mean Shift (AMS3D) and the ellipsoid crown shape model by adapting the kernel and the influence for detecting conifers and broadleaves.
- Chapter 5 explains the tree species classification approach for the integration of LiDAR and hyperspectral information, by selecting feature descriptors and by transforming feature sets into a new feature space.
- Chapter 6 presents conclusions and perspectives for this thesis.

2
Data Fusion

Hyperspectral data contains meaningful reflectance attributes of plants or spectral traits, while LiDAR data offers alternatives for analyzing structural properties of canopy. The fusion of these two data sources can improve forest characterization. The method to use for the data fusion should be chosen according to the variables to predict. This chapter presents a literature review on the integration of hyperspectral imaging and LiDAR data by considering applications related to forest monitoring. Although different authors propose a variety of taxonomies for data fusion, we classified our reviewed methods according to three levels of fusion: low level or observation level, medium level or feature level, and high level or decision level. This review examines the relationship between the three levels of fusion and the methods used in each considered approach.

Sommaire

2.1 Principles of fusion

As we mentioned in chapter 1, LiDAR data provide detailed geometric information, which makes it suitable for single tree detection and crown delineation [45, 96–98]. However, single-wavelength measurements by LiDAR systems is not enough for estimating biochemical properties, which is meaningful for mapping forest tree species [86]. At the same time, hyperspectral data describe a bi-dimensional representation of absorption features in the canopy reflectance spectrum, which allows the characterization of tree species at pixel level. However, the spectral measurements are sensitive to the complexity of the canopy structure and the illumination conditions [85].

The purpose of integrating remote sensing modalities is to achieve fused data from information of different spatial, spectral and temporal resolutions [118]. The output of the integration of these complementary and independent data is more refined, more robust and more accurate than individual data sources [117]. In this manner, data fusion improves the quality of information for decision making, by benefiting from the development of hyperspectral and LiDAR sensors. The problem of data fusion has captured the attention of several scientific contributions that seek for applications of main interest for sustainable management of forests: from trees to stand characterization [119, 120, 124].

Data fusion [117, 118, 168] gathers a group of methods and approaches that combines multiple sources of data. Particularly, different categories have been proposed to describe the fusion of hyperspectral images and other remote sensing modalities [117, 118], such as LiDAR data for forest monitoring [119, 120, 124]. Table 2.1 summarizes the main fusion categories considered in different studies: domain, resolution, nature of images, methods and data processing. Focusing on our interest of data processing, all the authors converges at three level of data representation defined clearly by Dechesne [165] as follows: low level or observation level, medium level or feature level, and high level or decision level. In this chapter, these three categories are going to be studied according to our literature review on data fusion for forest applications.

Table 2.1: Fusion categories (domain, resolution, nature of images, method and processing) described by levels proposed by five different authors. For data processing, three levels are defined: low level or observation level, medium level or feature level, and high level or decision level.

<table>
<tr><td rowspan="2">Categories</td><td colspan="4">Authors</td></tr>
<tr><td>Chaudhuri et al. [117]</td><td>Kandare [120] and Torabzadeh et al. [124]</td><td>Pohl et al. [118, 168]</td><td>Dechesne [119]</td></tr>
<tr><td rowspan="2">Domain</td><td>Spatial</td><td rowspan="4"></td><td rowspan="4"></td><td rowspan="5"></td></tr>
<tr><td>Frequency</td></tr>
<tr><td>Resolution</td><td>Pan-sharpening</td></tr>
<tr><td>Nature of images</td><td>Multimodal image fusion</td></tr>
<tr><td rowspan="3">Method</td><td rowspan="3"></td><td>Empirical or statistical</td><td rowspan="2"></td></tr>
<tr><td>Physical</td></tr>
<tr><td colspan="2">Hybrid</td></tr>
<tr><td rowspan="4">Processing</td><td rowspan="2">Pixel or signal</td><td rowspan="2">Data</td><td>Subpixel</td><td rowspan="2">Observation</td></tr>
<tr><td>Pixel</td></tr>
<tr><td>Feature or region</td><td>Product</td><td colspan="2">Feature</td></tr>
<tr><td>Decision or symbolic</td><td>Multilevel</td><td colspan="2">Decision</td></tr>
</table>

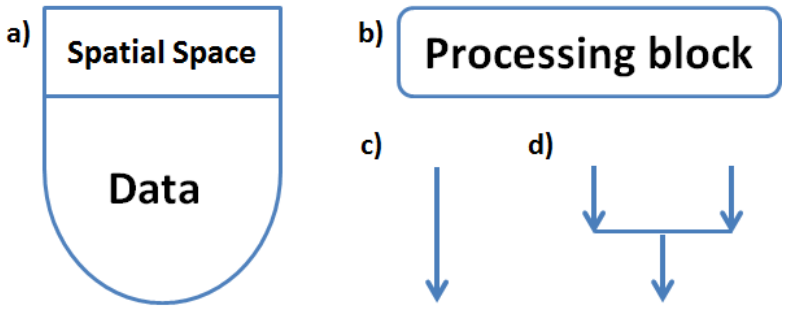

Figure 2.1: Graphical representation of processes for ilustrating fusion methods: a) Unit of data symbolizes the spatial space and the type of information. b) A block expresses the task for processing data and information. c) Interaction arrow for representing the inputs and outputs of processing blocks. d) Input simultaneity to a processing block

For each level of fusion, diagrams that describe interactions among processes and their inputs and outputs, illustrate the processes involved at each level. Units of data are represented in Figure 2.1 a), for clarifying how data evolves through every processing task. Every unit of data describe the type of information: spectral bands, height, feature, and so on; and also, the spatial space in which this information is represented: point level, pixel level, region level and object level. Additionally, a block represents tasks for processing data and information as it is observed in Figure 2.1 b), and finally, the arrows in Figure 2.1 c) and d) depict the interactions between these units of data and processes.

2.2 Low-level

This level is the most basic and fundamental fusion for understanding and processing the data [117]. It corresponds to the fusion of the reflectance of hyperspectral images and the coordinates of LiDAR point cloud [119]. This level of fusion preserves most of the original information [118]. In Figure 2.2, we describe processes for geometric and radiometric correction.

2.2.1 Geometric correction

Geometric correction is concerned with placing spectral information in their proper planimetric (x, y) map location so it can be associated with other spatial information [169]. This task involves different data fusion processes. Some studies correct distortions from the point cloud coordinates by using real world coordinates pixels [154] or by direct georeferencing [130]. Geometric correction algorithms are implemented in several computational packages: *Tiff* [144], *CaliGeo* available in *ENVI* [160], and *HyperspecIII* software [131, 133]. In this review, we are concerned about three types of geometric correction: orthorectification, co-registration and back projection.

Before explaining the geometric correction processes, it is imperative to define the canopy height model (CHM), which is the most common raster representation of LiDAR data for fusion at this level. CHM can be created in different ways. First, the point cloud is classified as ground and vegetation points by using the *TerraScan* software [159, 170]. Then, the digital terrain model (DTM) is derived from the ground points, and the digital surface model (DSM) from all the points. The CHM is simply computed by subtracting the DTM from the DSM. A second approach is based on the creation of a terrain surface, which is not necessarily a DTM; for instance, a TIN surface.

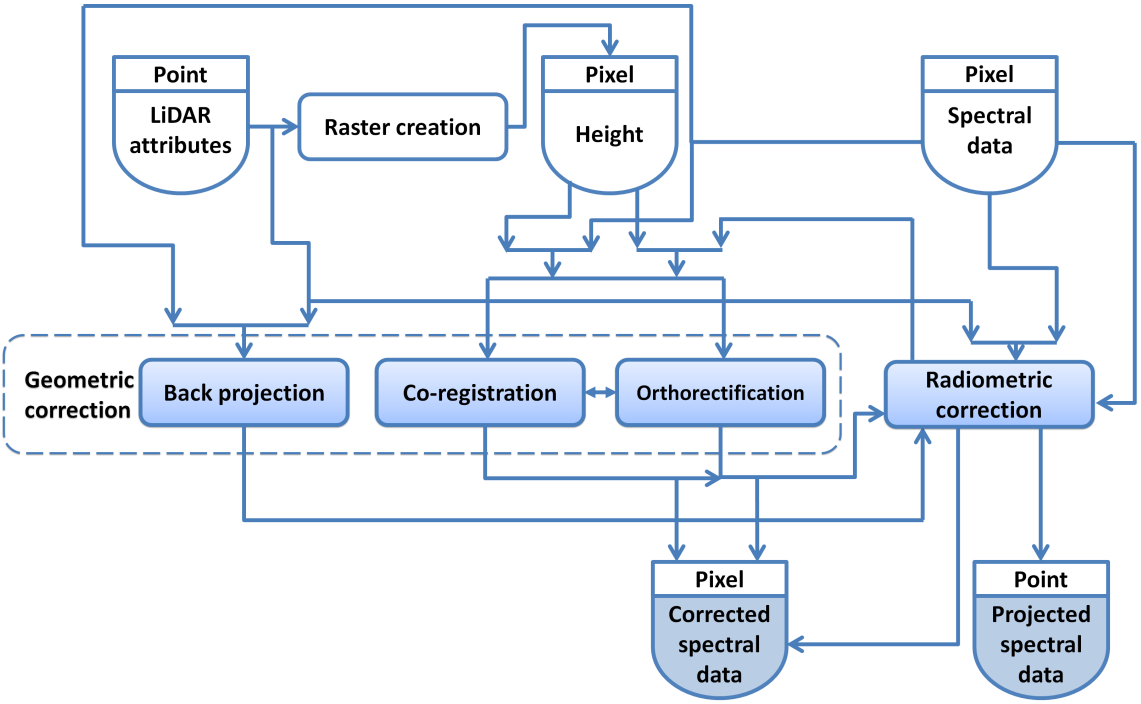

Figure 2.2: Illustration of fusion at low level or observation level

Then, the point cloud is normalized to compute directly a CHM that can be slightly lower than the one obtained in the first approach. Several studies prefer the use of specific softwares for creating the CHM: *Tiff* [156, 171], *TerraScan* [128, 151, 152], *FUSION* [139, 172], *eCognition* [129], *LAStools* [78, 158]. When CHM contains empty pixels called "pits", the R package *lidR* [173] implements a pit-free algorithm for *LAStools* following the method proposed by [174]. Additionally, CHM is used to threshold forest from forest gaps and low canopy heights [80, 126], or for establishing a framework for extraction of features [122].

The processes of orthorectification and co-registration can be applied separately or integrated as a workflow. Orthorectification is the process of geometrically adjusting the hyperspectral image to an orthogonal image (DSM) by transforming coordinates from the image space to the ground space and removing tilt and relief displacement, for creating a planimetrically correct image [169, 175]. Usually, remote sensing images are orthorectified and georeferenced before being sent to users. Sometimes these procedures are not accurate enough to identify individual trees. Co-registration methods for remote sensing datasets of wooded landscapes can improve the results [77]. For instance, the *AROP* package performs automated precise registration and orthorectification [176].

Co-registration is the translation and rotation alignment process in order to obtain a registered hyperspectral image by considering the LiDAR-derived DSM as reference [169]. This task has demonstrated the effectiveness and potentialities for decision-level process such pixel classification [177]. The process of co-registration of two image modalities requires the use of ground control points (GCP) [121]. Shen et al. [69] apply the nearest-neighbor interpolation by using more than 30 GCP with an accuracy of 0.25 m. Alonzo et al. [123, 137] use Delaunay triangulation with 137 GCP. Alternatively, other approaches do not require GCP for the registration process. For instance, the NGF-Curv algorithm proposed by Refs. [77, 127, 156] is based on the minimization of an objective function that contains similarity and regularization terms. NGF-Curv algorithm is implemented in the image registration software package called *FAIR* [178]. A second approach that avoids GCP is implemented in the *GeFolki* package [179], which is based on a local method of optical flow derived from the Lucas-Kanade algorithm, with a multiscale implementation, and

a specific filtering including rank filtering. The disadvantage of the registration methods without GCP is these are biased by shading effects, which are present in mountainous forest.

Back projection of LiDAR point cloud onto the image plane allows a better co-alignment than the image orthorectification with the CHM because of altitude distortions associated with the irregular porous surface of forest canopy. Back projection was implemented by Brell et al. [180] on hyperspectral imagery, by improving the geometric alignment between the hyperspectral images and LiDAR data. Alternatively, the process of spectral projection onto the 3D point cloud is implemented by Asner et al. [134], through a sun-canopy ray tracing for sunlit. In this way, LiDAR data with known solar position provided 3D maps of illumination geometry for each canopy.

2.2.2 Radiometric correction

The radiometric correction aims at converting radiance values of hyperspectral images into reflectance [169]. In the forest monitoring applications, authors do not establish a strict sequence for applying radiometric correction. In some studies, images are atmospherically corrected before co-registration by using the Atmospheric and Topographic Correction software *ATCOR-4*, which implements the radiative transfer model *MODTRAN* [54, 77, 123, 130, 132, 136, 137, 142, 144, 148, 154, 160]. Another task based on *MODTRAN* model for minimizing atmospheric effects, it is implemented in the Fast Line-of-Sight Atmospheric Analysis of Spectral Hypercubes, *FLAASH* algorithm, which is available in the image analysis software *ENVI* [74, 122, 128, 135, 143, 181]. Alternatively, the model *ACORN* is used to improve aerosol correction [78, 145–147, 149]. Additionally, there are other algorithms implemented in *SpectralView* [131, 133] or *QUAC* [73] for these correction purposes.

Another strategy for radiometric correction is implemented through normalization algorithms. For instance, the value of each pixel was normalized with respect to the sum of the original values of the same pixel in all the bands, by resulting in a significant improvement of the final classification accuracies [159]. This relative radiometric normalization is applied to the single images to obtain a uniform mosaic image [121]. The radiometric correction implemented after back projection involves a fusion strategy, by comparing the LiDAR return intensity and the hyperspectral information at the same wavelength [182]. This procedure requires spectral information beyond the VNIR spectral range.

2.3 Medium-level

Feature descriptors provide complementary information that is combined to form a composite set of features [117]. In this section, our literature review considers four important processes illustrated in Figure 2.3: feature extraction, feature stacking, feature selection and feature fusion.

2.3.1 Feature extraction

The main goal of these features is to represent the most relevant information from the original data [183]. From the fusion approaches, we have identified the following groups of feature descriptors: statistical, structural, topographic, vegetation indices, textural and dimension reduction.

- **Statistical features** have been widely used for forest tree characterization. In Table 2.2, a summary of statistical features are associated with their references and the data source: height from 3D point cloud, return intensity, CHM and spectral band. For instance, Dechesne et al. [165] compute these features by using three cylindrical neighborhoods around

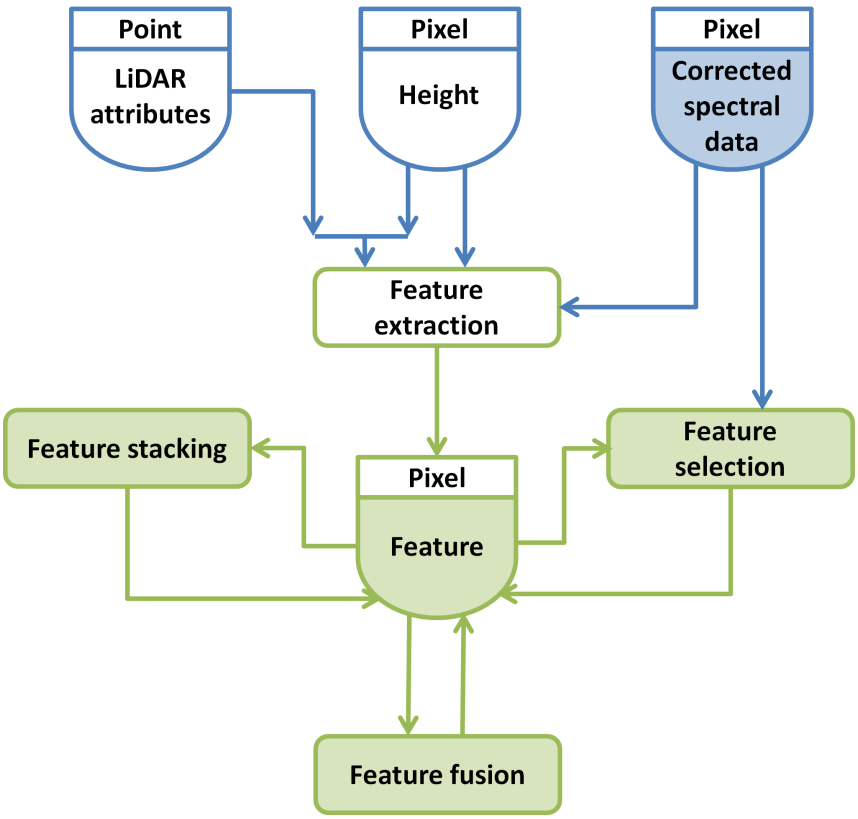

Figure 2.3: Fusion at medium level or feature level

each LiDAR point. Then, these features are projected on the CHM. In parallel, a set of statistical descriptors is computed at each spectral band by considering the same cylindrical radius. In Refs. [69, 73], authors compute these statistical features for every crown, which are extracted manually from field measurements [79] or by applying a segmentation algorithm. A review of segmentation approaches is described in the subsection of fusion at decision level.

- **Topographic features** or terrain features describe landscape level variations, which are related to the topography or soil [126]. A list of these type of features is described in Table 2.3. Cao et al. [75] compute these features from heights at the 3D point cloud. In [54, 126], these features are rasterized into a 2D representation.

- **Structural features** are summarized in Table 2.4, which are derived from LiDAR data. In Refs. [73, 123, 137, 155], authors compute these features by using the point cloud associated to each individual crown, which has been previously segmented in the CHM. Torabzadeh et al. [125] carry out these computations by handling return intensity.

- **Vegetation indices (VI)** derived from hyperspectral data are organized in 5 groups in the next tables: broadband greenness in Table 2.5, narrowband greenness in Table 2.6, light use efficiency in Table 2.7, leaf pigments in Table 2.8, dry or senescent carbon and canopy water content in Table 2.9. VI provide important radiometric characteristics for quantifying biophysical and biochemical indicators [69]. Studies show different strategies for the computation of these features. For instance, La et al. [152] obtain the NDVI index directly from the software *ENVI*. Kandare et al. [73] works at object level for averaging the pixel values inside every segmented crown at each band for deriving 16 VI. Luo et al. [74] focusing

Table 2.2: List of statistical feature descriptors with the respective references divided by the data source: height from 3D point cloud, amplitude of the return signal, CHM or spectral band

No.	**Statistical feature**	**Point cloud**	**Return intensity**	**CHM**	**Spectral band**
1	Minimum	[69, 165]		[139]	[165]
2	Maximum	[69, 73–75, 155, 165]		[139]	[165]
3	Mean	[74, 75, 155]	[165]		[165]
4	Median	[165]			[165]
5	Standard deviation	[69, 73–75, 165]		[139]	[165]
6	Variance	[73]			
7	Median absolute deviation from median	[165]			[165]
8	Mean absolute deviation from median	[165]			[165]
9	Mean absolute deviation from mean	[165]			[165]
10	Skewness	[73, 155, 165]		[139]	[165]
11	Kurtosis	[73, 155, 165]		[139]	[165]
12	Percentiles	[69, 73, 74, 125, 155, 165]	[125]		
13	Interquartile distance	[69]		[139]	
14	Coefficient of variation	[69, 73–75, 155]			

Table 2.3: List of topographic feature descriptors with the respective references divided by the data source: height from 3D point cloud or CHM

No.	**Topographic feature**	**Point cloud**	**CHM**	No.	**Topographic feature**	**Point cloud**	**CHM**
1	Aspect	[162]	[126]	2	Foliage height diversity	[54]	
3	Hillshade	[75]	[126]	4	Profile curvature	[75, 162]	
5	Slope	[75, 162]	[126]	6	Elevation data		[126]
7	Tree height	[54]	[126]	8	Topographic wetness index	[75]	
9	Plant area index	[54]		10	Compound topographic index	[162]	
11	Disection	[162]		12	Heat load index	[162]	
13	Planar curvature	[162]		14	Heat load index	[162]	
15	Site exposure index	[162]		16	Surface relief ratio	[162]	
17	Total curvature	[162]		18	Vector ruggedness model	[162]	

on the group of narrowband greenness because these VI reduces the saturation effect and improve the biomass estimation.

- **Textural features** are widely used in computer vision because these contain information concerning the structural arrangement of surfaces and their relationship to the surrounding environment [224]. Gray-Level Co-occurrence Matrix (GLCM) was computed by Dalponte et al. [79] over the band of 810*nm*. Alternatively, Cao et al. [75] implemented the texture analysis after computing Principal Component Analysis (PCA) over the first component. Plowright et al. [139], extract textural information by using the extended morphological profile method through circular structuring elements over the first three principal components of the hyperspectral data.

- **Dimension Reduction** is a special form of feature extraction [183]. Most of the feature extraction techniques revised previously, are focused on processing one modality at a time. In Refs. [69, 130, 132, 135], authors apply PCA for obtaining the most meaningful information from hyperspectral metrics. In Refs. [75, 151, 152], PCA is obtained by using the software *ENVI*.

  In Refs. [127, 156], robust PCA (rPCA) is used for feature extraction of hyperspectral imagery. For tree crown segmentation purposes, the first principal component was ignored because it contained illumination information rather than useful features [225]. The second to fifth principal components were extracted and assigned to corresponding LiDAR points by using horizontal geospatial coordinates.

  Zhang et al. [129], segregate spectral noise in hyperspectral data by applying Minimum Noise Fraction (MNF) transformation. This is a linear transformation of the original bands that applies two cascaded PCA and maximizes the ratio of signal to noise. This procedure can be performed in the software *ENVI*. Dian et al. [128] select the first 10 MNF bands

Table 2.4: List of structural feature descriptors with the respective references divided by the data source: height from 3D point cloud or return intensity

No.	**Structural feature**	**Point cloud**	**Return ntensity**
1	Crown height	[123, 125, 137]	
2	Crown widths at selected heights	[123, 137]	
3	Ratios of crown heights to widths at selected heights	[123, 125, 137]	
4	Direct measures of return intensity through the crown	[123, 137]	
5	Distributions of intensity through the crown		[123, 137]
6	Crown porosity measured by return penetration into the crown		[123, 137]
7	Occupied length of the vertical column by vegetation	[125]	
8	Number of detected canopy layers	[125]	
9	Relative position of the largest canopy layer	[125]	
10	Cumulative intensity		[125]
11	Point density	[125]	
12	Scatter	[165]	
13	Planarity	[165]	
14	Number of local height maxima	[165]	
15	Number of non-ground points within neighborhoods	[165]	
16	Cumulative proportional canopy density	[69, 73, 155]	
17	Canopy volume	[155]	
18	Crown area	[73, 73]	
19	Laser intercept index	[74]	
20	Percentage of returns $> 0.5m$	[139]	
21	Canopy cover (Percentage of first returns $> 2.0m$)	[69, 75]	

Table 2.5: Broadband greenness

No.	VI	Ref.	No.	VI	Ref
1	Normalized Difference Vegetation Index (NDVI)	[69, 72–76]	2	Non-Linear Index (NLI)	[184]
3	Renormalized Difference Vegetation Index (RDVI)	[158, 185]	4	Modified Non-Linear Index (MNLI)	[186]
5	Green Normalized Difference Vegetation Index (GNDVI)	[69, 73, 76, 80, 187]	6	Green Leaf Index (GLI)	[188]
7	Infrared Percentage Vegetation Index (IPVI)	[73, 76, 189]	8	Transformed Difference Vegetation Index (TDVI)	[190]
9	Triangular Greenness Index (TGI)	[191]	10	Difference Vegetation Index (DVI)	[73, 76, 192]
11	Green Difference Vegetation Index (GDVI)	[193]	12	Green Red Difference Index (GRDI)	[192]
13	Difference Difference Vegetation Index (DDVI)	[76, 194]	14	Enhanced Vegetation Index 1 (EVI1)	[69,73,74,76,128, 195]
15	Enhanced Vegetation Index 2 (EVI2)	[76, 196]	16	Leaf Area Index (LAI)	[197]
17	Simple Ratio Vegetation Index 1 (SRVI1)	[69, 73–76, 126, 198]	18	Modified Simple Ratio (MSR)	[199]
19	Green Chlorophyll Index (GCI)	[54, 67–69]	20	Green Ratio Vegetation Index (GRVI)	[200]
21	Green Red Ratio Vegetation Index (GRRVI)	[76, 201]	22	Blue Ratio Vegetation Index (BRVI)	[76, 201]
23	Red Ratio Vegetation Index (RRVI)	[76, 201]	24	Sum Green Index (SGI)	[69, 202]
25	Soil Adjusted Vegetation Index (SAVI)	[69, 74, 75, 203]	26	Optimized Soil Adjusted Vegetation Index (OSAVI)	[74, 204]
27	Modified Soil Adjusted Vegetation Index 2 (MSAVI2)	[74, 75, 158, 205]	28	Green Soil Adjusted Vegetation Index (GSAVI)	[193]
29	Green Optimized Soil Adjusted Vegetation Index (GOSAVI)	[193]	30	Green Atmospherically Resistant Index (GARI)	[76, 206]
31	Visible Atmospherically Resistant Index (VARI)	[76, 207]	32	Wide Dynamic Range Vegetation Index (WDRVI)	[208, 209]

Table 2.6: Narrowband greenness

No.	VI	Ref.	No.	VI	Ref
33	Modified Normalized Difference Vegetation Index (MNDVI)	[74, 210]	34	Red Edge Normalized Difference Vegetation Index (RENDVI)	[76, 80, 126, 211, 212]
35	Modified Red Edge Normalized Difference Vegetation Index (MRENDVI)	[69, 76, 212]	36	Simple Ratio Vegetation Index 2 (SRVI2)	[74, 210]
37	Modified Red Edge Simple Ratio (MRESR)	[73, 76, 212, 213]	38	Red Edge Chlorophyll Index (RECI)	[68, 69]
39	Vogelmann Red Edge Index 1 (VREI1)	[73, 214]	40	Vogelmann Red Edge Index 2 (VREI2)	[214]
41	Red Edge Inflection Point (REIP)	[74, 126, 215]	42	Atmospherically Resistant Vegetation Index (ARVI)	[73, 74, 76, 216]
43	Modified Chlorophyll Absorption Ratio Index 1 (MCARI1)	[70]	44	Modified Chlorophyll Absorption Ratio Index 2 (MCARI2)	[71]
45	Transformed Chlorophyll Absorption Reflectance Index (TCARI)	[69, 71]	46	Triangular Vegetation Index (TVI)	[217]
47	Modified Triangular Vegetation Index 1 (MTVI1)	[71]	48	Modified Triangular Vegetation Index 2 (MTVI2)	[71, 158]

Table 2.7: Light use efficiency

No.	VI	Ref.	No.	VI	Ref
49	Photochemical Reflectance Index (PRI)	[69, 76, 126, 218, 219]	50	Structure Insensitive Pigment Index (SIPI)	[69, 73, 220]
51	Red Green Ratio Index (RGRI)	[69, 221]	52	Photochemical Reflectance Ratio (PRR)	[69, 222]

Table 2.8: Leaf pigments

No.	VI	Ref.	No.	VI	Ref
53	Anthocyanin Reflectance Index 1 (ARI1)	[69, 73, 81]	54	Anthocyanin Reflectance Index 2 (ARI2)	[69, 73, 81]
55	Carotenoid Reflectance Index 1 (CRI1)	[69, 73, 82]	56	Carotenoid Reflectance Index 2 (CRI2)	[69, 73, 82]
57	Carotenoid Reflectance Index 3 (CRI3)	[68]	58	Carotenoid Reflectance Index 4 (CRI4)	[54, 68]
59	Plant Pigment Ratio (PPR)	[69, 83]			

Table 2.9: Dry or senescent carbon and Canopy water content

No.	VI	Ref.	No.	VI	Ref
60	Plant Senescence Reflectance Index (PSRI)	[73, 76, 223]	61	Water Band Index (WBI)	[73, 84]

based on eigenvalues.

2.3.2 Feature stacking

One of the most straightforward strategies for fusing features is via vector stacking [226]. Stacking together features from two different sensor modalities form a new fused feature space [227]. Usually, studies evaluate the effect of stacking LiDAR features to the hyperspectral data to improve the tree species discrimination. The main challenge in this fusion strategy is to balance the amount of information represented by each feature set. For instance, Dalponte et al. [121] select 40 hyperspectral features and add two LiDAR images (elevation and intensity) for feature classification. Van Coillie et al. [132] apply PCA independently over the hyperspectral bands and the LiDAR-derived percentile This height values. By stacking these features, the approach showed good results for small training set size in tree species classification. Liao et al. [130] fuse multi-scale features generated from the LiDAR data and the principal components of hyperspectral data, by considering five different windows size, which are associated to the tree crown size. The multi-scale features are generated by applying a sliding window centered at one pixel over the hyperspectral images and the CHM.

2.3.3 Feature selection

Unlike feature extraction, in which new features are created, the feature selection methods output a subset of meaningful features. In Refs. [123, 137], authors use Forward Feature Selection (FFS) over the structural metrics from LiDAR information. In Refs. [121, 122, 159], hyperspectral features were selected from the originals bands by applying Sequential Forward Floating Selection (SFFS) algorithm and the Jeffries-Matusita distance metric. Torabzadeh et al. [125] apply SFFS together with transformed divergence as a separability evaluation criterion. Spectral bands and structural features were separately selected.

Shen et al. [69] apply correlation analysis in order to exclude those metrics that are strongly correlated with others for classification purposes. Sommer et al. [126] develops a hyperspectral

band selection based on three conditions: band variance, band correlation and the correlation of the bands with the components of a PCA. Although, these strategies consolidate criteria for feature discrimination and avoid issues dealing with high-dimensional data, it is necessary to evaluate the effect of the amount of features to be selected over the task to improve.

2.3.4 Feature fusion

Linear [166, 228, 229] and non-linear [167] approaches have been proposed for feature fusion strategies. The linear approach is based on fusion graph algorithm [166, 229] that couples spatial, spectral and elevation information by extracting morphological profiles (MP) over the first two principal components of the hyperspectral data and the DSM derived from LiDAR data. Before the integration of each feature set, these are reduced to the size of the small feature set by using Kernel Principal Component Analysis (KPCA) [230]. The reduced feature sets are stacked and weighted by the distance through the edges of the fusion graph. An improvement of this method is achieved by employing the local spatial neighborhood information in a local graph fusion [166, 228]. This method reduces the computational complexity and provides a stable performance.

A deep fusion framework [167] is introduced to integrate the complementary information from hyperspectral and LiDAR data by applying a stacked autoencoder (multiple hidden layers of neurons). The deep learning approach by itself does not provide good results for the species classification. For this reason, the neighborhood information is considered by using a 5×5 sliding window centered pixel, and the PCA algorithm for feature extraction. The classification accuracy improved from 82.21% to 87.10%.

2.4 High-level

At this level of fusion, each modality is processed independently [119], to develop rule-based models that require eventually the processing from signal to information [118]. For a decision level of fusion, the integration of available information refines the results and maintains the best from the intermediate results [117, 119]. In this section, we focus on four strategies of fusion (see in Figure 2.4): classification, segmentation, association and prediction-estimation.

2.4.1 Classification

Tree species identification has attracted increasing attention across the remote sensing community. In 2016, Fassnacht et al. [231] collected 129 studies on species identification, from which 78 are related with multi/hyperspectral images. The classification methods used in this context are mainly based on non-parametric classifiers, which are adaptive to any kind of data distribution.

A first approach to use LiDAR information with hyperspectral data at the pixel level consists in creating masks over non-forest areas [232]. The masks avoid the spectral signature of other materials and plants to interfere with forest spectra in the classification process. In Refs. [80, 126, 129, 154], NDVI is used to separate vegetation from non-vegetation.

Sunlit criterion is another method for masking used by Refs. [69, 73, 78–80, 125, 159] to select those pixels, whose reflectance value in a determined portion of the spectrum are higher than a threshold.

A second approach consists in performing the classification from the fused features obtained in the feature level of fusion. Ballanti et al. [233] compare the performance of Support Vector Machine (SVM) [75, 79, 121, 122, 125, 132, 135, 155, 159, 161] and Random Forest (RF) [69, 75, 122, 126, 139] classifiers with two different parameters of canopy segmentation. The comparison

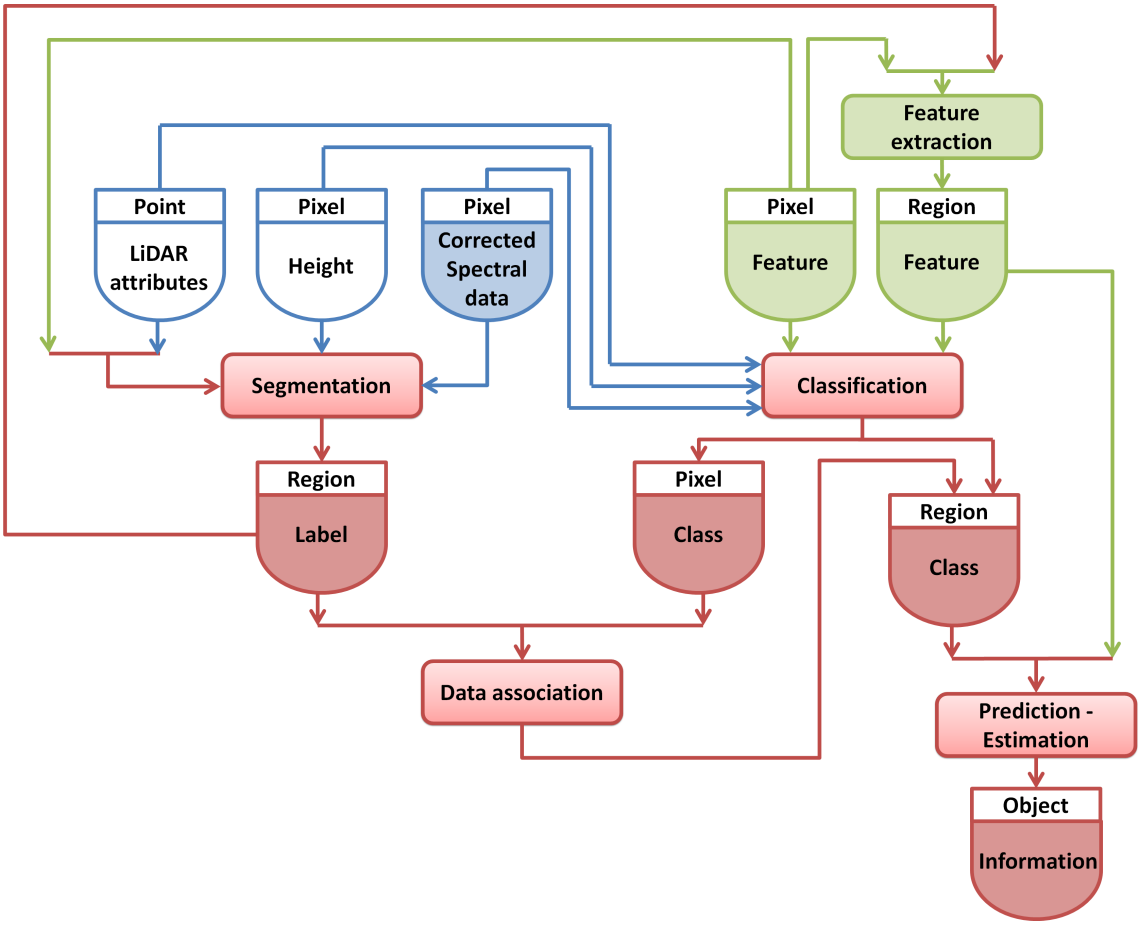

Figure 2.4: Fusion at high level or decision level

confirms that both classifiers performs well (overall accuracy above 90%). The overall SVM accuracy reaches even 95% for pixel-based samples.

Trier et al. [80] apply deep learning for pixel classification based on 160 hyperspectral channels in the visible and near-infrared spectrum with promising results. On the other hand, Refs. in [123, 137], they apply Canonical Discriminant Analysis, which uses derived canonical discriminant functions as linear combinations of the original variables for maximizing the coefficients between-group separation.

Sankey et al. [131, 133] proposes the mixture-tuned matched filtering sub-pixel classification technique, by matching the spectral signature in the image pixel to the known spectral signature of each species. Similar to this technique, Dutta et al. [158] use the Spectral Angle Mapper (SAM) to classify the spectra of each pixel with respect to a tree species library.

2.4.2 Segmentation

Segmentation strategies are oriented to the partition of an image into non-overlapping regions based on specific criteria. Several approaches of segmentation are implemented mostly at the CHM for Individual Tree Crown (ITC) delineation before fusing with already classified hyperspectral data. Marker-Based Watershed (MBW) [79, 157, 234] is implemented in the software *Tiff* [127, 156] for ITC delineation in the CHM. The algorithm initialization takes the treetop detections based on local maxima filtering [95]. In Refs. [123, 137], authors combined two watershed segmentation routines for locating crowns and subdividing the initial segments.

Region growing algorithm [135, 157, 159, 235] is an ITC segmentation approach implemented

in the software *eCognition* [129]. This approach is also initialized with treetop detections and can be applied to the CHM and the hyperspectral image. The package *itcSegment* [236] in the software *R* implements this algorithm for ITC delineation in Refs. [155, 161].

Region growing can be extended at the 3D point cloud in the Point Cloud Segmentation Algorithm (PCS) available in the software *LiForest* [69]. In Refs. [127, 156], they applied MBW for generating local maxima detections in the CHM, which represent the priors for graph cut segmentation in the 3D point cloud. The subdivision process in each cluster detects subcanopy trees, which is not feasible for the 2D segmentation algorithms. While Dian et al. [128] applies a mean shift algorithm for computing an object-based map of the canopy, Ferraz et al. [96, 97] has extended this technique to the 3D point cloud.

2.4.3 Data association

This approach consists of identifying tree species from delineated trees and voting rules. In Refs. [79, 127, 155, 158, 159, 161], the classification at ITC level was obtained by aggregating the classified pixels inside each ITC according to a majority rule. The most frequent species category inside of each ITC represents the tree specie. Dian et al. [128] propose a threshold of 50% of the total amount of pixels to define the specie of the tree. Matsuki et al. [135] propose a crown-preserving smoothing filter by a weighted vote of the class from neighboring pixels with the aim of reducing the salt-and-pepper noise due to misclassification while preserving the crown edges.

2.4.4 Prediction-estimation

The objective is to develop prediction models for estimating variables or for assessing specific characteristics of forest trees. Conventionally, linear regression methods [128, 131, 133, 154] aim to validate structural attributes such as tree height, crown diameter, base height or crown depth between LiDAR metrics and field measurements with a high coefficient of determination (R^2). Lee et al. [144] propose a Quadratic Linear Model (QLM) to estimate Photochemical reflectance index (PRI) as function of the altitudinal gradient with a low R^2 between 0.16 and 0.21. Luo et al. [74] fuse LiDAR metrics and VI to estimate the aboveground and belowground biomass by applying Partial Least Square Regression (PLSR) [146–148]. This multivariate statistical method deals with multicollinearity problems due to the high correlations among metrics. From PLSR analysis, Luo et al. [74] concluded LiDAR metrics are strongly related to forest biomass, while hyperspectral data does not provide significant improvement. RF [136, 143] is used for richness prediction with significant results (Adjusted $R^2 = 0.571$). However, the added value of hyperspectral plus LiDAR data was found to be low. Alternatively for species richness prediction, self-adaptive Fuzzy C-Means (FCM) clustering [142] was applied by combining VI and tree height data with a high $R^2 = 0.83$. It is still challenging to determine how to retrieve leaf properties from canopy reflectance data acquired from airborne imaging spectrometers at tree level.

2.5 Applications

This section reviews a set of 50 contributions oriented to forest monitoring applications that combines hyperspectral images and LiDAR data at different levels of fusion. In Table 2.10, we have grouped these studies into five categories by having as reference the work developed by Torabzadeh et al. [124]. We remark 98% of these works achieve a decision level fusion that involves tasks of segmentation, classification, data association or prediction-estimation; having taken into account that 62% of these studies transit through the three levels of fusion. Although

34% propose approaches both on observation and decision level, most of these contributions apply the extraction or selection of features from one modality. Finally, 4% remains at one level of fusion, either observation or decision.

Table 2.10: Studies of forest monitoring classified by the type of application and the level of fusion

Aplication (Number of studies)	Fusion Level		
	Observation	Feature	Decision
Species mapping (17)	[69, 121–133]		
	[134, 135]		[134, 135]
Functional and physiological attributes (16)	[73, 136–142]		
	[54, 143–149]		[54, 143–149]
Structural attributes (9)	[150–156]		
	[158]		[157, 158]
Above ground biomass & carbon density (5)	[159–161]		
	[74, 162]		[74, 162]
Landcover maps (4)	[77–80]		[78–80]

The application of species mapping refers to the mapping of individual tree species which represent 32% of our studies. 50% of these approaches used SVM to classify between 8 and 23 species by achieving an overall accuracy of 90.8%. Functional and physiological attributes correspond to the prediction of chemicals in plant leaves such as foliar traits, canopy water content, site index, imperviousness, among others varibles that represent 32% of the reviewed works. 18% of the contributions are about structural attributes such as ITC delineation, prediction of height or Diameter at Breast Height (DBH). This task requires a good segmentation approach, which is executed by region growing algorithm at the CHM. Above ground biomass and carbon density (10% of the researched applications) is more accurately estimated by LiDAR data, so enhancing the estimation with the fusion of hyperspectral images is still a challenge. Finally, 8% of our studies correspond to landcover maps, which deals with the mapping of large classes of species: forest and non-forest, or conifers and broadleaves. This application present high overall accuracies between 67-97.4%, with an ensemble of SVM and Gradient Boosted Machine (GBM) [78].

3 Material

In this chapter, we describe the datasets used for the algorithm assessment in this thesis. First, we describe the process for obtaining the data from the field by measuring individual trees. We explain the procedure to employ the mapping tools and the metrics to be extracted from the forest trees. In this part, we mention the shortcomings of mapping individual trees and the strategies applied for having co-registered data. Second, we provide details of the specie composition, the location and the forest plot characteristics of the study sites employed in this thesis. Finally, we give the specifications of the LiDAR and hyperspectral data collected during the airborne data acquisitions.

Sommaire

3.1 Field data

Remote sensing data have changed the perspectives of characterization of individual trees. In a field survey, the measurements of the diameter at breast height (DBH) involve an easy and straightforward procedure, from which other tree geometric characteristics can be derived. For instance, allometric equations can establish relationships between the tree height and the DBH through regression models [237–239].

The geometric information from LiDAR data acquisition makes possible to estimate directly the tree height with high accuracy [240]. In addition to this, the radiometric variables from hyperspectral data form a basis for extracting feature descriptors in order to predict forest tree species. Then, a proper alignment between these two remote sensing modalities and the ground data guarantees a proper model calibration for estimation and prediction of variables of interest [241].

In this work, field data is relevant for parameter estimation, training and evaluation of algorithms for individual tree crown (ITC) delineation and forest tree species classification. Accurate location of trees positions is needed in this regard, as well as reference measures of their characteristics: diameter at breast height (DBH), tree height and crown extension. In order to test the algorithms in forest stands with various stands and structures, two study sites are used: Chamrousse site in France and Pellizzano site in Italy. In the Chamrousse site, plots are located along an altitude gradient based on the Orchamp long-term monitoring site [242]. Since this chapter explains the tree measurements procedures for the Chamrousse site. For the Pellizzano, the details are given in the Ref. [159, 170].

3.1.1 Mapping tools

Global Navigation Satellite System (GNSS) provide signals from space that transmit positioning and timing data to GNSS receivers. Under open sky conditions, standard accuracy GNSS receivers are accurate in a range of two meters. However, GNSS accuracy below canopy makes it not possible to map each tree individualy with a GNSS receiver, otherwise their relative positions could be wrong. The strategy proposed in this project is to map the tree positions in spherical coordinates relatively to a central point (sometimes additional points are needed) with the mapping equipment that is described in this subsection. The geolocation of the central point is measured with a GNSS receiver operating for at least 5 minutes with 1 s sampling. This protocol was chosen according to a study made by the research and development unit of ONF, considering a trade-off between accuracy and measurement time. Tree coordinates are converted to projected coordinates by taking into account the magnetic declination at the date of mapping and the meridian convergence of the projection system at the location.

The mapping equipment is adapted for working in remote forest areas that usually have limited road access. This is why these instruments are particularly lightweight for being carried several hundred meters up and down hills. Figure 3.1 presents the devices used for tree measurements: clinometer and compass (Figures 3.1(a) and 3.1(b)), hypsometer (Figures 3.1(c)) and transponder (Figures 3.1(d)). Figure 3.2 showed the stages for tree mapping by locating the GPS point for referencing every single tree inside the forest plot.

The clinometer and compass from Figure 3.1(a) is mounted in the tripod from Figure 3.2(a) which is located in the GPS point as it is set by the operator in the Figure 3.2(b). For distance measures, an hypsometer VERTEX III and a transponder (shown in Figures 3.1(c) and 3.1(d), respectively) are more convenient than laser rangefinders when understory and bushes are present. These are useful for tree location by setting the transponder in the trunk of the tree as it is illustrated in Figure 3.2(c), and registering the tree positions.

(a) Clinometer and compass for tripod

(b) Clinometer and compass for manual use.

(c) Hypsometer.

(d) Transpoder.

Figure 3.1: Mapping tools used for forest tree inventories.

3.1.2 Geolocation

A precise co-registration among LiDAR (reference) and the field data is imperative for the successful characterization of individual forest trees [241]. The use of GPS devices for geolocation of the forest plots are sensitive to physical obstructions with respect to satellites. The availability and geometry of satellites can be better described by the dimensionless parameter position dilution of precision (PDOP) [243]. In fact, this metric increases when conditions are not favourable. For example, the forest canopy distorts the wave propagation by attenuating or blocking completely the GPS signal, resulting in a strong multipath effect and high PDOP [244].

Openings and clearings have almost arisen in higher location accuracy than forested sites. For this reason, GPS position is recorded in a nearby cleared area in order to locate the plot relatively to the GPS point. Additional reference points may be added when all trees are not visible from the previously materialized points. The validation of the algorithms for the segmentation of individual trees requires a GPS signal acquired on the field plots by considering the digital terrain model (DTM) [241]. For better registration between the tree positions relatively to the LiDAR dataset, the co-registration procedure in Ref. [245] has been applied.

3.1.3 ITC metrics

This section describes the definition of the main tree parameters considered in this document, and how these metrics are derived from field measurement, as it is illustrated in Figure 3.3.

- **Diameter at breast height**: DBH is the diameter measured in cm at 1.3 m vertical height

(a) Tripod with clinometer and compass

(b) Operator in the tripod

(c) Transpoder on the tree

Figure 3.2: Illustration of mapping individual trees in the site of Chamrousse, France by using the tripod, clinometer, compass, hypsometer and transponder.

above the ground [29, 241, 246]. By assuming the stem cross-sectional shape approaches a circle, DBH is estimated by measuring the circumference c of the stem cross-sectional by using a ruban tape. Then, the diameter of the circle that has the same circumference c is computed as follows: $\hat{d} = \frac{c}{\pi}$. DBH is important because it correlates closely to the wood volume in the stem of a tree or the weight (or biomass) of a tree [247].

- **Tree height**: total tree height is defined as the vertical distance from the ground level at tree stem to the highest twig of the tree [29, 241, 246]. Tree height is not the trunk length as it is shown in Figure 3.3(a), where all tree are same height [248]. For tree height measurement, geometric or trigonometric methods [247] are embodied in the use of hypsometers (see Figure 3.1(c)) to measure angles and distances to points on the tree. The height of the tree is important in calculating the trunk volume, in reflecting the competitive position of a tree in a stand, and in assessing the productivity capacity of the site [247].

- **Crown radius**: the tree crown size provides important factors in relation to the growth, health and technical quality of the tree stock [29, 249]. The crown radius is the distance between the center of the bole and the outer edge of the crown [44]. This metric can be derived from the crown extension by measuring the radius in the four cardinal directions: north (N), south (S), east (E) and west (W); as it is represented in Figure 3.3(b)). This method projects the outline of the crown vertically onto the ground, or more precisely, onto a horizontal plane [248]. For this horizontal projection, vertical sighting method [250] is applied to be aligned to the widest spread in the selected direction by using the clinometer and compass from Figure 3.1(b). Then, the radius can be measured by using the hypsometer (Figures 3.1(c)) and transponder (Figures 3.1(d)), as it is performed in Figure 3.3(c), where the transponder is put on the trunk, and the other operator measures the radius in the assigned direction with the hypsometer. Alternatively, ruban tape can be used to measure the radius distance as it is illustrated in Figure 3.3(d).

  If we consider r_N, r_S, r_E and r_W, as the crown radii in the respective four cardinal directions, the crown area A can be estimated as the summation of four quarters of the area associated

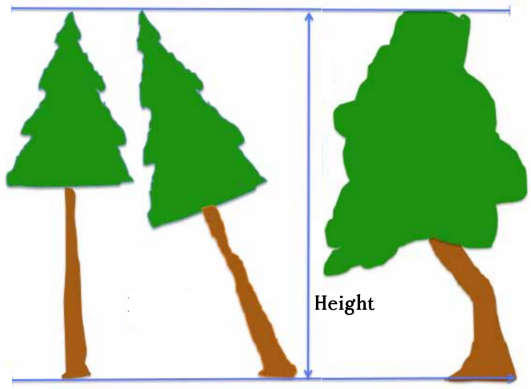

(a) All trees are the same height, which implies tree height is not trunk length.

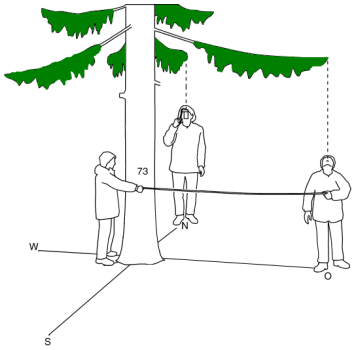

(b) Crown extension measurements in four directions

(c) Tree Crown extension measured with clinometer, compass, hypsometer and transponder.

(d) Tree Crown extension measured with clinometer, and compass, and ruban tape.

Figure 3.3: Tree height and crown spread measurements generated from the field survey in the site of Chamrousse, France.

to four different ellipses: $\hat{A} = \frac{\pi}{4}(r_N r_E + r_E r_S + r_S r_W + r_W r_N)$. Although an estimate of the crown radius r can be derived by applying the quadratic mean of the aforementioned crown radii [250], the crown area is approached as circle surface in order to estimate the crown radius by following this expression: $\hat{r} = \sqrt{\frac{\hat{A}}{\pi}}$.

- **Crown length**: this measurement is defined as the distance between the apex of the tree and the base of the live crown [44]. In some studies, the base of the live crown coincide to the point half way between the lowest green branches forming green crown all round and the lowest green branch on the bole [251]. From the field survey, the base is referenced by the position of the lowest green branch, which has been measured from the tree ground level.

- **Basal area**: this metric is estimated from the DBH d or directly from the circumference c, and corresponds to the area of the horizontal section of the tree stem at 1.3 m height [44, 241]:

$$g = \frac{\pi d^2}{4 \cdot 10^4} \tag{3.1}$$

If a forest stand of surface S is considered for monitoring, the stand-level metrics can be computed from the ITC metrics. A DBH threshold is usually applied to avoid trees that have limited effect on the topic of interest. Typically, trees with DBH of 17.5 *cm* are relevant for management in a harvesting perspective, while DBH of 7.5 *cm* are for research on the stand dynamics. Lower

diameters are interesting for studying regeneration, but inventory is then done on smaller surfaces. In our case, except for small trees located inside forest gaps, trees that should be visible in the airborne data have diameters above 7.5 *cm*.

- **Dominant height**: This metric is defined as the mean height of the 100 trees with the largest diameters per hectare.
- **Stem density**: If we consider S as the surface of the forest area, this attribute is the average number of trees per hectare:

$$N = \frac{N_T}{S} \tag{3.2}$$

- **Basal area, mean diameter**: Based on the their counterparts of included trees (g_i, d_i), the basal area and mean diameter are computed as follows:

$$G = \frac{1}{S}\sum_{i=1}^{N_T} g_i \quad D = \frac{1}{N_T}\sum_{i=1}^{N_T} d_i \tag{3.3}$$

3.2 Study areas

3.2.1 Chamrousse site

Chamrousse site is located in Belledonne massif, Northern Alps, France [164, 252, 253]; as it is shown in Figure 3.4. Seven plots were used: four of size of 50×50 m^2, two circular plots of 15 m radius, and a plot of 80×100 m^2, which is part of a long-term inventory dataset [22]. Four forest plots are located along an altitude gradient based on the Orchamp long-term monitoring site [242]. The forest is dominated by Norway spruce (*Picea abies*; 37.5%) and other conifers: silver fir (*Abies alba*; 31.6%) and mountain pine (*Pinus uncinata*; 10.6%); broadleaves species are mainly represented by European beech (*Fagus sylvatica*; 15.2%). Table 3.2 describes the percentage distribution of forests tree species among all the seven plots. Tree crown extensions are measured with ruban tapes in the north, south, east and west directions as the horizontal distance between the trunk center and the vertical projection of the furthest live branch along that direction. The field data is summarized in Table 3.1 by considering seven plots with 894 tree crowns.

Table 3.1: Summary of the field measurements at tree- and plot- level in the Chamrousse site: Minimum (Min), Maximum (Max) and Mean are displayed.

Level	Field measurement	Min.	Max.	Mean
Tree	DBH [cm]	7.5	104.5	26.2
	Tree Height [m]	2.0	38.4	14.8
	Crown area [m^2]	0	161.9	23.3
Plot	Mean DBH [cm]	16.3	31.2	25.8
	Number of $stems/ha$	460	980	640
	Basal Area [m^2/ha]	13.0	64.5	40.8

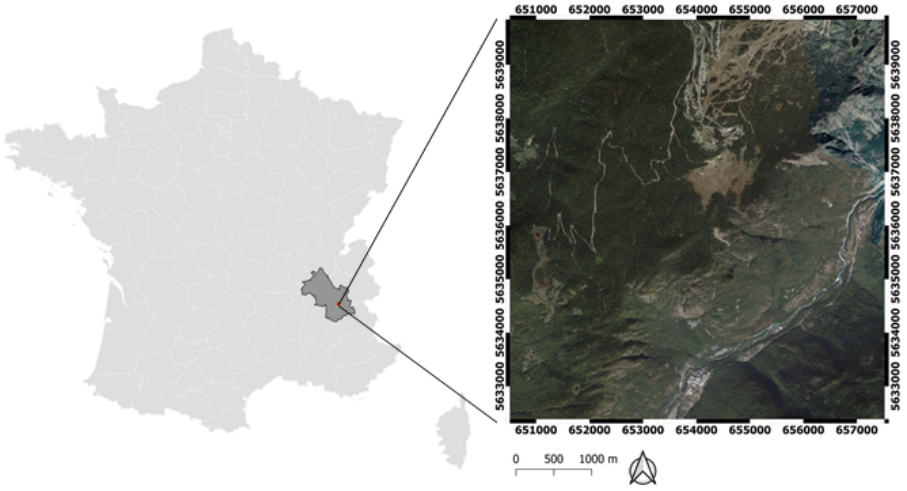

Figure 3.4: Chamrousse site is located in the department of Isère, in the Auvergne-Rhône-Alpes region in eastern France. The area of study is referenced in the Lambert 93 *projected coordinate system.*

Table 3.2: Abbreviation, full name and number of tree crowns per species encountered in the Chamrousse site. The total number of tree crowns is 894*.*

Abbr.	Genus species	English name	No.	%
ABAL	*Abies alba*	European silver fir	282	31.6
ACPS	*Acer pseudoplatanus*	Sycamore maple	10	1.1
BEPE	*Betula pendula*	Silver birch	13	1.5
BEsp	*Betula sp.*	Birch	3	0.3
COAV	*Corylus avellana*	Common hazel	7	0.8
FASY	*Fagus sylvatica*	European beech	136	15.2
FREX	*Fraxinus excelsior*	European ash	1	0.1
PIAB	*Picea abies*	Norway spruce	335	37.5
PICE	*Picea cembra*	Swiss pine	1	0.1
PIUN	*Pinus uncinata*	Mountain pine	95	10.6
POTR	*Populus tremula*	European aspen	4	0.5
SOAR	*Sorbus aria*	Common whitebeam	3	0.3
SOAU	*Sorbus aucuparia*	Rowan	3	0.3

3.2.2 Pellizzano site

This site [159, 170] is located in the municipality of Pellizzano in the Italian Alps [159, 170] as it is presented in Figure 3.5. In this site, 15 circular plots were measured: six plots have radius of 15 *m* and the remaining ones have 20 *m* radius. Tree crown was derived from the field-measured distances in the four cardinal directions from the trunk center to the crown boundary assuming an ellipsoidal shape. The complex forest structure is formed by coniferous trees: 75.7% of Norway spruce, 9.8% of larch (*Larix decidua*) and small proportions (more than 10 trees) of broadleaves such as silver birch (*Betula pendula*) and common alder (*Alnus glutinosa*). Table 3.4 describes the percentage distribution of forests tree species among all the 15 plots. The field data is summarized in Table 3.3 by considering seven plots with 543 tree crowns.

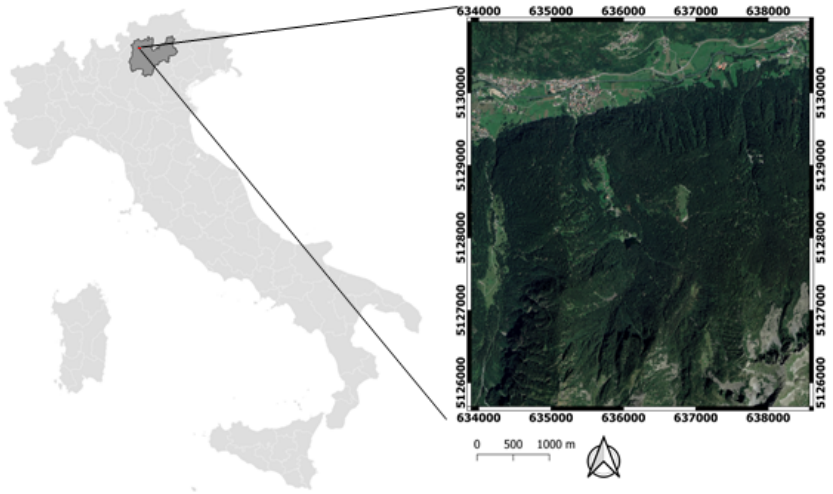

Figure 3.5: Pellizzano site is located in the Province of Trento, in the Trentino-Alto Adige region in northern Italy. The area of study is referenced in the WGS 84 / UTM zone 32N projected coordinate system.

Table 3.3: Summary of the field measurements at tree- and plot- level in the Pellizzano site: Minimum (Min), Maximum (Max) and Mean are displayed.

Level	Field measurement	Min.	Max.	Mean
Tree	DBH [cm]	5.0	89.0	32.3
	Tree Height [m]	2.5	39.8	21.5
	Crown area [m^2]	0	123.7	17.1
Plot	Mean DBH [cm]	21.7	58.1	36.7
	Number of $stems/ha$	127	1050	502
	Basal Area [m^2/ha]	35.7	77.8	55.0

Table 3.4: Abbreviation, full name and number of tree crowns per species encountered in the Pellizzano site. The total number of tree crowns is 543.

Abbr.	Genus species	English name	No.	%
ABAL	*Abies alba*	European silver fir	13	2.4
ACPS	*Acer pseudoplatanus*	Sycamore maple	13	2.4
ALGL	*Alnus glutinosa*	Common alder	17	3.1
BEPE	*Betula pendula*	Silver birch	18	3.3
BEVU	*Berberis vulgaris*	European barberry	1	0.2
COAV	*Corylus avellana*	Common hazel	3	0.6
FASY	*Fagus sylvatica*	European beech	2	0.4
LADE	*Larix decidua*	European larch	53	9.8
PIAB	*Picea abies*	Norway spruce	411	75.7
POTR	*Populus tremula*	European aspen	1	0.2
SAAL	*Salix alba*	Willows	1	0.2
SOAU	*Sorbus aucuparia*	Rowan	10	1.8

3.3 ALS and hyperspectral data

3.3.1 Chamousse site

Airborne laser scanning (ALS) data were acquired between 11th and 29th of June 2018, using a Riegl LMS Q780 laser scanner. The point cloud was classified in ground and vegetation classes by using TerraScan software. The average point density was of 40 $points\ m^{-2}$, and the ground point density was of 8.5 $points\ m^{-2}$. The scan frequency was up to 400 kHz with a 60° field of view and the overlap for each stripe was at least 50%.

Hyperspectral data were acquired on 23rd of June 2018 with an Hyspex VNIR 1600 SN0014 sensor. The minimum overlap among the images was 45%. Each image is characterized by 160 spectral bands acquired between 400 and 1000 nm, by a spatial resolution of 0.80 m and by spectral resolution of 4.5 nm. The images were orthorectified by using the digital surface model (DSM) generated from the LiDAR point cloud with a resolution of 0.50-m [254]. The relative geometric precision obtained between two lines on the area of interest is of the order of 2-3 pixels. The atmospheric corrections were carried out by ATCOR-4 model [255]. The aerosol model used is "Rural". Visibility is fixed and configured as constant for each zone; visibility of 60 km was retained. DSM is then taken into account to adjust the optical thickness levels of the aerosols on the areas of interest. In order to attenuate the effects of bidirectional reflectance distribution function (BRDF), ATCOR-4's BREFCOR module [256] has been implemented to produce albedo-type data. However, given the small angular opening of the sensor (17°), the effects of BRDF are limited and therefore the effect of the BREFCOR corrections as well.

3.3.2 Pellizzano site

ALS data were acquired between 7th and 9th of September 2012, using a Riegl LMS-Q680i laser scanner. The system mounted on a Multi Mission Aircraft was optimized to measure canopy structure with a flying speed of about 51 m/s at an altitude of 660 m above ground level. The scan frequency was 400 kHz with a 60° field of view and the overlap for each stripe was at least 30%. Up to five returns were recorded for each emitted pulse and the average point density was

of 48 *points* m^{-2}. A digital terrain model (DTM) was generated from the ALS points by using TerraScan software with a grid size of 0.5 *m*. ALS point cloud was normalized to obtain a canopy height model (CHM) by subtracting the DTM from the DSM created from all ALS points.

Hyperspectral data were acquired on 13^{th} of June 2013 with an AISA Eagle II sensor. The minimum overlap among the images was 20%. Each image is characterized by 65 spectral bands acquired between 400 and 990 *nm* and by a spatial resolution of 1 *m*. The hyperspectral images were mosaicked in order to create a uniform image, and to reduce minor differences in reflectance occurring between the different images.

4
ITC Delineation

An important task for the individual tree crown (ITC) delineation is segmentation, and previous studies showed that the adaptive 3D mean shift (AMS3D) algorithm provides effective results. AMS3D for ITC segmentation has three components for the kernel profile: shape, weight and size. In this chapter, we present an AMS3D approach based on the adaptation of the kernel profile size through an ellipsoid crown shape model. The algorithm parameters are estimated based on allometry equations derived from 22 forest plots in two study sites. After computing the mean shift (MS) vector, we initialize the parameters of the ellipsoid crown shape model to derive the kernel profile size, and further tested two crown shape models for adapting the size of the superellipsoid (SE) kernel profile. These schemes are compared with two other MS algorithms with and without kernel profile size adaptation. We select the best algorithm output per plot based on the maximum F1-score. The ellipsoid crown shape model with a SE kernel profile of n = 1.5 presents the highest recall and the best Jaccard index for conifers.

Sommaire

4.1 Introduction

Decision-support systems for forest management rely on stand attribute information by collecting data on the ground in a field survey [103]. Field-based inventories are time-consuming and labor-intensive to be collected, providing rough estimates of stand attributes with typical sampling limitations because of terrain or vegetation factors [45]. Evidently, this challenging task requires all devices, methods and data available from remote sensing [257] for an analysis at tree level. Remote sensing based tools, in particular, individual tree level analysis, could contribute to producing more precise inventories; for instance, Crowther *et al*. [258] estimated the world's tree population in 3.04 trillion based on satellite imagery.

Nowadays, decision makers benefit from light detection and ranging (LiDAR) technology, which provides 3D explicit information for performing the ITC segmentation with a high accuracy level. Conventional methods for performing the individual tree crown (ITC) segmentation degrade the 3D information of the point cloud into a 2D image for applying image processing methods, which are based on local maximum filtering [95]. For 2D segmentation of crown segmentation, methods such as marker-based watershed [259], seeded region growing [159] or voronoi tesselation [260] are implemented either in *Python* or in *R* packages. A recent segmentation comparative assessment [261] remarked the superior performance of the 3D segmentation algorithms over the methods based on 2D image. In particular, the adaptive 3D mean shift (AMS3D) [97] clearly outperforms other segmentation approaches.

The mean shift (MS) algorithm [262,263] is a nonparametric method for finding the maximum value (mode) of a probability density function (PDF). Each LiDAR point contributes to the PDF based on the distribution estimated by the kernel profile. The kernel output is a weighted mean point that is shifted iteratively to locate the mode. A potential ITC is defined by a cluster of points that converge to the same mode. In [163, 264], the kernel profile shape influences consistently in the MS performance. For proving this, authors evaluate different kernel profiles: anisotropic symetric (cylinder and superellipsoid) and radially symmetric (sphere).A superellipsoid (SE) kernel profile improved the segmentation and confirmed the findings of Yilmaz [265], who points out the anisotropic symmetric kernels preserve most of the non-object region outside of the kernel.

Ferraz *et al*. in [97] proposed the adaptivity of the kernel profile size in the MS algorithm, known as AMS3D. The allometry equations for estimating the bandwidths of the cylinder kernel, are suitable for tropical forests, but this adaptation requires a performance assessment for other forest types. This chapter presents a methodology for adapting a SE kernel profile into an ellipsoid crown shape model for temperate forests. Results demonstrate that the ellipsoid adaptation provides better segmentation results for coniferous species with respect to other AMS3D approaches. This work is divided as follows: section 4.2 describes the background of MS algorithm for ITC segmentation, section 4.3 presents the main contribution of this work by adapting a crown shape model, section 4.4 describes the datasets, the parameters settings and the most important results and finally, section 4.5 corresponds to the conclusions and the work perspectives.

4.2 MS segmentation

If we consider a 3D point coordinate $\mathbf{x_i} = (X_i, Y_i, Z_i)$, the MS vector, $\mathbf{v}(\mathbf{x_i})$, is given by the equation (4.1):

$$\mathbf{v}(\mathbf{x_i}) = \frac{\sum_{\mathbf{x_j} \in N(\mathbf{x_i})} K(\mathbf{x_i}, \mathbf{x_j}) \mathbf{x_j}}{\sum_{\mathbf{x_j} \in N(\mathbf{x_i})} K(\mathbf{x_i}, \mathbf{x_j})} - \mathbf{x_i} \tag{4.1}$$

where $N(\mathbf{x_i})$ represents a set of points $\mathbf{x_j}$ in the neighborhood of $\mathbf{x_i}$ described by the kernel profile, and $K(\mathbf{x_i}, \mathbf{x_j})$ is the kernel function that weights the importance of each point $\mathbf{x_j}$ through a parameter called bandwidth. The selection of the kernel profile shape, weight and size has important variations that are studied in the subsections 4.2.1, 4.2.2 and 4.2.3.

4.2.1 Kernel profile shape

The kernel profile shape defines the distribution of the points $\mathbf{x_j}$ in the neighborhood of $\mathbf{x_i}$. Ferraz *et al.* [96] use a straightforward implementation based on a cylinder of radius r_{kc} and height h_k. Xiao *et al.* [163] propose the SE profile, $N(\mathbf{x_i})$, in equation (4.2) for selecting the set of points $\{\mathbf{x_j} \in N(\mathbf{x_i}) | N(\mathbf{x_i}) \leq 1\}$:

$$N(\mathbf{x_i}) = \frac{||\mathbf{x_i^h} - \mathbf{x_j^h}||^n}{r_k^n} + \frac{||Z_i - Z_j||^n}{a_k^n} \tag{4.2}$$

where $\mathbf{x_i} = (\mathbf{x_i^h}, Z_i)$ and $\mathbf{x_i^h} = (X_i, Y_i)$ represents the 2D components of $\mathbf{x_i}$, $\mathbf{x_j} = (\mathbf{x_j^h}, Z_j)$ is a point in the neighborhood formed by the SE kernel profile with center at $\mathbf{x_i}$, a_k is the radius of the intersection of the kernel profile with the z-axis, r_k is the radius of the kernel profile circle in xy-plane, and n is a positive real number that determines the shape of the kernel profile. An ellipsoid emerges when $n = 2$, and it becomes a cone when n decreases to 1.

4.2.2 Kernel profile weight

Following the multivariate kernel proposed by Comaniciu *et al.* [262] for image segmentation, the kernel weight $K(\mathbf{x_i}, \mathbf{x_j})$ proposed by Ferraz *et al.* [96] is given in equation (4.3)

$$K(\mathbf{x_i}, \mathbf{x_j}) = K_h\left(\mathbf{x_i^h}, \mathbf{x_j^h}, w_h\right) K_z(Z_i, Z_j, w_z) \tag{4.3}$$

where K_h is the horizontal kernel weight, K_z is the vertical kernel weight, w_h and w_z are their respective bandwidths, which depend on the kernel profile shape. Ferraz *et al.* [96] use the Gaussian function for the horizontal kernel weight and Epanechnikov function K_z^F for the vertical kernel weight presented as follows in equations (4.4) and (4.5), respectively:

$$K_h\left(\mathbf{x_i}, \mathbf{x_j}, w_h\right) = \exp\left(-\gamma \left|\left| \frac{\mathbf{x_i^h} - \mathbf{x_j^h}}{w_h} \right|\right|^2\right) \tag{4.4}$$

$$K_z^F(Z_i, Z_j, w_z) = 1 - \left|\left|1 - d(Z_i, Z_j, w_z)\right|\right|^2 \tag{4.5}$$

where $\gamma = 5$, $w_h = 2 \times r_{kc}$ (diameter of the cylinder kernel profile) and $d(Z_i, Z_j, w_z)$ is the vertical distance function between the point and the mask boundary obtained in expression (4.6)

$$\begin{aligned} d(Z_i, Z_j, w_z) &= min\{d_{inf}, d_{sup}\} \\ d_{inf} &= \left|\left| \frac{\left(Z_i - \frac{1}{4}h_k\right) - Z_j}{\frac{1}{2}w_z} \right|\right| \\ d_{sup} &= \left|\left| \frac{\left(Z_i + \frac{1}{2}h_k\right) - Z_j}{\frac{1}{2}w_z} \right|\right| \end{aligned} \tag{4.6}$$

where $Z_j \in \left[Z_i - \frac{1}{4}h_k, Z_i + \frac{1}{2}h_k\right]$ and $w_z = \frac{3}{4} \times h_k$. The variables d_{inf} and d_{sup} are explained in equation (13) in [96]. If Z_i is the height of a point $\mathbf{x_i}$, Z_j corresponds to the height of a point in the neighborhood of $\mathbf{x_i}$, which is described by the asymmetric profile cylinder of height, h_k: $\left[Z_i - \frac{1}{4}h_k, Z_i + \frac{1}{2}h_k\right]$. The variables d_{inf} and d_{sup} quantify the distance between Z_j and the vertical

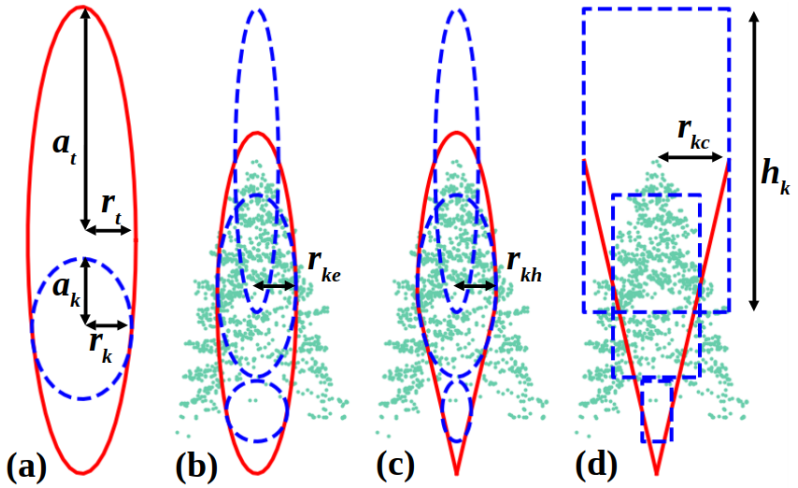

Figure 4.1: Three different crown shape models in red line: (a) and (b) ellipsoid, (c) hybrid model and (d) inverted cone; and two kernel profiles in dotted blue line: SE in (a), (b) and (c), and cylinder in (d). In (a), we illustrate the parameters of the ellipsoid crown model and the SE kernel profile.

boundaries of the profile cylinder, weighted by the half of the vertical bandwidth $w_z = \frac{3}{4} \times h_k$. The minimum value between d_{inf} and d_{sup} defines the vertical distance function between the point and the mask boundary.

Another combination is proposed by Xiao *et al.* [163] whose horizontal kernel weight K_h is a Gaussian function with $\gamma = 0.5$ (normal distribution), and the vertical kernel weight K_z^X is described in equation (4.7)

$$K_z^X(Z_i, Z_j, w_z) = \left|\left| \frac{Z_j - Z_{min}}{w_z} \right|\right| \tag{4.7}$$

where $w_z = Z_{max} - Z_{min}$, corresponds to the difference between the maximum and minimum height values in the kernel profile by weighting on higher points to converge at the top of a tree.

4.2.3 Kernel profile size

Following the tree size allometry equations, Ferraz *et al.* [97] compute the radius r_{kc} and the height h_k of the cylinder kernel profile, by using equations (4.8) and (4.9)

$$r_{kc} = m_1 Z_i \tag{4.8}$$

$$h_k = m_2 Z_i \tag{4.9}$$

where m_1 represents the slope of the linear regression between the tree height and the crown radius, and m_2 is the slope between the tree height and the crown depth. In Fig. 4.1(d), this kind of adaptive kernel size leads to fit an inverted cone as long as it moves on the z-axis. Although this approach has been assessed for tropical forests by dealing with wide crowns, coniferous trees that are present in temperate forests, are better described by narrow clusters in the upper parts of the canopy. As a consequence, the inverted cone approach would lead to an undersegmentation effect by merging adjacent coniferous tree crowns. An alternative solution to this problem is presented by Xiao *et al.* [163] by testing different profile sizes with and without adapting the kernel profile size. In this work, we compare the previous strategies for controlling the kernel profile size with our AMS3D approach.

4.3 AMS3D based on crown shape model

Our objective is to adapt the SE kernel profile size by fitting it into an ellipsoid crown model, using the parameters m_1 and m_2 (Fig. 4.1(a)). If the tree crown model is defined by the crown radius r_t in xy-plane and the radius of the intersection of the crown model along the z-axis, a_t, it is possible to derive the parameters of the SE kernel profile r_k and a_k as it is illustrated in Fig. 4.1(a). Previously, a preprocessing stage is applied in the 3D point cloud by removing the points less than $h_{min} = 1.5\ m$ [170]. The negative effects of shrubs, grassland and low height objects are avoided by applying this threshold.

The main core of AMS3D is described in Algorithm 1. The algorithm is initialized with a point $\mathbf{x_i}$ and a set of parameters $m = \{m_1, m_2\}$. The output variable $\mathbf{u_i}$ is the mode derived from $\mathbf{x_i}$. The kernel parameters r_k and a_k are initialized by the equations (4.8) and (4.9), respectively. The parameter a_k is assumed to be half of the cylinder height h_k. These parameters determine the neighborhood $N(\mathbf{u_i})$ by using equation (4.2) and to estimate the weighted mean $\mathbf{u_{i+1}}$. If the euclidean distance, Δ_u, between $\mathbf{u_{i+1}}$ and $\mathbf{u_i}$ is less than 1×10^{-7} (threshold selected empirically), then MS vector (equation (4.1)) converges and $\mathbf{u_{i+1}}$ becomes a mode. This is recorded and the next point $\mathbf{x_{i+1}}$ is evaluated. If not, a new MS vector is recomputed, $\mathbf{u_i} = \mathbf{u_{i+1}}$, until it converges. The incorporation of the crown shape model for controlling the kernel size is executed when the MS vector does not converge ($\Delta_u \geq 1 \times 10^{-7}$). Although this is the general discrimination condition to verify if the weighted mean becomes a mode, the kernel profile contains internally the next discrimination conditions:

- To compute the mode $\mathbf{u_i}$ of a point $\mathbf{x_i}$ in the AMS3D algorithm, the number of points in the neighborhood $N(\mathbf{u_i})$ should be greater than 1, otherwise $\mathbf{u_i} = \mathbf{u_{i+1}}$.
- If the vertical distance, Δ_{uv}, between the maximum and the minimum points in the neighborhood $N(\mathbf{u_i})$ is less than 1×10^{-7} (approximately 0), then we weight the MS vector by using the horizontal kernel (Gaussian function) only.
- If the maximum horizontal distance, Δ_{uh}, of the points in the neighborhood $N(\mathbf{u_i})$ with respect to $\mathbf{u_i}$ is less than 1×10^{-7} (approximately 0), then we weight the MS vector by using the vertical kernel (Epanechnikov function, K_z^F) only.
- If Δ_{uv} and Δ_{uh} are less 1×10^{-7}, then $\mathbf{u_i} = \mathbf{u_{i+1}}$.

The point of maximum height h_{max} is searched in the cylindrical neighborhood $C(\mathbf{u_i})$ of radius r_k and infinite height. The tree crown parameters r_t and a_t are obtained from equations (4.10) and (4.11):

$$a_t = \frac{1}{2}(h_{max} + h_{min}) \tag{4.10}$$

$$r_t = (h_{max})^{\alpha}. \tag{4.11}$$

Equation (4.11) comes from the allometry relationship between the tree height and the crown radius used for 3D ITC segmentation [98]. The parameter α is estimated by equating the expressions (4.8) and (4.11), when $Z_i = a_t$. This means that the kernel profile radius should be equal to the tree crown radius around half of the tree height. It turns out the expression (4.12)

$$\alpha = \frac{\log(m_1 a_t)}{\log(h_{max})}. \tag{4.12}$$

Once the parameters a_t and r_t are obtained, the kernel radius, r_{ke}, from the ellipsoid crown model (Fig. 4.1(b)) that controls the radius r_k (Fig. 4.1(a)) from the SE kernel from equation (4.2), is derived from the ellipse equation in (4.13)

Algorithm 1: AMS3D with ellipsoid crown model

Input: $\mathbf{x_i}$ - 3D LiDAR point.
Parameter: m_1 and m_2 - Allometry coefficients.
Data: $\{\mathbf{x_i}, ..., \mathbf{x_N}\}$ - 3D point cloud.
Output: $\mathbf{u_i}$ - Mode of the point $\mathbf{x_i}$.
for *i = 1,..,N* **do**
  Initialize $\mathbf{u_i} \leftarrow \mathbf{x_i}$, $r_k \leftarrow m_1 Z_i$, $a_k \leftarrow \frac{1}{2} m_2 Z_i$, and $\Delta_u \leftarrow 10^7$;
  while $\Delta_u \geq 10^{-7}$ **do**
    $\mathbf{u_{i+1}} \leftarrow \frac{\sum_{\mathbf{u_j} \in N(\mathbf{u_i})} K(\mathbf{u_i}, \mathbf{u_j}) \mathbf{u_j}}{\sum_{\mathbf{u_j} \in N(\mathbf{u_i})} K(\mathbf{u_j}, \mathbf{u_i})}$;
    $\Delta_u \leftarrow ||\mathbf{u_{i+1}} - \mathbf{u_i}||$;
    $\mathbf{u_i} \leftarrow \mathbf{u_{i+1}}$;
    if $\Delta_u \geq 10^{-7}$ **then**
      $h_{max} \leftarrow \max_{\mathbf{u_j} \in C(\mathbf{u_i})} (Z_j)$;
      Compute a_t and r_t according to (4.10) and (4.11);
      Compute r_{ke} according to (4.13) ;
      Update $r_k \leftarrow r_{ke}$ and $a_k \leftarrow \frac{1}{2} m_2 Z_i$;
    else
      break;

$$r_{ke} = \frac{r_t}{a_t} \sqrt{2 a_t Z_i - Z_i^2}. \tag{4.13}$$

The parameter a_k is updated based on the new estimation of Z_i, and $r_k = r_{ke}$. In addition to the ellipsoid crown model, a hybrid crown model (Fig. 4.1(c)) is implemented by using the same a_k parameter and by computing a hybrid kernel radius value $r_{kh} = \min(r_{kc}, r_{ke})$ in order to set $r_k = r_{kh}$.

4.4 Experimental analysis

For the experimental setup, Table 4.1 presents a description of six different AMS3D models assessed in this work. Model F represents the adaptive approach of Ferraz *et al.* [97] with cylinder (C) kernel profile (Fig. 4.1(d)). The remaining models implement the (SE) kernel profile from equation (4.2). Model X represents the approach of Xiao *et al.* which has two parameters, r_k and b, for estimating $a_k = b \times r_k$, but no kernel size adaptation. Models E1 and E2 introduce the ellipsoid crown model (Fig. 4.1(b)), while models H1 and H2 implement the hybrid crown model (Fig. 4.1(c)), with $n = \{1.5, 2.0\}$.

For the algorithm evaluation, the cluster points detected as a potential tree from each algorithm, are projected into the *xy*-plane for computing the 2D centroid and for fitting an ellipsoidal crown shape. For every detected tree, we pair with a tree in the inventory based on the matching index, I_{TC}, which is the ratio of the distance between the assumed tree top and detected maxima, and the matching distance described in [95].

The matching index I_{TC} is the ratio of the distance between the assumed tree top and detected maxima, and the matching distance. The equation is described by using the following expression:

$$I_{T,C} = \frac{d_{T,C}}{d_{max}(h_t)} \tag{4.14}$$

Table 4.1: AMS3D configurations based on the kernel profile

AMS3D	Shape		Weight		Size	
Model	Type	n	K_h	Vertical	Radius	Height
F [97]	C	-	$\gamma = 5.0$	K_z^F	r_{kc}	h_k
X [163]	SE	1.5	$\gamma = 0.5$	K_z^X	r_k	a_k
E1	SE	1.5	$\gamma = 5.0$	K_z^F	r_{ke}	a_k
E2	SE	2.0	$\gamma = 5.0$	K_z^F	r_{ke}	a_k
H1	SE	1.5	$\gamma = 5.0$	K_z^F	r_{kh}	a_k
H2	SE	2.0	$\gamma = 5.0$	K_z^F	r_{kh}	a_k

Table 4.2: Summary of the field measurements at tree level

	No.	Average			Species	
Study site (No. Plots)	Tree Crown	DBH [cm]	Tree Height [m]	Crown Area [m^2]	CON [%]	BRO [%]
Chamrousse (7)	894	26.2	14.8	23.3	79.8	20.2
Pellizzano (15)	543	29.4	19.6	17.8	87.8	12.2

where the matching distance $d_{max}(h_t)$ is given by

$$d_{max}(h_t) = \frac{\varepsilon_{gps}}{cos(s_{terrain})} + s_{tree} \times (\varepsilon_h + 1) \times h_t \tag{4.15}$$

where ε_{gps} is the GPS positioning planimetric error (0.97 m, $s_{terrain}$ is the terrain slope (0.25), s_{tree} is the slope of a tilted tree (14%), ε_h is the height measures accuracy (15%), h_t is the height of the tree and $d_{T,C}$ is the Euclidean distance between detected and reference treetops. This index I_{TC} can be computed in an R package *lidaRtRee*.

This index is multiplied by the Jaccard distance $J_d = 1 - J_i$, where J_i is the Jaccard index equal to $\frac{V_R \cap V_D}{V_R \cup V_D}$, V_R and V_D are the tree volume from reference (ground truth inventory) and from detections, based on the ellipse area and the tree height. When the potential pair with the lowest matching factor $J_d \times I_{TC}$ is validated, the lists of remaining detected and reference trees are updated before moving to the next pair. The number of matched trees are called true positives (TP), N_R is the number of reference trees in the inventory and N_D is the number of detected trees. Then, three metrics are computed: Recall= TP/N_R, Precision= TP/N_D and F1-score.

4.4.1 Dataset

The characteristics of 1437 trees from two study sites [252] are summarized in Table 4.2 with average values of: diameter at breast height (DBH), tree height and crown area. The percentage of conifers (CON) and broadleaves (BRO) are also reported. The study areas corresponds to the Chamrousses site, located in Belledonne massif, Northern Alps, France; and the Pellizzano site located in the Italian Alps [170]. The description of both study sites are given in chapter 3, in the subsection 3.2. The remote sensing data description of LiDAR and hyperspectral data is detailed in subsection 3.3.

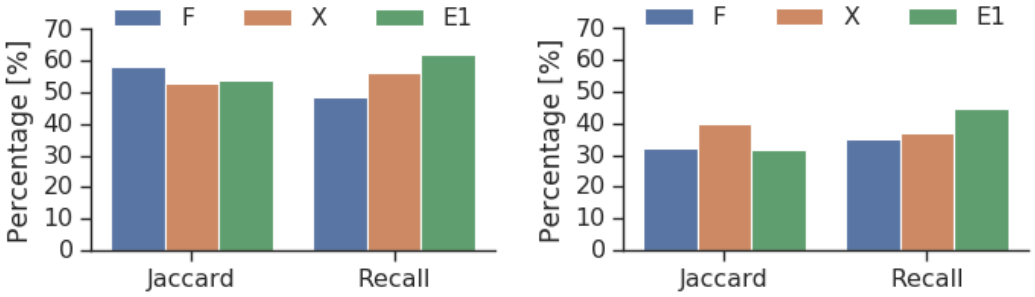

(a) Conifers (1190)

(b) Broadleaves (247)

Figure 4.2: Algorithm comparison assessment based on species: (a) 1190 conifers and (b) 247 broadleaves from the sites in Pellizzano and Chamrousse.

4.4.2 Parameters

For the algorithms F, E1, E2, H1 and H2; the parameters m_1 and m_2 are computed for every plot on the basis of the ground truth information. For every linear regression, we obtain two confidence intervals (CI) at 95.0% and 99.9% for generating a set of 5 values per parameter: the slope value, the upper and lower limits of the two CI. In this way, we run 25 experiments per algorithm in each plot. The mean value of parameter m_1 is 0.131 with minimum and maximum values between 0.025 and 0.316. The parameter m_2 has a mean value of 0.786 with minimum and maximum values between 0.143 and 0.969. The parameters for the model X are selected according to [163], where $r_k = \{2,3\}$ and $b = \{1,1.5,2,2.5,3\}$.

4.4.3 Results and discussion

The overall performance of six AMS3D segmentation schemes are summarized in Table 4.3 based on four metrics: average J_i, recall, precision and F1-score. The best results per plot were selected according to the parameter setting with the maximum F1-score. Although F1-score values were similar among the algorithms with ellipsoid and hybrid crown model, the algorithm E1 presented the highest recall, *i.e.* the greatest amount of matched trees, and the highest average J_i, *i.e.* the best ITC segmentation. Algorithm F produced undersegmented tree crowns because the kernel radius enclosed more than one tree at upper layers. This issue is solved in our method by adjusting the crown radius. Algorithm X maximized F1-score by decreasing the number of detections, which produced the best precision with respect to other algorithms, but it decreased the number of TP trees. This algorithm produced better recall values with small kernels by oversegmenting the point cloud.

Table 4.3: Overall assessment of 6 AMS3D schemes based on 22 forest plots from two study sites

AMS3D	J_i [%]	Recall [%]	Precision [%]	F1-score [%]
F [97]	49.1	46.1	72.0	56.2
X [163]	48.5	52.8	74.3	61.7
E1	**53.7**	**59.0**	67.4	62.9
E2	52.2	57.1	70.7	63.1
H1	52.6	58.2	67.3	62.4
H2	52.3	58.0	68.4	62.8

The algorithm E1 is assessed in each study site to remark differences of the point density. The recall values in the sites of Chamrousse and Pellizzano were 56.6% and 63.0%, respectively. Although the pulse density of Pellizzano site is three times Chamrousse's pulse density, the recall difference between these two sites did not respond in that magnitude. Other factors described in Table 4.2 can contribute for E1 to deliver better performance in Pellizzano. For instance, the average tree height is greater in Pellizzano than Chamrousse, presenting more salient trees which are easy to be segmented. Also, the Pellizzano site has 8.0 points of percentage more conifers than Chamrousse site.

For the species analysis, an important finding of the algorithm performances is presented in Fig. 5.8, which corresponds to the results of the segmentation for coniferous and broadleaves species. In Fig. 4.2(a), E1 obtains the highest recall of 62.0% for conifers by reaching a difference of 5.9 points of percentage over the algorithm X and 13.6 over F. This difference is compensated for algorithm F that had the best J_i: 58.2%, 3.8 points of percentage better than algorithm E1. For broadleaves (Fig. 4.2(b)), none of the presented algorithms performed a recall over 50.0% and J_i better than 40.0%.

For discussing the species results at plot level, two conifers plots and two forest plots with more than 50% of broadleaves are selected from both study sites. The histogram of heights are computed by setting a bin size of 5 *m* for TP, false negative (FN) and false positive (FP) tree detections. In addition, the estimation of the gap area can be used as a forest structure descriptor. The gap area percentage (GAP) is estimated from the rate between the gap area given by a height threshold every 1 *m* and the maximum gap area surface (approximately the forest plot surface) calculated in an R package *ForestGapR* [266]. The resulting curve overlaps each height histogram in Fig. 4.3.

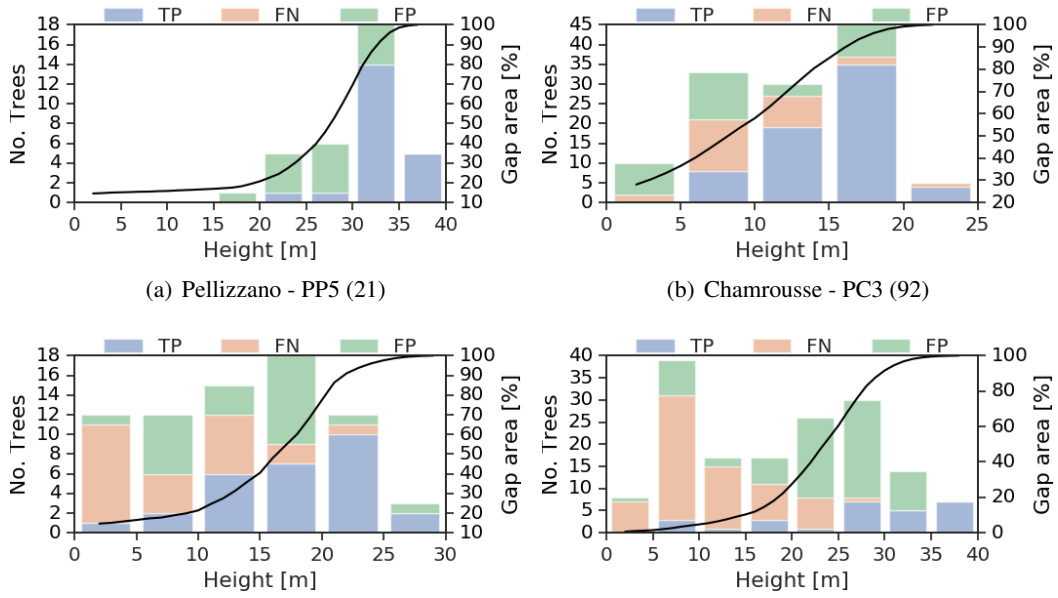

(a) Pellizzano - PP5 (21)

(b) Chamrousse - PC3 (92)

(c) Pellizzano - PP1 (51)

(d) Chamrousse - PC1 (92)

Figure 4.3: Histograms of heights for the TP, FN and FP trees in the conifers plots: (a) plot 5 from Pellizzano (PP5) and (b) plot 3 from Chamrousse (PC3). Below, the plots with more than 50% of broadleaves: (c) plot 1 from Pellizzano (PP1) and (d) plot 1 from Chamrousse (PC1). The GAP curve is represented in black.

In Fig. 4.3, plot 5 from Pellizzano, PP5, (Fig C.25(a)) and plot 3 from Chamrousse, PC3, (Fig. C.25(b)) obtained the highest recalls: 100% and 72.7%, respectively. PP5 revealed the ideal scenario for ITC segmentation. E1 detected all the 21 conifers (small plot), whose heights were greater than 20 *m* (salient trees). As the GAP curve increased, the number of TP and FP trees

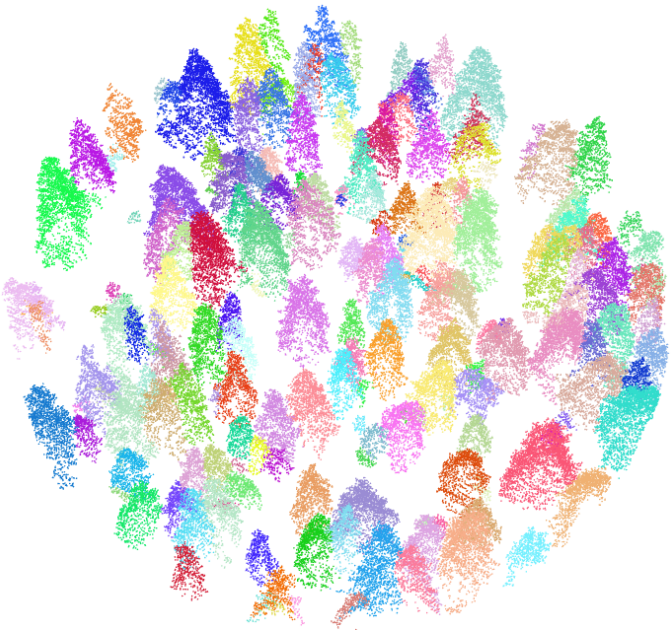

Figure 4.4: 3D segmentation of PC3 by using algorithm E1. 66 trees out of 92 were matched, resulting in a recall of 71.7% *and a Jaccard index of* 54.5%.

increased, because tree crowns became more sparse when the GAP value overpasses 20.8%. The forest structure of conifers has more sparse upper canopy layers with prominent gap areas. In contrast to PP5, the majority of trees in PC3 are less than 20 *m* (Fig. 4.4).

Although PC3 showed a GAP value of 36.5% at 5 *m*, E1 faced difficulties to segment understory trees because the crown shape model that controls the kernel size is calibrated with the height of the highest point, which makes it suitable for salient trees. In Fig. 4.3, plot 1 from Chamrousse, PC1, (Fig. C.25(g)) and plot 1 from Pellizzano, PP1, (Fig C.25(c)) obtained lower recalls: 29.3% and 54.9%, respectively. Two aspects are remarked in these plots. First, most of the trees are located at the lower canopy layers (tree heights less than 20 *m*). It increased the amount of FN trees with respect to the conifers plots. Second, the canopy of these plots is dense with low GAP values at the lower canopy layers: 1.5% at 5 *m* in PC1 and 14.6% at 2 *m* in PP1. This makes it difficult to segment groups of understory trees that belong to the same species because a dense point cloud can lead to undersegmentation. If the LiDAR point density is very low, the clusters that represent potential ITC become noisy and have low definition to be delineated.

4.5 Conclusion

In this chapter, we presented an AMS3D approach for ITC segmentation by adapting the kernel profile size through crown shape model and by exploring the optimal parameters. The ellipsoid crown shape model with a SE kernel profile of $n = 1.5$ presents the best overall recall of 59.0% and Jaccard index of 53.7% among the assessed schemes of 3D segmentation. The most outstanding results of the algorithm are revealed for the coniferous trees. Forest plots with a high presence of broadleaves trees represent challenging tasks for all ITC segmentation approaches. Future work is going to be focused on estimating automatically the algorithm parameters in order to consolidate a tool for end-user purposes. This task will involve the integration with other data modalities, such as hyperspectral imaging for tree species prediction.

5

Tree Species Classification

This chapter presents the integration of feature descriptors from hyperspectral image (HI) and LiDAR by using the intra-set and inter-set feature importance for the semantic segmentation of forest tree species. A fusion methodology is proposed between high-density LiDAR data and VNIR HI acquired on French temperate forests along an altitude gradient. The proposed scheme has three inputs: the field inventory information, the HI and the LiDAR data. Our approach can be described in eight stages: polygon projection, non-overlapping pixel selection, computation of vegetation indices (VI), LiDAR feature extraction, robust PCA (rPCA), height, vegetation and shadow mask, feature reduction and classification. The overall accuracy of tree species classification at pixel-level was 78.1% *by using random forest (RF) classifier,* 78.3% *of trees were correctly assigned overall, by having conifers such as Norway Spruce and mountain pine with producer's accuracies above* 90%.

Sommaire

5.1 Introduction

Spatial distribution of forest tree species has important benefits for sustainable forest management [232]. For instance, scientists are able to study the functioning of forested ecosystems by understanding variables associated to stress, disease patterns, invasive species spread and deforestation [127, 232]. This information is very relevant to establish useful exploitation policies of forests [122]. Conventional ecological survey methods of tree species mapping require an exhaustive work that thrives in difficult scenarios, relies on small plot-level datasets and implies a significant amount of time, manpower and economic resources [144, 232].

Several studies have highlighted the potential of spectral and spatial resolution in remote sensing based tools for monitoring forest ecosystems. Hyperspectral images (HI) and Light Detection and Ranging (LiDAR) provide high resolution radiometric and geometric information for monitoring forests at individual tree crown (ITC) level. The advances in the integration of LiDAR and hyperspectral sensors make possible to identify tree species at pixel-level with a high accuracy. The integration of different remote sensing modalities is a challenging task for tree species classification due to different artifacts such as the lighting variability, the topographic effects and the atmospheric conditions of the data acquisition. The characterization of ITC can benefit from the extraction and selection of robust feature descriptors that solve these issues.

Data fusion is implemented at three levels: observation-level, feature-level and decision-level [252]. Considering that tree species identification is a remote sensing topic posed as a supervised approach [267], recent studies pursue to integrate HI and LiDAR data for improving the classification (decision-level fusion). In [135], features are extracted from the HI by applying principal component analysis (PCA) for reducing the redundancy within the bands [130]. In [127], the algorithm rPCA is applied for filtering the noise and for selecting relevant features. This study demonstrated that rPCA improved the classification of six tree species over PCA, with an overall accuracy of 61.0% at tree-level. The algorithms support vector machines (SVM) [127] and RF [76, 268] have been used for tree species classification with HI. Although SVM performs superior for high dimensional features, it requires a proper parameter-setting that can be time-consuming for large datasets. Alternatively, RF can be a good choice for feature selection (feature-level fusion) and classification [269].

In this chapter, we present the integration of HI and LiDAR data for the classification of four forest tree species. First, we compute the vegetation indices (VI) from HI, we extract LiDAR features from the 3D point cloud and we compute the principal components (PC) by using robust PCA (rPCA). Second, we create the dataset from the field survey data explained in section 3.1. The pixels selected for the dataset are according to three criteria: height, vegetation and shadow. The amount of features created can be reduced by considering the intra-set and inter-set feature importance by using the RF scores and the 5-fold cross validation. Finally, we apply RF for the pixel classification. This work is divided as follows: section 5.2 refers to the study site and the data acquisition, section 5.3 presents the contributions based on feature extraction, feature selection and classification based on RF, section 5.4 discusses the results of feature fusion for the classification and finally, section 5.5 corresponds to the conclusions and the work perspectives.

5.2 Study area

The study area corresponds to the site of Chamrousse, located in Belledonne massif, Northern Alps, France. The description of the study site is given in chapter 3, in the subsection 3.2.1 with the summary of the field measurements at tree- and plot- level in Table 3.1. The remote sensing data description of LiDAR and hyperspectral data is detailed in subsection 3.3.1.

5.3 Methodology

The semantic segmentation workflow for forest tree species classification is presented in Figure 5.1. The proposed scheme has three inputs: the field inventory information, the HI and the LiDAR data. This approach comprises the following steps: polygon projection, non-overlapping pixel selection, computation of vegetation indices (VI), LiDAR feature extraction, robust PCA (rPCA), height vegetation and shadow mask, feature reduction and classification.

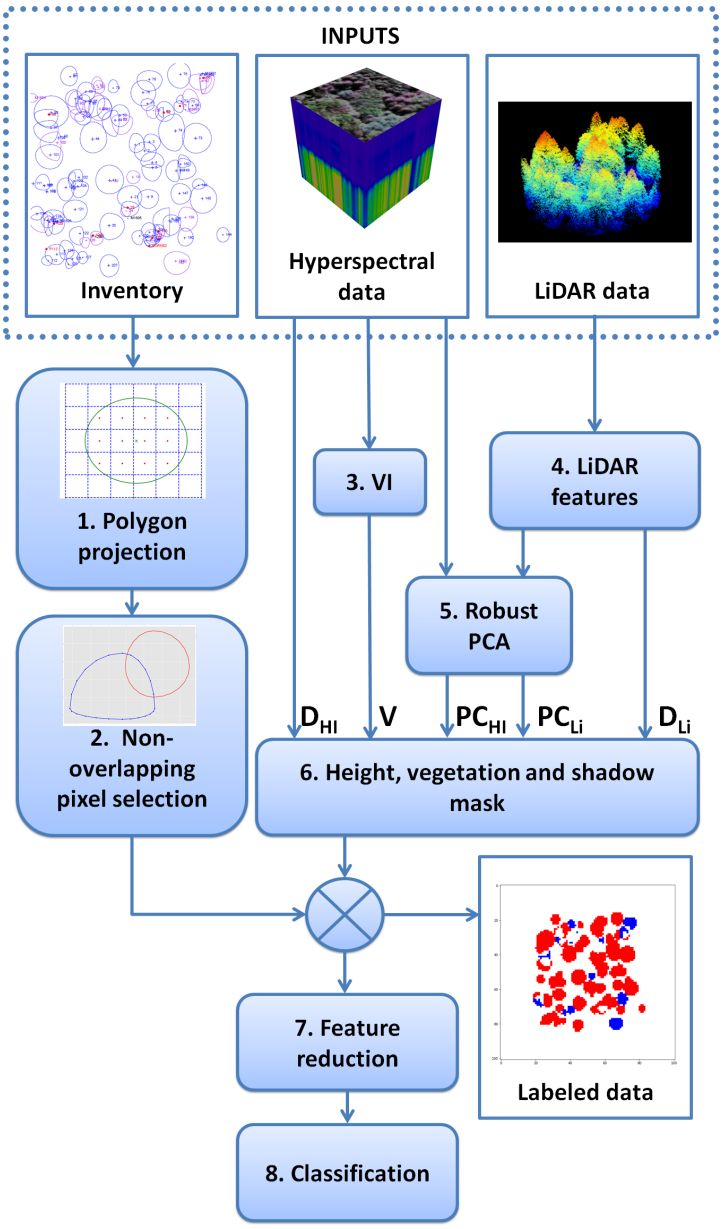

Figure 5.1: Semantic segmentation flowchart for forest tree species classification by integrating HI and LiDAR data. Five types of feature sets are evaluated: the hyperspectral bands represented in matrix $\mathbf{D_{HI}}$*, the vegetation indices in* $\mathbf{V}$*, the PC obtained by using rPCA from HI in* $\mathbf{PC_{HI}}$*, the LiDAR features in* $\mathbf{D_{Li}}$ *and the PC obtained by using rPCA from LiDAR in* $\mathbf{PC_{Li}}$*.*

5.3.1 Polygon projection

Each tree crown from the inventory is projected into the xy-plane by fitting an ellipsoidal crown shape. Then, a HI pixel is associated with a crown by verifying if the pixel center coordinate is inside the crown polygon. The pixel center coordinate, (x_c, y_c), is computed through the following equations:

$$\begin{aligned} x_c &= (2c_i + 1)s_f + x_0 \\ y_c &= y_0 - (2r_i + 1)s_f \end{aligned} \tag{5.1}$$

where (x_0, y_0) is the xy coordinates for the upper-left pixel in the image, s_f is the half of the spatial resolution of the image, and (r_i, c_i) are the coordinates for the row and the column pixel positions in the image ($r_i \in \{0, ..., m\}$ and $c_i \in \{0, ..., n\}$ with an image size $m \times n$.

5.3.2 Non-overlapping pixel selection

The crown pixel correspondence becomes challenging when some crown regions overlap among each other. To overcome this issue, those overlapping pixels that are associated with crown trees of different species, are not considered in our ground truth. The purpose is to select a representative set of pure pixels for each species. The overlapping pixels for those trees of the same species, are labeled to the tree with the greatest height and crown area. This pixel - tree association is relevant when the training and testing sets are defined for the classification.

5.3.3 Vegetation indices (VI)

In section 2.3.1 of feature extraction, we describe a list of 61 vegetation indices divided in 5 groups according to the following tables: broadband greenness in Table 2.5, narrowband greenness in Table 2.6, light use efficiency in Table 2.7, leaf pigments in Table 2.8, dry or senescent carbon and canopy water content in Table 2.9. We compute these 61 features by using the equations summarized in Annex B of feature descriptors.

5.3.4 LiDAR features

From the LiDAR 3D point cloud, 72 LiDAR features are computed at point-level according to [165]. The equations of these features are presented in in Annex B:

- Two vegetation density features: the cumulative sum of local height maxima retrieved from each radius r_f maximum filter within three cylindrical neighborhoods of radius $r_c \in \{1.0, 3.0, 5.0\}$ m. The second feature is computed from the number of points classified as ground points over the total number of points within each cylindrical neighborhood of radius r_c. The three outputs of the neighborhoods for every point are stacked.

- Two shape features: the scatter and the planarity are computed from the eigenvalues of the covariance matrix within the three cylindrical neighborhoods of radius r_c.

- 20 statistical features from each LiDAR point using the cylindrical neighborhoods given in r_c. The height and intensity information from the LiDAR data are used to derive statistical features: minimum; maximum; mean; median; standard deviation; median absolute deviation from median; mean absolute deviation from median; mean absolute deviation from mean; skewness; kurtosis; 10^{th}, 20^{th}, 30^{th}, 40^{th}, 50^{th}, 60^{th}, 70^{th}, 80^{th}, 90^{th} and 95^{th} percentiles. All the statistical functions are used for the height, while the mean is used for the intensity only.

After computing the LiDAR features at point-level, these features are rasterized at the resolution of the HI, s_c. The feature values of the points inside the pixel that is centered at the coordinate $\mathbf{x} = (x_c, y_c)$, are weighted according to the function $W(\mathbf{x})$

$$\begin{aligned} W(\mathbf{x_i}) &= W_h(\mathbf{x_i}) W_v(\mathbf{x_i}) \\ W_h(\mathbf{x_i}) &= \exp\left(-\gamma \left|\left| \frac{\mathbf{x} - \mathbf{x}_i}{w_h} \right|\right|^2\right) \\ W_v(\mathbf{x_i}) &= \left|\left| \frac{Z_i - Z_{min}}{w_z} \right|\right| \end{aligned} \tag{5.2}$$

where W_h and W_v are the weighting functions of the horizontal and vertical information, respectively. The point $\mathbf{x_i}$ represents the xy coordinate of each 3D point inside the cylinder, γ is selected to be 0.5 (normal distribution), w_h is an horizontal bandwidth equal to $\sqrt{2}s_c$, Z_i represents the z coordinate of each 3D point inside the pixel and $w_z = Z_{max} - Z_{min}$, corresponds to the difference between the maximum and minimum height 3D point values in the vertical weighting function, W_v. These weighting functions have been used for finding the maximum value of the 3D point cloud distributions for 3D segmentation purposes [163]. In this way, the information of the highest points close to the pixel center are given more importance because these are associated to the most illuminated regions in the image.

5.3.5 Robust PCA

From a given data matrix of size $m \times n$, PCA can generate a low-rank matrix $\mathbf{L}$ that minimizes the error $\mathbf{S} = \mathbf{D} - \mathbf{L}$:

$$\min_{\mathbf{L},\mathbf{S}} ||\mathbf{S}||_F, \text{ s.t.} \operatorname{rank}(\mathbf{L}) \leq r, \ \mathbf{D} = \mathbf{L} + \mathbf{S} \tag{5.3}$$

where $r \ll \min(m,n)$ is the target rank of $\mathbf{D}$ and $||\cdot||_F$ is the Frobenius norm. Although PCA is widely used as dimensionality reduction technique, it can be affected by large-amplitude noise. rPCA [127] is a method proposed to improve the robustness of the PCA for dealing with outliers. This algorithm pursues to recover a low-rank matrix $\mathbf{L}$ from highly noisy measurements $\mathbf{D} = \mathbf{L} + \mathbf{S}$, by separating a sparse matrix $\mathbf{S}$. Given the matrix $\mathbf{D}$, the matrices $\mathbf{L}$ and $\mathbf{S}$ are computed by satisfying the following condition:

$$\min_{\mathbf{L},\mathbf{S}} \operatorname{rank}(\mathbf{L}) + \lambda ||\mathbf{S}||_0, \text{ s.t.} \mathbf{L} + \mathbf{S} = \mathbf{D} \tag{5.4}$$

where $||\cdot||_0$ is the l_0-norm, λ is a regularization parameter for balancing the importance between the ranking operator and the sparsity regularization. Equation (5.4) is reformulated as a convex optimization approach:

$$\min_{\mathbf{L},\mathbf{S}} ||\mathbf{L}||_* + \lambda ||\mathbf{S}||_1, \text{ s. t.} \mathbf{L} + \mathbf{S} = \mathbf{D} \tag{5.5}$$

where $||\cdot||_*$ is the nuclear norm, which is the sum of singular values of $\mathbf{L}$; and $||\cdot||_1$ is the l_1-norm. In [270], authors described the programming implementation of the rPCA algorithm. In this stage, the matrices $\mathbf{L}$ and $\mathbf{S}$ are obtained from the HI, $\mathbf{D_{HI}}$, and the rasterized LiDAR features, $\mathbf{D_{Li}}$, separately. From the matrix $\mathbf{L}$, we compute the PC for each modality as it is explained in [156].

5.3.6 Height, vegetation and shadow mask

The purpose of the height mask is to avoid negative effects due to shrubs, grassland and low height objects. A threshold value of $h_{min} = 1.5\ m$ [170] is applied over the digital surface model (DSM) for preserving most of the forest regions. At this point, by merging all the criteria of specie purity, pixel illumination and height information, a set of n_{lp} labeled pixels associated with $n_{HI} = 160$ hyperspectral bands and $n_{Li} = 72$ rasterized LiDAR metrics is processed in the next stage.

The selection of sunlit pixels is advised because shadowed pixels are affected from a low signal-to-noise ratio (SNR) [86]. Several strategies have been proposed for shadow removal. In our approach, the criterion explained by [79], estimated the average of the blue portion of the spectrum in the range of $[450, 550]$ *nm*. Then, Otsu threshold is calculated over this range. Since the Otsu threshold value removed approximately 50.0% of the pixels, the minimum threshold is computed to preserve around 65.0% of our ground truth.

The normalized difference vegetation index (NDVI) is used to separate forest from non-vegetation [271]. In [161], authors selected a NDVI value greater than 0.5 to consider well-lit, leafy vegetation pixels. In [137], they used a threshold of 0.6 based on the average NDVI for all crowns. For our approach, a NDVI value of 0.55 is applied for all forest plots.

5.3.7 Feature reduction

From the workflow presented in Figure 5.1, we are considering 5 types of feature sets: the hyperspectral bands represented in matrix $\mathbf{D_{HI}}$, the vegetation indices in $\mathbf{V}$, the PC obtained by using rPCA from HI in $\mathbf{PC_{HI}}$, the LiDAR features in $\mathbf{D_{Li}}$ and the PC obtained by using rPCA from LiDAR in $\mathbf{PC_{Li}}$. The feature selection for $\mathbf{D_{HI}}$, $\mathbf{V}$ and $\mathbf{D_{Li}}$ was carried out by calculating the RF scores to estimate the intra-set feature importance. For instance, let $\mathbf{A}$ be a feature set of 5 features $A = [\mathbf{a_1}, \mathbf{a_2}, \mathbf{a_3}, \mathbf{a_4}, \mathbf{a_5}]$, then, the RF scores s_i are computed for the i-th feature by using 5-fold cross validation. Figure 5.2 illustrates the 6 subsets in which the dataset is divided. From this data distribution, 5 subsets are in the training set and the remaining one is used for testing. Since RF score $s_i \in [0, 1]$, this is computed for each of the 5 subsets in the training set by applying the following equation:

$$s_i = \frac{\prod_{j=1}^{5} s_{i,j}}{\sum_{i=1}^{n_f} \prod_{j=1}^{5} s_{i,j}} \tag{5.6}$$

where j represents the index of the subset in the training set, $s_{i,j}$ is the RF score for the i-th feature associated to the j-th subset and n_f is the number of features.

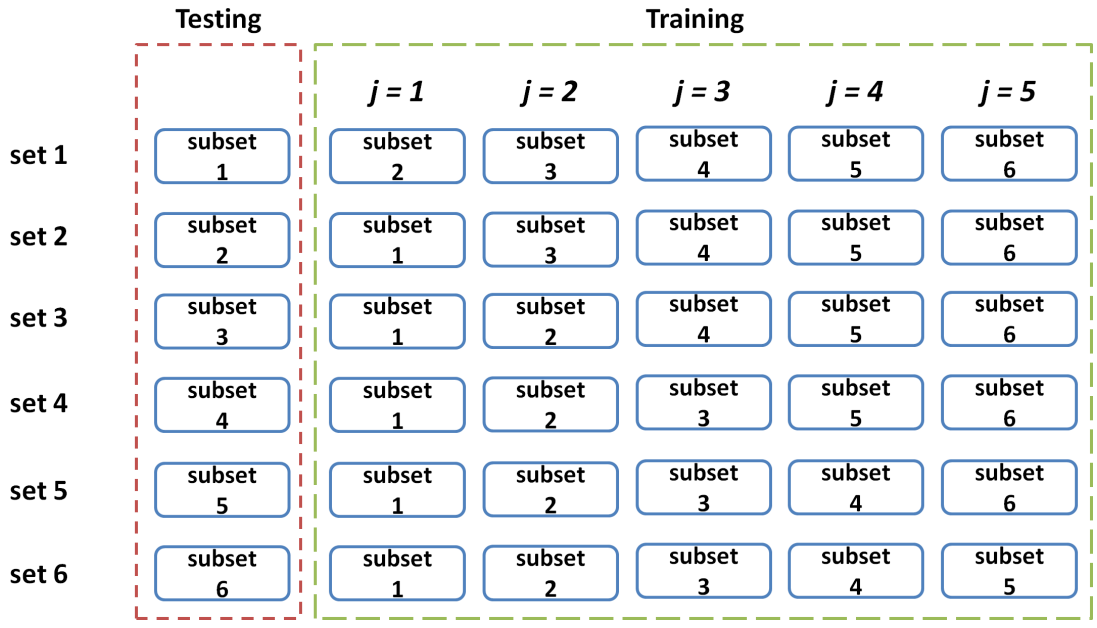

Figure 5.2: Illustration of the dataset distribution for 5-fold cross validation in the training set. The dataset is divided in 6 subsets, from which 5 subsets are in the training set and the remaining one is used for testing.

For our example presented in $\mathbf{A}$ ($n_f = 5$) we obtain $[s_1, s_2, s_3, s_4, s_5]$, where $s_4 > s_3 > s_1 > s_5 > s_2$. In this way, the features are ordered in decreasing magnitude of importance by creating a sorted set of features $[\mathbf{a_4}, \mathbf{a_3}, \mathbf{a_1}, \mathbf{a_5}, \mathbf{a_2}]$. By considering this order, each feature forms a new set together with the features that have higher importance:

- $A_1 = [\mathbf{a_4}]$
- $A_2 = [\mathbf{a_4}, \mathbf{a_3}]$
- $A_3 = [\mathbf{a_4}, \mathbf{a_3}, \mathbf{a_1}]$
- $A_4 = [\mathbf{a_4}, \mathbf{a_3}, \mathbf{a_1}, \mathbf{a_5}]$
- $A_5 = [\mathbf{a_4}, \mathbf{a_3}, \mathbf{a_1}, \mathbf{a_5}, \mathbf{a_2}]$

Each new presented set A_k is evaluated in the RF classifier by applying 5-fold cross validation to compute the average F1-score, $F1_k \in [0, 1]$. Then, the question is: *how many features should be selected?* The definition of the number of features k to be selected, implies the selection of the set A_k. For doing this task, we apply the following cumulative error function:

$$ce_k = \sum_{\alpha} \sqrt{\alpha \left(\frac{1-k}{n_f} \right)^2 + (1-\alpha)(1-F1_k)^2} \tag{5.7}$$

where $\alpha = \{0.05, 0.10, 0.15, 0.20, 0.25, 0.30, 0.35, 0.40, 0.45, 0.5\}$. The selected A_k is given by the set of k features with the minimum ce_k. This procedure is repeated 6 times by changing the subset in the testing set as we see in Figure 5.2. We group all the selected features generated in each experience, which forms the final selected feature set. For defining the number of PC for $\mathbf{PC_{HI}}$ and $\mathbf{PC_{Li}}$, we increment the number of PC by one and we test every new set by applying 5-fold cross validation for computing the average F1-score, $F1_k$. The number of PC will be given by the minimum ce_k. Since we repeat this procedure 6 times, we select the maximum number of PC among the 6 experiences performed.

The feature stacking from a different set to another is given by the inter-set feature importance. The feature set with the highest F1-score among $\mathbf{D_{HI}}$, $\mathbf{V}$ and $\mathbf{D_{Li}}$, is our reference set to which new features will be added to increase the overall F1-score. Let $\mathbf{A_3} = [\mathbf{a_4}, \mathbf{a_3}, \mathbf{a_1}]$ be our reference set with the highest F1-score, the feature set $\mathbf{B} = [\mathbf{b_1}, \mathbf{b_2}, \mathbf{b_3}, \mathbf{b_4}]$ contains the features to be added to the set $\mathbf{A_3}$. The estimation of the inter-set feature importance is achieved by stacking each feature:

- $[\mathbf{a_4}, \mathbf{a_3}, \mathbf{a_1}, \mathbf{b_1}]$
- $[\mathbf{a_4}, \mathbf{a_3}, \mathbf{a_1}, \mathbf{b_2}]$
- $[\mathbf{a_4}, \mathbf{a_3}, \mathbf{a_1}, \mathbf{b_3}]$
- $[\mathbf{a_4}, \mathbf{a_3}, \mathbf{a_1}, \mathbf{b_4}]$

We compute the RF score for each feature set associated to the added feature by using 5-fold cross validation as we explained before through equation 5.6. The features are ordered in decreasing magnitude of importance to be stacked sequentially in the reference set as follows:

- $B_1 = [\mathbf{a_4}, \mathbf{a_3}, \mathbf{a_1}, \mathbf{b_3}]$
- $B_2 = [\mathbf{a_4}, \mathbf{a_3}, \mathbf{a_1}, \mathbf{b_3}, \mathbf{b_4}]$
- $B_3 = [\mathbf{a_4}, \mathbf{a_3}, \mathbf{a_1}, \mathbf{b_3}, \mathbf{b_4}, \mathbf{b_1}]$
- $B_4 = [\mathbf{a_4}, \mathbf{a_3}, \mathbf{a_1}, \mathbf{b_3}, \mathbf{b_4}, \mathbf{b_1}, \mathbf{b_2}]$

The selected B_k is given by the set of k features with the minimum ce_k. This procedure is repeated 6 times as it is illustrated in Figure 5.2, and then we group all the selected features generated in each experience, which forms the final selected feature set.

Table 5.1: Abbreviation, full name and number of tree crowns per species in the study area. The total number of trees is 479

Abbr.	Genus species	English name	No.
ABAL	*Abies alba*	European silver fir	146
ACPS	*Acer pseudoplatanus*	Sycamore maple	7
BEPE	*Betula pendula*	Silver birch	8
BEsp	*Betula sp.*	Birch	2
COAV	*Corylus avellana*	Common hazel	3
FASY	*Fagus sylvatica*	European beech	68
FREX	*Fraxinus excelsior*	European ash	1
PIAB	*Picea abies*	Norway spruce	209
PICE	*Picea abies*	Norway spruce	1
PIUN	*Pinus uncinata*	Mountain pine	29
POTR	*Populus tremula*	European aspen	2
SOAR	*Sorbus aria*	Common whitebeam	1
SOAU	*Sorbus aucuparia*	Rowan	2

5.3.8 Classification

For the tree species classification, tree crowns were selected according to the number of pixels per crown. Thus, those trees that had more than 4 pixels per crown, were considered in our dataset. By applying this criterion, an average of 20.5 pixels per crown was obtained which is close to the average number of pixels per crown selected by Baldeck *et al.* [272] (24.9 pixels per crown). After performing the tree crown selection, the number of trees per specie were distributed according to Table 5.1.

For the RF classifier, the number of decision trees to grow was set to 1000. The training and test sets were defined by randomly separating trees and by associating the pixels with their crowns. The tree crowns were divided into six sets. The training set was formed by five of these six subsets, whose amount of pixels are similar number of samples selected in [127] (1537 pixels).

Our dataset showed a problem of class imbalance, which means the number of trees and pixels per class are not evenly distributed [268]. To address this problem, two strategies were implemented. First, those tree species that had less than six trees or had less than 1% of total number of pixels were grouped into a class called “other" species. Second, RF automatically weighted the classes by considering that these are inversely proportional to the frequency that the class has in the data [273]. The pixel distribution is described in Table 5.2.

5.4 Results and discussion

The ground truth of the seven plots of the Chamrousse site is illustrated over the images in Figure 5.3. Four classes of tree species were classified at pixel-level. The tree species PIAB is present in all forest plots, while the class PIUN is in plot 4 only.

The mask filtering stage from subsection 5.3.6 is illustrated in Figure 5.4 by presenting the

Table 5.2: Abbreviation, number and percentage of trees and pixels for four identified species and one "other" species class

Abbr.	Average pixels/tree	No. pixel	Pixel [%]	Tree [%]
ABAL	18.4	2764	28.2	30.5
FASY	23.4	1822	18.6	14.2
PIAB	20.0	4529	46.2	43.6
PIUN	8.2	266	2.7	6.1
Other	16.4	423	4.3	5.6
Overall	20.5	9804	100	100

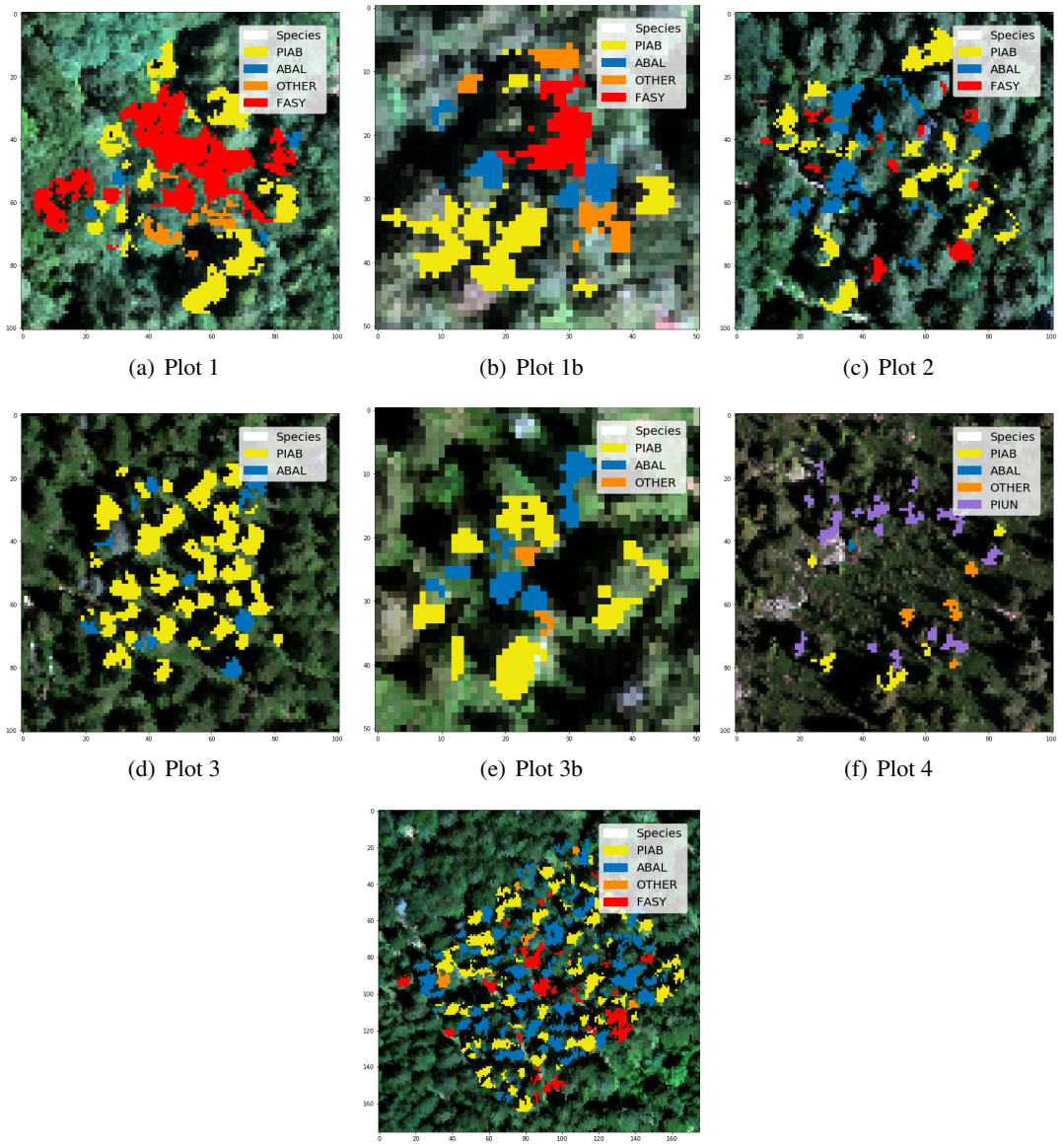

(a) Plot 1 (b) Plot 1b (c) Plot 2

(d) Plot 3 (e) Plot 3b (f) Plot 4

(g) Plot Premol

Figure 5.3: RGB representation of the forest plots corresponding to the Chamrousse site with the following color labels: ● Abies alba (ABAL), ● Fagus sylvatica (FASY), ● Picea abies (PIAB), ● Pinus uncinata (PIUN) and ● "other" species

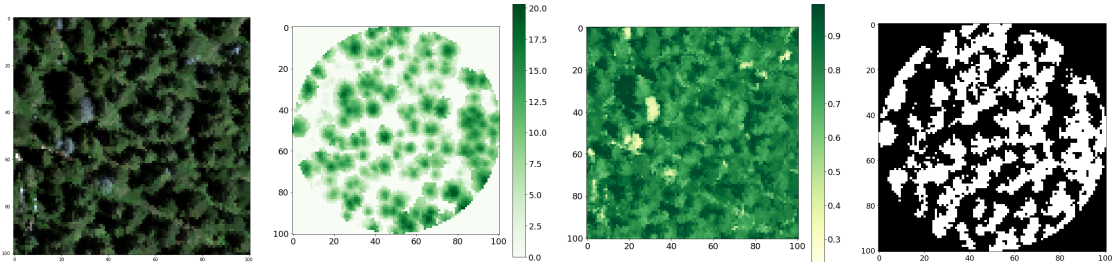

(a) RGB image (b) DSM (c) NDVI (d) Mask filter

Figure 5.4: Height, vegetation and shadow mask applied in plot 3.

Table 5.3: Overall accuracy [%] and F1-score [%] of forest tree species classification for HI and LiDAR features after before and after removing the shadow pixels.

	Ground truth		Mask filter	
Tree species	$\mathbf{D_{HI}}$	$\mathbf{D_{Li}}$	$\mathbf{D_{HI}}$	$\mathbf{D_{Li}}$
ABAL	54.7	60.5	**63.8**	**61.6**
FASY	61.6	44.2	**71.2**	**50.9**
PIAB	70.8	70.2	**77.3**	**71.5**
PIUN	28.8	62.1	**40.2**	**66.1**
Other	17.7	4.2	**27.9**	**22.1**
Overall accuracy	62.4	61.7	**70.6**	**63.9**

RGB representation, the DSM from LiDAR and the NDVI. The effect of this filter was evaluated at pixel-level in the classifier by considering the spectral information and the LiDAR features. The overall accuracy is computed by taking into account all the six experiments presented in Figure 5.2, as it is detailed in Table 5.3. We confirm the findings of Torabzadeh *et al.* [86], who removed the shadow pixels for forest tree species classification. In fact, the overall accuracy for HI increased around 8 points of percentage at the same time that all species improved their F1-scores. The effect of removing pixels associated with shadow, low objects and non-vegetation are appreciated in Figure 5.5. One of the main results is the reduction of the spectral variability generated mainly by shadow pixels, which are generated by the topography of the site, the forest structure and the illumination conditions. The shadow pixels distort the spectral content and limit the classification task. Another remark regarding the application of this mask is in the group of other species. Before the filtering task, this class contains pixels from broadleaves and conifers (*Picea cembra*). After filtering the data, this group contains broadleaves species only. Although the improvement of mask filtering is 2.2 points of percentage for the LiDAR features, the effect is not visually perceived in Figure 5.4 as we notice for HI data. However, the class other species showed the most significant F1-score increase from 4.2 to 22.1%.

One of the feature sets that contributes significantly for the tree species classification is the computation of PC. In Table 5.4, we compare the effect of obtaining the PC from PCA and rPCA. For HI, the overall accuracy showed an improvement with respect to the result obtained by classifying just spectral bands (70.6%). The components of rPCA performed better than PCA by presenting a slightly increase of 1.3 points of percentage between them. The most relevant effect is given by the class PIUN by providing a F1-score increase from 74.2% to 82.9%. It might be explained due to fact the algorithm rPCA was applied over each forest plot image and the class PIUN can be found in the plot 4 only. All the classes showed a F1-score improvement with the exception

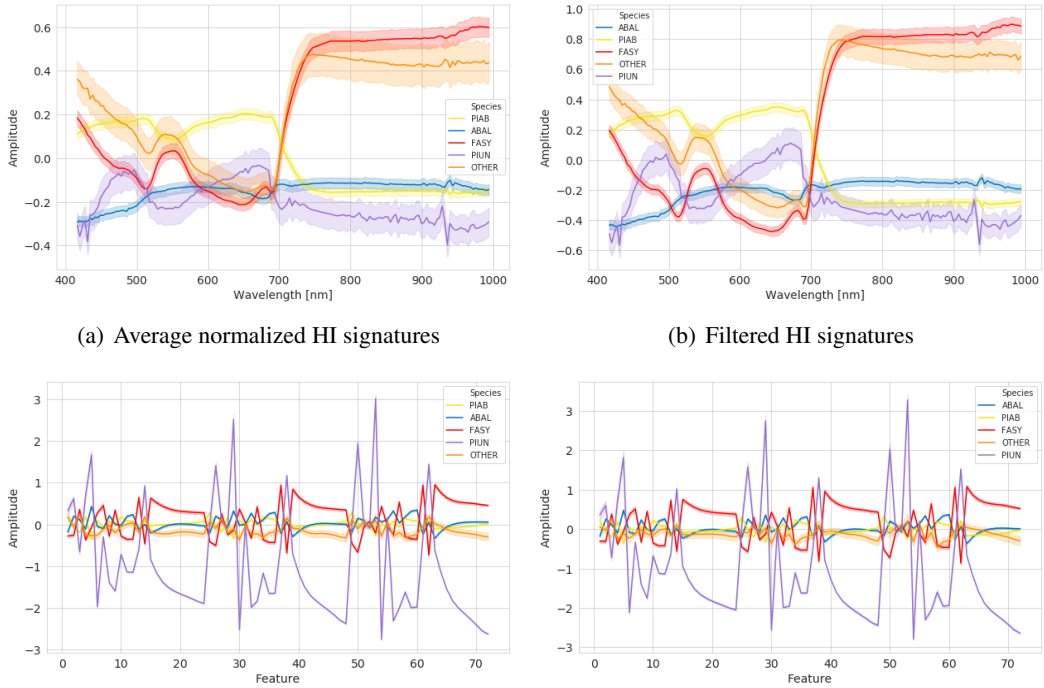

(a) Average normalized HI signatures

(b) Filtered HI signatures

(c) Average normalized LiDAR features

(d) Filtered LiDAR signatures

Figure 5.5: Normalized average spectral and LiDAR features of all selected pixels from Figure 5.3 for describing forest tree species with the following color labels: ● Abies alba (ABAL), ● Fagus sylvatica (FASY), ● Picea abies (PIAB), ● Pinus uncinata (PIUN) and ● "other" species

of class FASY which performed better with PCA (75.1%). For the LiDAR features, PCA provided better results than rPCA, but the difference is less than one point of percentage. Both techniques presented an overall accuracy better than the classification by LiDAR features. The class PIUN benefited more from rPCA, while the class ABAL performed a better classification with LiDAR features.

One of the data fusion approaches at feature-level is feature stacking [227]. Table 5.5 presents the overall accuracy and the F1-scores by feature set and by forest trees species. The last column presents the results of stacking all feature sets: 160 hyperspectral bands $\mathbf{D_{HI}}$, 61 vegetation indices in $\mathbf{V}$, 160 PC obtained by using rPCA from HI in $\mathbf{PC_{HI}}$, 72 LiDAR features in $\mathbf{D_{Li}}$ and 72 PC obtained by using rPCA from LiDAR in $\mathbf{PC_{Li}}$. We noticed the VI provided an overall accuracy increase of 2.2 points of percentage with respect to spectral bands. In fact, all forest tree species improved the classification performance, in particular the class PIAB with a F1-score of 79%. The full feature stacking improved the overall accuracy considering an increase of F1-score for all tree species than individual feature set contribution, with the exception of class PIUN that performed better with PC.

From the previous results, feature stacking improved the overall accuracy by considering 525 features. We explore if the reduction of the amount of features can maintain or improve the classification performance. We tested another scheme of data fusion at feature-level based on the selection of individual features from each feature set, and then we proceeded to stack the final subsets. To do this task, we implemented the intra-set feature importance based RF score and 5-fold cross validation in the training set, as it was explained in subsection 5.3.7. Table 5.6 presents the overall accuracy and F1-scores of each feature set by species. We noticed that feature reduction improved the classification performance of each feature set with the exception of spectral features. The performance decreased less than one point of percentage for HI because the classes ABAL, PIAB and other species decreased their results too. Regarding the stacking of

Table 5.4: Overall accuracy [%] and F1-score [%] of forest tree species classification for HI and LiDAR features by using PCA and rPCA.

	PCA		rPCA	
Tree species	$\mathbf{PC_{HI}}$	$\mathbf{PC_{Li}}$	$\mathbf{PC_{HI}}$	$\mathbf{PC_{Li}}$
ABAL	61.6	**58**	**66.3**	55.5
FASY	**75.1**	**53.3**	72.1	52.6
PIAB	77.6	**73**	**78.5**	72.4
PIUN	74.2	74.9	**82.9**	**77.8**
Other	15.3	11.4	**29.5**	**17.1**
Overall accuracy	71.9	**65.2**	**73.2**	64.5

Table 5.5: Overall accuracy [%], F1-score [%] of forest tree species classification and the number of features (No.) for each feature set. The last column presents the results of stacking all features.

Feature	$\mathbf{D_{HI}}$	**V**	$\mathbf{PC_{HI}}$	$\mathbf{D_{Li}}$	$\mathbf{PC_{Li}}$	Stacking
No.	160	61	160	72	72	525
ABAL	63.8	67.8	66.3	61.6	55.5	**73.4**
FASY	71.2	72.5	72.1	50.9	52.6	**72.9**
PIAB	77.3	79	78.5	71.5	72.4	**80.9**
PIUN	40.2	56.1	**82.9**	66.1	77.8	80.6
Other	27.9	33.5	29.5	22.1	17.1	**34.8**
Overall accuracy	70.6	72.8	73.2	63.9	64.5	**76.1**

the selected features, the classes ABAL and PIAB benefited more of this operation with respect to the other classes that obtained better results by reducing the amount of PC from the hyperspectral data. An important finding of this operation is the creation of a list of the 25 VI that improved the classification among the 6 experiments performed. The list of VI and frequency is presented in Figure 5.6. The description and computation of these VI are presented in Annex B. Figure 5.7 shows the selected feature representation by forest tree species.

A final scheme of fusion was considering the inter-set feature importance presented in subsection 5.3.7 among the feature sets $\mathbf{D_{HI}}$, **V** and $\mathbf{D_{Li}}$. The feature set **V** was considered as reference set because of its highest accuracy. We started by adding the features from HI. The effect of adding the selected features did not increase the overall accuracy. We obtained 73.5% and the selected VI produced an overall accuracy of 73.6%. Then, we proceeded to add the LiDAR features. This operation reduced the overall accuracy. We maintained the number of PC in HI and LiDAR, and we performed the feature stacking among 25 features in **V**, 20 components in $\mathbf{PC_{HI}}$ and 22 components from $\mathbf{PC_{Li}}$ as it is presented in Table 5.7. The overall accuracy of stacking these three feature sets is slightly better than the previous approach that considers HI and LiDAR features. The main difference is the reduction of features to obtain 67 features. Most of the species improved their F1-scores with the exception of other species, but this result is better than the approach of stacking all selected features presented in Table 5.6.

Tables 5.8 and 5.9 present the species classification at the pixel-level and tree-level, respectively. The overall accuracy at tree-level is 78.3%, which is slightly similar to the accuracy at pixel-level, 78.1%. The species PIUN, the class in plot 4, obtained the highest producer's and

Table 5.6: Overall accuracy [%], F1-score [%] of forest tree species classification and the number of selected features (No.) for each feature set. The last column presents the results of stacking all features.

Feature	$\mathbf{D_{HI}}$	**V**	$\mathbf{PC_{HI}}$	$\mathbf{D_{Li}}$	$\mathbf{PC_{Li}}$	Stacking
No.	38	25	20	20	22	125
ABAL	62.4	69.6	70.8	61.6	60.8	**75**
FASY	71.8	73	**74.9**	51.1	54.5	73.3
PIAB	76.3	79.3	80.7	72.5	73	**81.3**
PIUN	49.4	62.7	**86.6**	67.8	76.8	80.7
Other	26	31.9	**46.5**	25.6	19.9	37.4
Overall accuracy	69.8	73.6	76.1	64.4	65.7	**76.8**

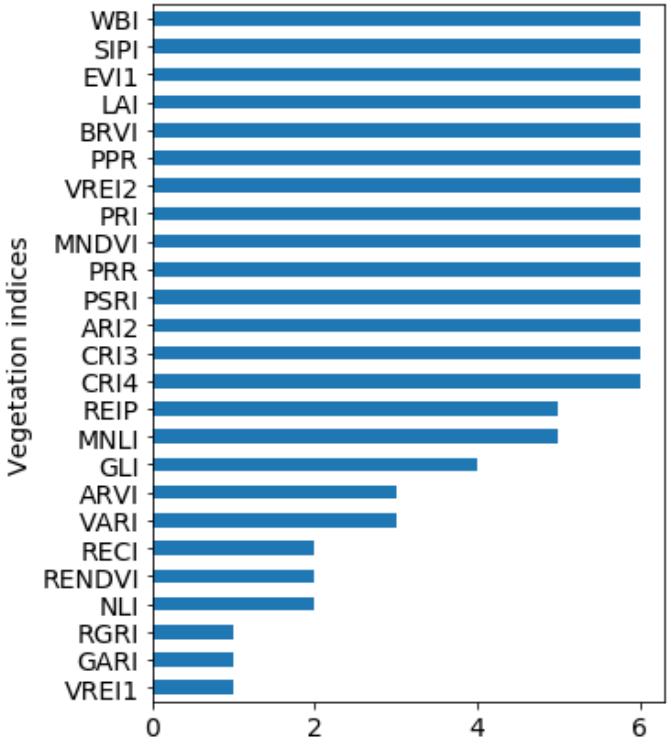

Figure 5.6: Frequency of selected vegetation indices after performing feature reduction according to the subset distribution presented in Figure 5.2.

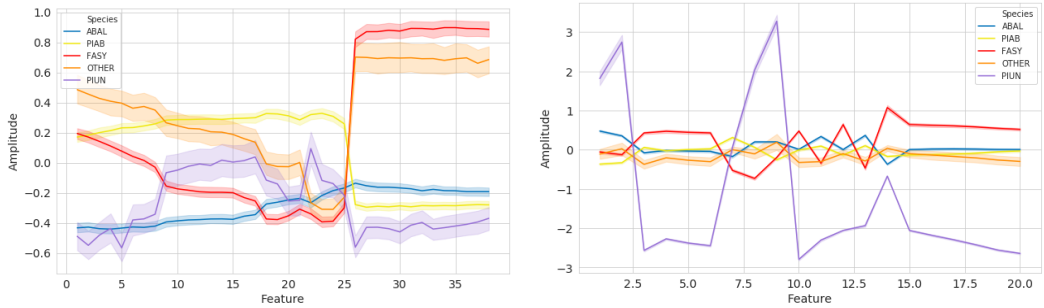

(a) Selected HI bands

(b) Selected LiDAR features

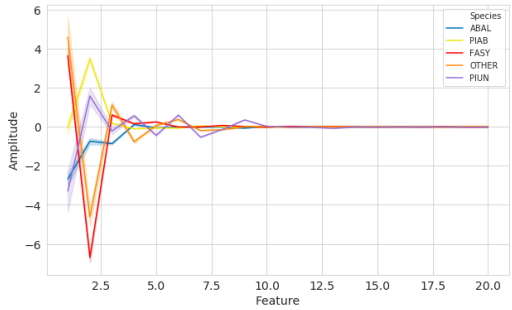

(c) Selected HI PC

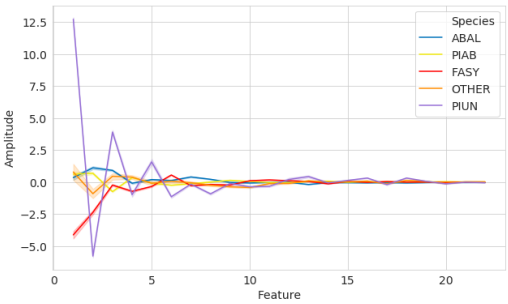

(d) Selected LiDAR PC

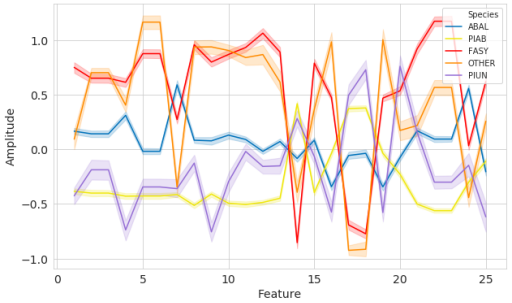

(e) Selected VI

Figure 5.7: Normalized average selected features from HI and LiDAR data, the selected amount of PC and the selected VI for describing forest tree species with the following color labels: ● Abies alba (ABAL), ● Fagus sylvatica (FASY), ● Picea abies (PIAB), ● Pinus uncinata (PIUN) and ● "other" species

Table 5.7: Overall accuracy [%], F1-score [%] of forest tree species classification and the number of selected features (No.) after stacking each feature set.

Feature	**V**	**V + PC_{HI}**	**V + PC_{HI} + PC_{Li}**
No.	25	45	67
ABAL	69.6	72.8	**74.5**
FASY	73	75.3	**76.4**
PIAB	79.3	81.2	**82.2**
PIUN	62.7	84.8	**90.3**
Other	31.9	**44.8**	43.5
Overall accuracy	73.6	76.7	**78.1**

user's accuracy among all species. This class benefited from the data fusion with the PC from HI and LiDAR features. Figure 5.8 presents the pixel classification of 15 tree crowns. At tree-level, the classifier predicted just one PIUN tree as PIAB as we observed in Figure 5.8(b) because of one pixel difference. PIUN, PIAB and ABAL belongs to the group of conifers, so it is expected to have wrong prediction among them. The species PIAB is the most abundant class of our dataset. It obtained a producer's accuracy of 90.6%, but the misclassied pixels from ABAL, FASY and other species reduce the user's accuracy as we observed in Figures 5.8(e) and 5.8(f). Although the producer's accuracies of ABAL and FASY species are almost similar at tree-level, we noticed that the most amount of wrong predictions results as PIAB class (Figures 5.8(h) and 5.8(k)) and between them (Figures 5.8(i) and 5.8(l)). The class other species is the most challenging to classify because it is diffused into the other species as we observe in Figures s 5.8(b) and 5.8(c). The classification at tree-level is obtained by applying a majority voting rule to define the species for each crown [127]. In this approach, authors used rPCA and SVM to obtain an overall accuracy for the classification of six tree species of 91.7% and 61.1% at the pixel- and tree-level, respectively. Our results shows more consistency between the pixel- and tree-level by evaluating the entire dataset.

Table 5.8: Species classification results at pixel-level obtained by the fusion of HI and LiDAR features

Ground truth							
Tree species	ABAL	FASY	PIAB	PIUN	Other	Total	Producer's acc. [%]
ABAL	1912	119	725	1	7	2764	69.2
FASY	113	1387	302	0	20	1822	76.1
PIAB	310	184	3974	13	48	4529	87.7
PIUN	3	0	17	241	5	266	90.6
Other	32	117	121	13	140	423	33.1
Total	2370	1807	5139	268	220	9804	
User's acc. [%]	80.7	76.8	77.3	89.9	63.6		78.1

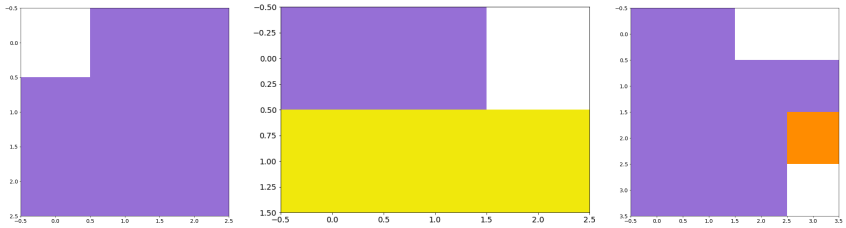

(a) PIUN (b) PIUN (c) PIUN

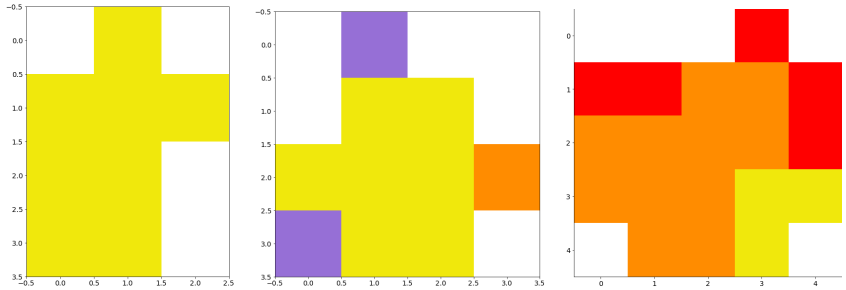

(d) PIAB (e) PIAB (f) PIAB

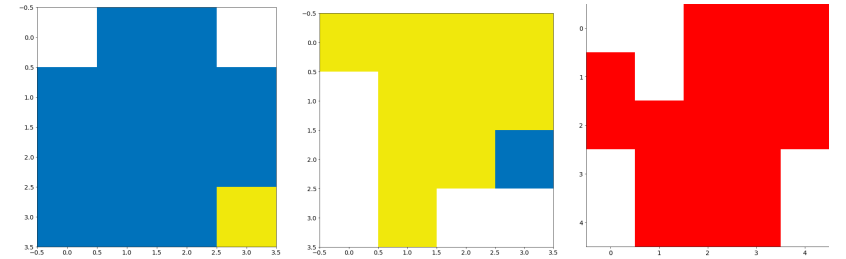

(g) ABAL (h) ABAL (i) ABAL

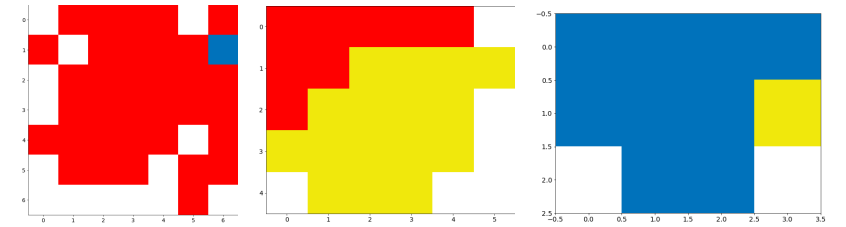

(j) FASY (k) FASY (l) FASY

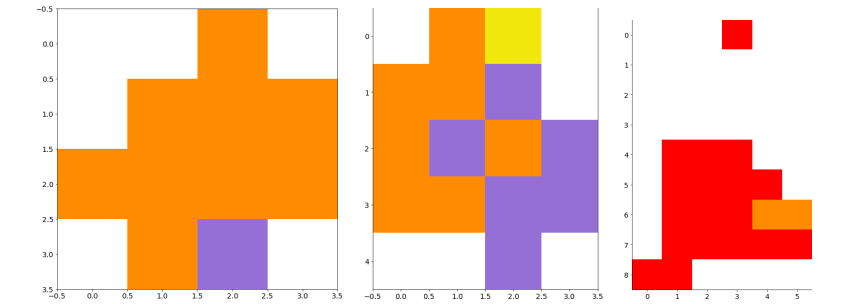

(m) Other (n) Other (o) Other

Figure 5.8: Results of pixel classification for tree-level assessment of 15 *tree crowns: (a) PIUN correctly detected, (b) PIUN detected as PIAB, (c) PIUN correctly detected, (d) PIAB correctly detected, (e) PIAB correctly detected, (f) PIAB detected as other, (g) ABAL correctly detected, (h) ABAL detected as PIAB, (i) ABAL detected as FASY, (j) FASY correctly detected, (k) FASY detected as PIAB, (l) FASY detected as ABAL, (m) Other correctly detected, (n) Other correctly detected, (o) Other detected as FASY. Legend: ● Abies alba (ABAL), ● Fagus sylvatica (FASY), ● Picea abies (PIAB), ● Pinus uncinata (PIUN) and ● other species*

Table 5.9: Species classification results at tree-level obtained by the fusion of HI and LiDAR features

Ground truth							
Tree species	ABAL	FASY	PIAB	PIUN	Other	Total	Producer's acc. [%]
ABAL	100	5	41	0	0	146	68.5
FASY	5	47	15	0	1	68	69.1
PIAB	9	9	190	0	1	209	90.9
PIUN	0	0	1	28	0	29	96.6
Other	2	8	7	0	10	27	37.0
Total	116	69	254	28	12	479	
User's acc. [%]	86.2	68.1	74.8	100	83.3		78.3

5.5 Conclusions

In this work, we presented a data fusion scheme that integrated features extracted from the HI and the LiDAR data for semantic segmentation. The potential of rPCA for extracting features from LiDAR and HI improved the classification together with the vegetation indices. The feature selection implements two steps: first, the intra-set feature importance was described by the RF scores and 5-fold cross validation in the training set. The cumulative error function helps to define the number of features to be accepted in the model. The inter-set feature importance was estimated for selecting feature sets that can contribute to improve the classification. This method offers the flexibility of incorporating additional features, which increases the interpretability of the model. The feature reduction process decreased the dimensionality from 525 to 67 features. The overall accuracy of tree species classification at pixel-level was 78.1%. Our approach showed that 78.3% of trees were correctly assigned overall, which represented an improvement of 17.2 points of percentage with respect to [127]. Although these two remote sensing modalities provided valuable information, the coniferous classes PIUN and PIAB benefited mainly from feature selection and integration. However, it became a challenging task for dealing with imbalanced classes of our dataset, such as other species. Future work is going to be focused in the implementation of tree species detectors by selecting the most relevant features from HI and LiDAR data for each specific tree species.

6

Conclusion and work perspectives

In this final chapter, we summarize the main contributions presented along this manuscript and we propose some perspectives in which we can address our future work.

Sommaire

This PhD thesis deals with the integration of LiDAR and hyperspectral data to characterize individual forest trees. The leading idea is to improve methods to derive forest information at tree-level by extracting geometric and radiometric features. This research work considers the issues of field data required to build and validate the models. Forest plots represent a wide range of forest structures, from conifers to mixed, multilayered stands. Tree measurements from 894 tree crowns grouped in 7 plots in mountain forests located in the French Alps are considered along this study. Besides, a dataset of 573 tree crowns from 15 plots located in the Italian Alps was also taken into account. For our tree measurements, the accuracy of LiDAR data was employed to co-register field data. The hyperspectral data were orthorectified by using a DSM, which provided a relative geometric precision of 2-3 pixels. A more detailed information regarding the field data is provided in chapter 3.

The contributions of this manuscript may be of great interest for forest managers in order to account (i) for the inventory of individual tree crowns (ii) for mapping individual tree species, and these can be summarized as follows:

- An updated review of data fusion methods of LiDAR and hyperspectral data for forest monitoring.
- An improved 3D segmentation algorithm for delineating individual tree crowns based on Adaptive Mean Shift (AMS3D) and an ellipsoid crown shape model.
- A criterion for feature selection based on random forests (RF) score, 5-fold cross validation and a cumulative error function for forest tree species classification.

6.1 How data processing methods are applied in each level of data fusion for forest monitoring?

The continuing advancement of remote-sensing technology has encouraged the use of data available to the scientific community. The integration of remote sensing data has attracted significant attention, specially for applications in forest monitoring. Therefore, an exploratory task is always welcomed to identify the methods and how these can be adapted for this subject in order to be transferred towards an operative context. From the theoretical point of view, this manuscript provides a review of data processing methods at each level of fusion in chapter 2. Three levels of fusion for processing data were identified: observation or low-level, feature or medium-level, and decision or high-level.

We grouped the methods in processes in order to illustrate the interaction among them, and the link between data and the spatial domain (point cloud or image grid). An extensive compilation of feature descriptors are categorized in six groups: statistical, structural, topographic, vegetation indices, textural and dimension reduction. For the feature sets used in this manuscript, we provided the equations in annex B. At decision-level, we established the processes that define the main forest applications: species mapping, the estimation of functional, physiological, structural attributes, above-ground biomass and carbon density, and land cover maps. From this review, we highlight that the automatic delineation of individual trees is required for the characterization at tree-level. Then, considering the high resolution of the LiDAR data in our datasets, a 3D segmentation algorithm is proposed for detecting individual tree crowns.

Additional aspects that can improve this review of data fusion methods can be focused on the response of the revised methods with respect to specific characteristics of the remote sensing data such as the spatial or spectral resolution, or the information regarding the type of forest (temperate,

boreal, tropical, subtropical) or specie composition. For instance, some individual tree crown segmentation algorithms provide better results in the context of a dense point cloud and sparse canopies. Although this type of review can generate anticipated value judgments, these aspects can be helpful to understand the conditions in which the method would perform in a specific scenario. At this point, the collaboration and networking of the scientific community can also give an updated feedback through data science challenges.

6.2 How a crown shape model can improve the segmentation of individual tree crowns?

Individual tree-level analysis is oriented to extract information regarding the position and size of the trees. Mountainous forest is a challenging environment because of the horizontal and vertical structure of plots, which makes the parameter setting of the detection algorithms, a difficult task. In this manuscript, we improved the 3D segmentation algorithm proposed by Ferraz *et al*. [96,97] by preserving the input parameters based on allometry equations and by introducing an ellipsoid crown shape model, as it is explained in chapter 4. The parameters of AMS3D does not depend on the number and position of treetops, which makes it a good alternative. We tested two crown shape models for adapting the size of the superellipsoid (SE) kernel profile. These schemes are compared with two other MS algorithms with and without kernel profile size adaptation. We select the best algorithm output per plot based on the maximum F1-score. The ellipsoid crown shape model with a SE kernel profile of $n = 1.5$ presents the best overall recall of 59.0% and Jaccard index of 53.7% among the assessed schemes of 3D segmentation.

Our approach solved the problem of the AMS3D proposed by Ferraz *et al*. [97], which produced undersegmented tree crowns because the kernel radius enclosed more than one tree at upper layers. The ellipsoid crown shape model adjusts the crown radius to control the kernel size and improved the segmentation results. The 3D mean shift algorithm proposed by Xiao *et al*. [163] maximized the F1-score by decreasing the number of detections, which produced the best precision with respect to other algorithms, but it decreased the number of true positive trees. Xiao's algorithm produced better recall values with small kernels by oversegmenting the point cloud. The results obtained show that models are highly dependent on the forest structures, which can be described by the gap area percentage at different heights of the canopy.

The limitation of the proposed 3D segmentation algorithm is the parameter setting, which depends on the ground truth information. In the short-term, we prepare a 2D segmentation approach based on mean shift for parameter estimation of the AMS3D. The idea is reducing the number of parameters to one by introducing the vertical kernel weight function proposed by Xiao *et al*. [163]. The remaining parameter can be calibrated by applying sensitivity analysis, and by using the silhouette coefficient to select the best output segmentation. Hyperspectral data can be integrated in this approach through an additional kernel. Lee *et al*. [156] introduces the second to fifth principal components from hyperspectral data into a 3D graph-cut segmentation approach for estimating point similarity. The first component is associated to illumination information, so it is affected by shadow. Similarly, the kernel design can be explored by adding other descriptors (e.g. percentiles). Finally, the results obtained with the ellipsoid crown shape model open a new experimental area to find alternative shapes that fits the tree crown according to the type of forest.

6.3 Which feature combination contribute to characterize the forest tree species composition?

In the line of individual tree characterization, the identification of forest tree species is of our concern in the chapter 5 of this manuscript. A pixel-classification workflow was developed for the identification of four main species: *Abies alba* (ABAL), *Fagus sylvatica* (FASY), *Picea abies* (PIAB), *Pinus uncinata* (PIUN) and “other" species. Our dataset for training and testing was created from the field data which have been preprocessed by using mask filtering based on height, vegetation and shadow. The effect of removing shadow pixels benefited the identification of species by reducing the spectral variability. Five set of features were studied in this approach: 160 hyperspectral bands (HI), 61 vegetation indices (VI), the principal components (PC) obtained by using robust PCA (rPCA) from HI, 72 LiDAR features and the PC obtained by using rPCA from LiDAR. We performed a fusion at feature level by selecting the amount of features of our prediction model. This operation was based on the random forests (RF) score, 5-fold cross validation in the training set and a cumulative error function for defining a criterion of intra-set feature importance.

An important contribution is the reduction of the amount of features by preserving, or even enhancing the performance of the classification. The inter-set feature importance was applied for merging features among the 38 HI, 25 VI and 20 LiDAR features. The classification results showed the selected vegetation indices combined with the spectral bands and LiDAR features did not improve significantly the classification. The best feature set combination was given by the selected 25 VI, 20 PC from HI and 22 PC from LiDAR features. The overall accuracy of tree species classification at pixel-level was 78.1%. Our approach showed that 78.3% of trees were correctly assigned overall, by using 67 out of 525 feature descriptors.

Although the algorithm has been validated through the ground truth derived from tree measurements, the matched trees extracted from the AMS3D segmentation algorithm can be also considered for training and testing our classification algorithm, and also to complement the information of individual tree characterization. In this way, we can propose a workflow in which we can test different datasets and assess its scope for other forest applications.

The shadow effect influences the variability of the spectral signatures of forest tree species. In our approach, this issue is solved by removing these pixels with mask filter. Another technique that can be applied to deal with shadows is the unmixing-based approach as it is suggested by Matsuki *et al.* [135], who applied it in a complex mixed forest. Spectral unmixing has been used in other studies to identify group of species: conifers and broadleaves [274]. This technique results promising because new unmixing-based approaches are oriented to integrate HI and LiDAR data [275].

Regarding the type of features used in this approach, the performance of VI provided interesting results. Unlike PCA that is a linear method for extracting features, VI establishes non-linear relationships among the spectral bands. For this reason, it is important to explore the response of non-linear algorithms for extracting features. For instance, KPCA [230] or autoencoders [166] have been also considered for the identification of forest tree species.

The criterion for selecting the number of features based on the RF-score and the cumulative error function was performed in a 5-fold cross validation in the training set. This strategy determined the number of features that contributed most in the classification task. In this way, the number of VI was determined and the frequency of the selected feature is shown in Figure 5.6. We consider as a future work, that the number of experiments to select features should be increased in order to confirm this trend. In addition to that, these results have been compared with single feature stacking. Since the number of selected features can be determined, we can also explore other feature selection algorithms such as Forward Feature Selection (FFS) [123, 137], or Sequential Forward Floating Selection (SFFS) [121, 122, 159].

In the long term, we can think over the integration with other data modalities, either to improve the task of individual tree delineation or to increase the feature representation for the specie classification. The IDTResS competition provided field data of forest plots for three remote sensing modalities: RGB images, DSM and LiDAR point cloud, and hyperspectral images. The spatial resolution of the LiDAR point cloud is 6 points m^{-2}, while the hyperspectral grid is 1 m^2. RGB images have the highest spatial resolution of 0.01 m^2. Our AMS3D approach relies on a dense point cloud for delineating tree crowns, so this scenario is an example of how data fusion strategies can be elaborated in order to improve the performance of current methods.

Bibliography

[1] *Global Forest Resources Assessment 2020*. FAO, 2020.

[2] R. J. Keenan, G. A. Reams, F. Achard, J. V. de Freitas, A. Grainger, and E. Lindquist, "Dynamics of global forest area: Results from the fao global forest resources assessment 2015," *Forest Ecology and Management*, vol. 352, pp. 9 – 20, 2015. Changes in Global Forest Resources from 1990 to 2015.

[3] *The State of the World's Forests 2020*. FAO and UNEP, 2020.

[4] W. E. Stein, C. M. Berry, J. L. Morris, L. V. Hernick, F. Mannolini, C. Ver Straeten, E. Landing, J. E. Marshall, C. H. Wellman, D. J. Beerling, and J. R. Leake, "Mid-devonian archaeopteris roots signal revolutionary change in earliest fossil forests," *Current Biology*, vol. 30, no. 3, pp. 421 – 431.e2, 2020.

[5] W. Stein, C. Berry, L. Hernick, and F. Mannolini, "Surprisingly complex community discovered in the mid-devonian fossil forest at gilboa," *Nature*, vol. 483, pp. 78–81, 03 2012.

[6] C. M. Berry, "Palaeobotany: The rise of the earth's early forests," *Current Biology*, vol. 29, no. 16, pp. R792 – R794, 2019.

[7] B. Meyer-Berthaud and A.-L. Decombeix, "In the shade of the oldest forest," *Nature*, vol. 483, no. 7387, pp. 41–42, 2012.

[8] Łukasz Pawlik and Brian Buma and Pavel Šamonil and Jiří Kvaček and Anna Gałązka and Petr Kohout and Ireneusz Malik, "Impact of trees and forests on the devonian landscape and weathering processes with implications to the global earth's system properties - a critical review," *Earth-Science Reviews*, vol. 205, p. 103200, 2020.

[9] G. Grassi, J. House, F. Dentener, S. Federici, M. Elzen, and J. Penman, "The key role of forests in meeting climate targets requires science for credible mitigation," vol. 7, pp. 220–226, 02 2017.

[10] M. J. Sanz, "Un-redd, the united nations programme to reduce emissions from deforestation and forest degradation (2008-2015)," *Unasylva*, vol. 67, no. 246, pp. 31–36, 2016. Copyright - Copyright Food and Agriculture Organization of the United Nations 2016; Document feature - ; Photographs; Diagrams; Tables; Last updated - 2017-04-01.

[11] V. Viippola, T. H. Whitlow, W. Zhao, V. Yli-Pelkonen, J. Mikola, R. Pouyat, and H. Setälä, "The effects of trees on air pollutant levels in peri-urban near-road environments," *Urban Forestry & Urban Greening*, 2018.

[12] P. Iversen, "Forests' role in the climate change agenda," *Unasylva*, vol. 67, no. 246, p. 3, 2016.

[13] C. Watkins, *Trees, woods and forests: A social and cultural history*. Reaktion Books, 2014.

[14] V. L. Caetano Andrade, B. M. Flores, C. Levis, C. R. Clement, P. Roberts, and J. Schöngart, "Growth rings of brazil nut trees (bertholletia excelsa) as a living record of historical human disturbance in central amazonia," *PLOS ONE*, vol. 14, pp. 1–18, 04 2019.

[15] V. L. Caetano-Andrade, C. R. Clement, D. Weigel, S. Trumbore, N. Boivin, J. Schöngart, and P. Roberts, "Tropical trees as time capsules of anthropogenic activity," *Trends in Plant Science*, vol. 25, no. 4, pp. 369 – 380, 2020.

[16] R. O. Curtis, *Silvicultural research and the evolution of forest practices in the Douglas-fir region*, vol. 696. US Department of Agriculture, Forest Service, Pacific Northwest Research Station, 2007.

[17] J. Boyle, J. Tappeiner, R. Waring, and C. Tattersall Smith, "Sustainable forestry: Ecology and silviculture for resilient forests," in *Reference Module in Earth Systems and Environmental Sciences*, Elsevier, 2016.

[18] D. Gilmour, "Silviculture and community forestry: looking backwards, looking forwards," *Banko Janakari*, pp. 6–14, 2018.

[19] IGN Institut National de l'Information Géographique et Forestière, "Le mémento - inventaire forestier." https://inventaire-forestier.ign.fr/spip.php?rubrique219, 2019. (Accessed on 08/18/2020).

[20] IGN Institut National de l'Information Géographique et Forestière, "Forêt de montagne." https://inventaire-forestier.ign.fr/IMG/pdf/France_part4-2.pdf, 2012. (Accessed on 10/05/2020).

[21] J.-M. Monnet, P. Paccard, and C. Riond, "La télédétection aéroportée pour la gestion des territoires forestiers de montagne," *Sciences Eaux & Territoires*, no. 33, pp. 64–69, 2020.

[22] M. Fuhr, T. Cordonnier, B. Courbaud, G. Kunstler, E. Mermin, C. Riond, and P. Tardif, "Long-term tree inventory data from mountain forest plots in france," *Ecology*, vol. 98, no. 4, pp. 1180–1180, 2017.

[23] O. Thees, M. Erni, R. Lemm, G. Stadelmann, and E. K. Zenner, "Future potentials of sustainable wood fuel from forests in switzerland," *Biomass and Bioenergy*, vol. 141, p. 105647, 2020.

[24] C. Pascual and A. García-Abril and L.G. García-Montero and S. Martín-Fernández and W.B. Cohen, "Object-based semi-automatic approach for forest structure characterization using lidar data in heterogeneous pinus sylvestris stands," *Forest Ecology and Management*, vol. 255, no. 11, pp. 3677 – 3685, 2008.

[25] H. E. Burkhart and M. Tomé, *Modeling Wood Characteristics*, pp. 405–427. Dordrecht: Springer Netherlands, 2012.

[26] M. van Leeuwen, T. Hilker, N. C. Coops, G. Frazer, M. A. Wulder, G. J. Newnham, and D. S. Culvenor, "Assessment of standing wood and fiber quality using ground and airborne laser scanning: A review," *Forest Ecology and Management*, vol. 261, no. 9, pp. 1467 – 1478, 2011.

[27] M. P. Fernández, A. Norero, J. R. Vera, and E. Pérez, "A functional-structural model for radiata pine (pinus radiata) focusing on tree architecture and wood quality," *Annals of Botany*, vol. 108, pp. 1155–1178, October 2011.

[28] B. Bennett, "What is a forest? on the vagueness of certain geographic concepts," *Topoi*, vol. 20, no. 2, pp. 189–201, 2001.

[29] T. Gschwantner, K. Schadauer, C. Vidal, A. Lanz, E. Tomppo, L. Di Cosmo, N. Robert, D. E. Duursma, and M. Lawrence, "Common tree definitions for national forest inventories in europe," *Silva Fennica*, vol. 43, no. 2, pp. 303–321, 2009. Cited By :42.

[30] P. W. West, *Tree and Forest Measurement*. Springer Berlin Heidelberg, 2009.

[31] Terje Gobakken and Erik Næsset and Ross Nelson and Ole Martin Bollandsås and Timothy G. Gregoire and Göran Ståhl and Sören Holm and Hans Ole Ørka and Rasmus Astrup, "Estimating biomass in hedmark county, norway using national forest inventory field plots and airborne laser scanning," *Remote Sensing of Environment*, vol. 123, pp. 443 – 456, 2012.

[32] E. Tomppo, M. Haakana, M. Katila, and J. Peräsaari, *Multi-source national forest inventory: Methods and applications*, vol. 18. Springer Science & Business Media, 2008.

[33] A. Kangas and M. Maltamo, *Forest inventory: methodology and applications*, vol. 10. Springer Science & Business Media, 2006.

[34] W. A. Bechtold and C. T. Scott, "The forest inventory and analysis plot design," *The enhanced forest inventory and analysis program—national sampling design and estimation procedures*, pp. 27–42, 2005.

[35] W. Wan Mohd Jaafar, I. Woodhouse, C. Silva, H. Omar, K. Abdul Maulud, A. Hudak, C. Klauberg, A. Cardil, and M. Mohan, "Improving individual tree crown delineation and attributes estimation of tropical forests using airborne lidar data," *Forests*, vol. 9, p. 759, Dec 2018.

[36] J.-F. Côté, R. A. Fournier, and R. Egli, "An architectural model of trees to estimate forest structural attributes using terrestrial lidar," *Environmental Modelling & Software*, vol. 26, no. 6, pp. 761 – 777, 2011.

[37] F. M. Jiménez-Brenes, F. López-Granados, A. De Castro, J. Torres-Sánchez, N. Serrano, and J. Peña, "Quantifying pruning impacts on olive tree architecture and annual canopy growth by using uav-based 3d modelling," *Plant Methods*, vol. 13, no. 1, p. 55, 2017.

[38] H. Thorpe, R. Astrup, A. Trowbridge, and K. Coates, "Competition and tree crowns: A neighborhood analysis of three boreal tree species," *Forest Ecology and Management*, vol. 259, no. 8, pp. 1586 – 1596, 2010.

[39] H. Sterba, A. Blab, and K. Katzensteiner, "Adapting an individual tree growth model for norway spruce (picea abies l. karst.) in pure and mixed species stands," *Forest Ecology and Management*, vol. 159, no. 1, pp. 101 – 110, 2002. Forest Ecosystem Restoration.

[40] H. Hasenauer, *Concepts Within Tree Growth Modeling*, pp. 3–17. Berlin, Heidelberg: Springer Berlin Heidelberg, 2006.

[41] F. B. Sullivan, M. J. Ducey, D. A. Orwig, B. Cook, and M. W. Palace, "Comparison of lidar- and allometry-derived canopy height models in an eastern deciduous forest," *Forest Ecology and Management*, vol. 406, pp. 83–94, December 2017.

[42] D. Spittlehouse and R. B. Stewart, "Adaptation to climate change in forest management," 2003.

[43] L. Gómez-Aparicio, R. García-Valdés, P. Ruíz-Benito, and M. A. Zavala, "Disentangling the relative importance of climate, size and competition on tree growth in iberian forests: implications for forest management under global change," *Global Change Biology*, vol. 17, no. 7, pp. 2400–2414, 2011.

[44] A. Van Laar and A. Akça, *Forest mensuration*, vol. 13. Springer Science & Business Media, 2007.

[45] H. Hamraz, M. A. Contreras, and J. Zhang, "A robust approach for tree segmentation in deciduous forests using small-footprint airborne lidar data," *International Journal of Applied Earth Observation and Geoinformation*, vol. 52, pp. 532 – 541, 2016.

[46] R. E. McRoberts and E. O. Tomppo, "Remote sensing support for national forest inventories," *Remote Sensing of Environment*, vol. 110, no. 4, pp. 412 – 419, 2007. ForestSAT Special Issue.

[47] M. Köhl, S. Magnussen, and M. Marchetti, *Remote Sensing*, pp. 197–238. Berlin, Heidelberg: Springer Berlin Heidelberg, 2006.

[48] W. G. Rees, *Physical principles of remote sensing*. Cambridge university press, 2013.

[49] P. S. Thenkabail, J. G. Lyon, and A. Huete, "Advances in hyperspectral remote sensing of vegetation and agricultural croplands: Chapter 1," in *Hyperspectral Remote Sensing of Vegetation* (P. Thenkabail, J. Lyon, and A. Huete, eds.), CRC Press, 2012.

[50] S. Aggarwal, "Principles of remote sensing," *Satellite remote sensing and GIS applications in agricultural meteorology*, pp. 23–38, 2004.

[51] C. Secades, B. O'Connor, C. Brown, M. Walpole, *et al.*, "Earth observation for biodiversity monitoring: a review of current approaches and future opportunities for tracking progress towards the aichi biodiversity targets.," *CBD technical series*, no. 72, 2014.

[52] X. Zhang and W. Ni-meister, *Remote Sensing of Forest Biomass*, pp. 63–98. Berlin, Heidelberg: Springer Berlin Heidelberg, 2014.

[53] Q. Xie, J. Dash, W. Huang, D. Peng, Q. Qin, H. Mortimer, R. Casa, S. Pignatti, G. Laneve, S. Pascucci, Y. Dong, and H. Ye, "Vegetation indices combining the red and red-edge spectral information for leaf area index retrieval," *IEEE Journal of Selected Topics in Applied Earth Observations and Remote Sensing*, vol. 11, no. 5, pp. 1482–1493, 2018.

[54] F. D. Schneider, F. Morsdorf, B. Schmid, O. L. Petchey, A. Hueni, D. S. Schimel, and M. E. Schaepman, "Mapping functional diversity from remotely sensed morphological and physiological forest traits," *Nature Communications*, vol. 8, no. 1, 2017.

[55] M. Borengasser, W. S. Hungate, and R. Watkins, *Hyperspectral remote sensing: principles and applications*. CRC press, 2007.

[56] P. J. Gibson and C. H. Power, *Introductory remote sensing: Principles and concepts*. Psychology Press, 2000.

[57] E. Tomppo, H. Olsson, G. Ståhl, M. Nilsson, O. Hagner, and M. Katila, "Combining national forest inventory field plots and remote sensing data for forest databases," *Remote Sensing of Environment*, vol. 112, no. 5, pp. 1982 – 1999, 2008. Earth Observations for Terrestrial Biodiversity and Ecosystems Special Issue.

[58] H. Maas, A. Bienert, S. Scheller, and E. Keane, "Automatic forest inventory parameter determination from terrestrial laser scanner data," *International Journal of Remote Sensing*, vol. 29, no. 5, pp. 1579–1593, 2008.

[59] B. Cook, L. Corp, R. Nelson, E. Middleton, D. Morton, J. McCorkel, J. Masek, K. Ranson, V. Ly, and P. Montesano, "Nasa goddard's lidar, hyperspectral and thermal (g-liht) airborne imager," *Remote Sensing*, vol. 5, p. 4045–4066, Aug 2013.

[60] A. F. Goetz, "Three decades of hyperspectral remote sensing of the earth: A personal view," *Remote Sensing of Environment*, vol. 113, pp. S5 – S16, 2009. Imaging Spectroscopy Special Issue.

[61] J. M. Bioucas-Dias, A. Plaza, G. Camps-Valls, P. Scheunders, N. Nasrabadi, and J. Chanussot, "Hyperspectral remote sensing data analysis and future challenges," *IEEE Geoscience and Remote Sensing Magazine*, vol. 1, pp. 6–36, June 2013.

[62] R. Dorrepaal, C. Malegori, and A. Gowen, "Tutorial: Time series hyperspectral image analysis," *Journal of Near Infrared Spectroscopy*, vol. 24, no. 2, pp. 89–107, 2016.

[63] J. M. Bioucas-Dias, A. Plaza, N. Dobigeon, M. Parente, Q. Du, P. Gader, and J. Chanussot, "Hyperspectral unmixing overview: Geometrical, statistical, and sparse regression-based approaches," *IEEE Journal of Selected Topics in Applied Earth Observations and Remote Sensing*, vol. 5, pp. 354–379, April 2012.

[64] G. A. Shaw and H. K. Burke, "Spectral imaging for remote sensing," *Lincoln laboratory journal*, vol. 14, no. 1, pp. 3–28, 2003.

[65] M. J. Khan, H. S. Khan, A. Yousaf, K. Khurshid, and A. Abbas, "Modern trends in hyperspectral image analysis: A review," *IEEE Access*, vol. 6, pp. 14118–14129, 2018.

[66] A. A. Gitelson, "Nondestructive estimation of foliar pigment (chlorophylls, carotenoids, and anthocyanins) contents: Evaluating a semianalytical three-band model: Chapter 6," in *Hyperspectral Remote Sensing of Vegetation* (P. Thenkabail, J. Lyon, and A. Huete, eds.), CRC Press, 2012.

[67] A. A. Gitelson, Y. Gritz, and M. N. Merzlyak, "Relationships between leaf chlorophyll content and spectral reflectance and algorithms for non-destructive chlorophyll assessment in higher plant leaves," *Journal of plant physiology*, vol. 160, no. 3, pp. 271–282, 2003.

[68] A. A. Gitelson, G. P. Keydan, and M. N. Merzlyak, "Three-band model for noninvasive estimation of chlorophyll, carotenoids, and anthocyanin contents in higher plant leaves," *Geophysical Research Letters*, vol. 33, no. 11, 2006.

[69] X. Shen and L. Cao, "Tree-Species Classification in Subtropical Forests Using Airborne Hyperspectral and LiDAR Data," *Remote Sensing*, vol. 9, no. 11, p. 1180, 2017.

[70] C. Daughtry, C. Walthall, M. Kim, E. de Colstoun, and J. McMurtrey, "Estimating corn leaf chlorophyll concentration from leaf and canopy reflectance," *Remote Sensing of Environment*, vol. 74, no. 2, pp. 229 – 239, 2000.

[71] D. Haboudane, J. R. Miller, E. Pattey, P. J. Zarco-Tejada, and I. B. Strachan, "Hyperspectral vegetation indices and novel algorithms for predicting green lai of crop canopies: Modeling and validation in the context of precision agriculture," *Remote Sensing of Environment*, vol. 90, no. 3, pp. 337 – 352, 2004.

[72] J. Rousel, R. Haas, J. Schell, and D. Deering, "Monitoring vegetation systems in the great plains with erts," in *Proceedings of the Third Earth Resources Technology Satellite—1 Symposium; NASA SP-351*, pp. 309–317, 1973.

[73] K. Kandare, H. O. Ørka, M. Dalponte, E. Næsset, and T. Gobakken, "Individual tree crown approach for predicting site index in boreal forests using airborne laser scanning and hyperspectral data," *International Journal of Applied Earth Observation and Geoinformation*, vol. 60, no. September 2016, pp. 72–82, 2017.

[74] S. Luo, C. Wang, X. Xi, F. Pan, D. Peng, J. Zou, S. Nie, and H. Qin, "Fusion of airborne LiDAR data and hyperspectral imagery for aboveground and belowground forest biomass estimation," *Ecological Indicators*, vol. 73, pp. 378–387, 2017.

[75] L. Cao, J. Pan, R. Li, J. Li, and Z. Li, "Integrating airborne LiDAR and optical data to estimate forest aboveground biomass in arid and semi-arid regions of China," *Remote Sensing*, vol. 10, no. 4, 2018.

[76] J. Maschler, C. Atzberger, and M. Immitzer, "Individual tree crown segmentation and classification of 13 tree species using airborne hyperspectral data," *Remote Sensing*, vol. 10, p. 1218, Aug 2018.

[77] J. Lee, X. Cai, C. B. Schönlieb, and D. A. Coomes, "Nonparametric image registration of airborne LiDAR, hyperspectral and photographic imagery of wooded landscapes," *IEEE Transactions on Geoscience and Remote Sensing*, vol. 53, no. 11, pp. 6073–6084, 2015.

[78] N. R. Vaughn, G. P. Asner, P. G. Brodrick, R. E. Martin, J. W. Heckler, D. E. Knapp, and R. F. Hughes, "An approach for high-resolution mapping of Hawaiian Metrosideros Forest mortality using Laser-Guided Imaging Spectroscopy," *Remote Sensing*, vol. 10, no. 4, pp. 1–17, 2018.

[79] M. Dalponte, H. O. Ørka, L. T. Ene, T. Gobakken, and E. Næsset, "Tree crown delineation and tree species classification in boreal forests using hyperspectral and ALS data," *Remote Sensing of Environment*, vol. 140, pp. 306–317, 2014.

[80] Ø. D. Trier, A.-B. Salberg, M. Kermit, Ø. Rudjord, T. Gobakken, E. Næsset, and D. Aarsten, "Tree species classification in Norway from airborne hyperspectral and airborne laser scanning data," *European Journal of Remote Sensing*, vol. 51, no. 1, pp. 336–351, 2018.

[81] A. A. Gitelson, M. N. Merzlyak, and O. B. Chivkunova, "Optical properties and nondestructive estimation of anthocyanin content in plant leaves," *Photochemistry and Photobiology*, vol. 74, no. 1, pp. 38–45.

[82] A. A. Gitelson, Y. Zur, O. B. Chivkunova, and M. N. Merzlyak, "Assessing carotenoid content in plant leaves with reflectance spectroscopy," *Photochemistry and Photobiology*, vol. 75, no. 3, pp. 272–281, 2002.

[83] G. Metternicht, "Vegetation indices derived from high-resolution airborne videography for precision crop management," *International Journal of Remote Sensing*, vol. 24, no. 14, pp. 2855–2877, 2003.

[84] J. Peñuelas, I. Filella, C. Biel, L. Serrano, and R. Savé, "The reflectance at the 950–970 nm region as an indicator of plant water status," *International Journal of Remote Sensing*, vol. 14, no. 10, pp. 1887–1905, 1993.

[85] H. Torabzadeh, *Forest characterization by fusion of imaging spectroscopy and airborne laser scanning*. PhD thesis, University of Zurich, 2016.

[86] H. Torabzadeh, R. Leiterer, A. Hueni, M. E. Schaepman, and F. Morsdorf, "Tree species classification in a temperate mixed forest using a combination of imaging spectroscopy and airborne laser scanning," *Agricultural and Forest Meteorology*, vol. 279, p. 107744, 2019.

[87] H. Torabzadeh, F. Morsdorf, and M. E. Schaepman, "Fusion of imaging spectroscopy and airborne laser scanning data for characterization of forest ecosystems – a review," *ISPRS Journal of Photogrammetry and Remote Sensing*, vol. 97, pp. 25 – 35, 2014.

[88] P. S. Thenkabail, J. G. Lyon, and A. Huete, "Hyperspectral data mining: Chapter 4," in *Hyperspectral Remote Sensing of Vegetation* (P. Thenkabail, J. Lyon, and A. Huete, eds.), CRC Press, 2012.

[89] M. N. Favorskaya and L. C. Jain, *Overview of LiDAR Technologies and Equipment for Land Cover Scanning*, pp. 19–68. Cham: Springer International Publishing, 2017.

[90] J. Vauhkonen, M. Maltamo, R. E. McRoberts, and E. Næsset, "Introduction to forestry applications of airborne laser scanning," in *Forestry applications of airborne laser scanning*, pp. 1–16, Springer, 2014.

[91] K. Lim, P. Treitz, M. Wulder, B. St-Onge, and M. Flood, "Lidar remote sensing of forest structure," *Progress in physical geography*, vol. 27, no. 1, pp. 88–106, 2003.

[92] G. Vincent, C. Antin, M. Laurans, J. Heurtebize, S. Durrieu, C. Lavalley, and J. Dauzat, "Mapping plant area index of tropical evergreen forest by airborne laser scanning. A cross-validation study using LAI2200 optical sensor," *Remote Sensing of Environment*, vol. 198, pp. 254–266, 2017.

[93] W. Chen, X. Hu, W. Chen, Y. Hong, and M. Yang, "Airborne lidar remote sensing for individual tree forest inventory using trunk detection-aided mean shift clustering techniques," *Remote Sensing*, vol. 10, p. 1078, Jul 2018.

[94] C. Hug, A. Ullrich, and A. Grimm, "Litemapper-5600-a waveform-digitizing lidar terrain and vegetation mapping system," *International Archives of Photogrammetry, Remote Sensing and Spatial Information Sciences*, vol. 36, no. Part 8, p. W2, 2004.

[95] J.-M. Monnet, E. Mermin, J. Chanussot, and F. Berger, "Tree top detection using local maxima filtering: a parameter sensitivity analysis," in *10th International Conference on LiDAR Applications for Assessing Forest Ecosystems (Silvilaser 2010)*, (Freiburg, Germany), p. 9, Sept. 2010.

[96] A. Ferraz, F. Bretar, S. Jacquemoud, G. Gonçalves, L. Pereira, M. Tomé, and P. Soares, "3-D mapping of a multi-layered Mediterranean forest using ALS data," *Remote Sensing of Environment*, vol. 121, pp. 210 – 223, 2012.

[97] A. Ferraz, S. Saatchi, C. Mallet, and V. Meyer, "LiDAR detection of individual tree size in tropical forests," *Remote Sensing of Environment*, vol. 183, pp. 318–333, 2016.

[98] J. Williams, C. Schönlieb, T. Swinfield, J. Lee, X. Cai, L. Qie, and D. A. Coomes, "3D segmentation of trees through a flexible multiclass graph cut algorithm," *IEEE Transactions on Geoscience and Remote Sensing*, vol. 58, pp. 754–776, Feb 2020.

[99] M. V. Leeuwen, N. C. Coops, and M. A. Wulder, "Canopy surface reconstruction from a lidar point cloud using hough transform," *Remote Sensing Letters*, vol. 1, no. 3, pp. 125–132, 2010.

[100] L. A. Arroyo, C. Pascual, and J. A. Manzanera, "Fire models and methods to map fuel types: The role of remote sensing," *Forest Ecology and Management*, vol. 256, no. 6, pp. 1239 – 1252, 2008.

[101] M. García, D. Riaño, E. Chuvieco, J. Salas, and F. M. Danson, "Multispectral and lidar data fusion for fuel type mapping using support vector machine and decision rules," *Remote Sensing of Environment*, vol. 115, no. 6, pp. 1369 – 1379, 2011.

[102] J. A. Manzanera, A. García-Abril, C. Pascual, R. Tejera, S. Martín-Fernández, T. Tokola, and R. Valbuena, "Fusion of airborne lidar and multispectral sensors reveals synergic capabilities in forest structure characterization," *GIScience & Remote Sensing*, vol. 53, no. 6, pp. 723–738, 2016.

[103] E. Bergseng, H. O. Ørka, E. Næsset, and T. Gobakken, "Assessing forest inventory information obtained from different inventory approaches and remote sensing data sources," *Annals of forest science*, vol. 72, no. 1, pp. 33–45, 2015.

[104] E. Ayrey, S. Fraver, J. A. K. Jr., L. S. Kenefic, D. Hayes, A. R. Weiskittel, and B. E. Roth, "Layer stacking: A novel algorithm for individual forest tree segmentation from lidar point clouds," *Canadian Journal of Remote Sensing*, vol. 43, no. 1, pp. 16–27, 2017.

[105] E. Dambrine, J.-L. Dupouey, L. Laüt, L. Humbert, M. Thinon, T. Beaufils, and H. Richard, "Present forest biodiversity patterns in france related to former roman agriculture," *Ecology*, vol. 88, no. 6, pp. 1430–1439, 2007.

[106] A. S. R. Sanz, C. Fernandez, F. Mouillot, L. Ferrat, D. Istria, and V. Pasqualini, "Long-term forest dynamics and land-use abandonment in the mediterranean mountains, corsica, france," *Ecology and Society*, vol. 18, no. 2, 2013.

[107] L. Hinojosa, C. Napoléone, M. Moulery, and E. F. Lambin, "The "mountain effect" in the abandonment of grasslands: Insights from the french southern alps," *Agriculture, Ecosystems Environment*, vol. 221, pp. 115 – 124, 2016.

[108] D. MacDonald, J. R. Crabtree, G. Wiesinger, T. Dax, N. Stamou, P. Fleury, J. G. Lazpita, and A. Gibon, "Agricultural abandonment in mountain areas of europe: environmental consequences and policy response," *Journal of environmental management*, vol. 59, no. 1, pp. 47–69, 2000.

[109] P. Leskinen, G. Cardellini, S. González-García, E. Hurmekoski, R. Sathre, J. Seppälä, C. Smyth, T. Stern, and P. J. Verkerk, "Substitution effects of wood-based products in climate change mitigation," *From Science to Policy*, vol. 7, p. 28, 2018.

[110] F. Bilgili, E. Koçak, Ümit Bulut, and S. Kuşkaya, "Can biomass energy be an efficient policy tool for sustainable development?," *Renewable and Sustainable Energy Reviews*, vol. 71, pp. 830 – 845, 2017.

[111] U. Schirpke, C. Meisch, T. Marsoner, and U. Tappeiner, "Revealing spatial and temporal patterns of outdoor recreation in the european alps and their surroundings," *Ecosystem Services*, vol. 31, pp. 336 – 350, 2018. Assessment and Valuation of Recreational Ecosystem Services.

[112] S. Dupire, F. Bourrier, J.-M. Monnet, S. Bigot, L. Borgniet, F. Berger, and T. Curt, "Novel quantitative indicators to characterize the protective effect of mountain forests against rockfall," *Ecological Indicators*, vol. 67, pp. 98 – 107, 2016.

[113] R. Mainieri, A. Favillier, J. Lopez-Saez, N. Eckert, T. Zgheib, P. Morel, M. Saulnier, J.-L. Peiry, M. Stoffel, and C. Corona, "Impacts of land-cover changes on snow avalanche activity in the french alps," *Anthropocene*, vol. 30, p. 100244, 2020.

[114] M. Mina, H. Bugmann, T. Cordonnier, F. Irauschek, M. Klopcic, M. Pardos, and M. Cailleret, "Future ecosystem services from european mountain forests under climate change," *Journal of Applied Ecology*, vol. 54, no. 2, pp. 389–401, 2017.

[115] D. Vázquez-Tarrío, L. Borgniet, F. Liébault, and A. Recking, "Using uas optical imagery and sfm photogrammetry to characterize the surface grain size of gravel bars in a braided river (vénéon river, french alps)," *Geomorphology*, vol. 285, pp. 94 – 105, 2017.

[116] P. Bebi, R. Seidl, R. Motta, M. Fuhr, D. Firm, F. Krumm, M. Conedera, C. Ginzler, T. Wohlgemuth, and D. Kulakowski, "Changes of forest cover and disturbance regimes in the mountain forests of the alps," *Forest Ecology and Management*, vol. 388, pp. 43 – 56, 2017. Ecology of Mountain Forest Ecosystems in Europe.

[117] S. Chaudhuri and K. Kotwal, *Hyperspectral Image Fusion*. Springer, 2013.

[118] C. Pohl and J. Van Genderen, *Remote sensing image fusion: A practical guide*. CRC Press, 2016.

[119] C. Dechesne, *Segmentation sémantique de peuplement forestiers par analyse conjointe d'imagerie multispectrale très haute résolution et de données 3D LiDAR aéroportées*. PhD thesis, 2017. Thése de doctorat dirigée par Gouet-Brunet, Valérie Sciences et Technologies de l'Information Géographique Paris Est 2017.

[120] K. Kandare, *Fusion of airborne laser scanning and hyperspectral data for predicting forest characteristics at different spatial scales*. PhD thesis, 2017.

[121] M. Dalponte, L. Bruzzone, and D. Gianelle, "Fusion of hyperspectral and LiDAR remote sensing data for classification of complex forest areas," *Geoscience and Remote Sensing, IEEE Transactions on*, vol. 46, no. 5, pp. 1416–1427, 2008.

[122] M. Dalponte, L. Bruzzone, and D. Gianelle, "Tree species classification in the Southern Alps based on the fusion of very high geometrical resolution multispectral/hyperspectral images and LiDAR data," *Remote Sensing of Environment*, vol. 123, pp. 258–270, 2012.

[123] M. Alonzo, B. Bookhagen, and D. A. Roberts, "Urban tree species mapping using hyperspectral and LiDAR data fusion," *Remote Sensing of Environment*, vol. 148, pp. 70–83, 2014.

[124] H. Torabzadeh, F. Morsdorf, R. Leiterer, and M. E. Schaepman, "Fusing imaging spectrometry and airborne laser scanning data for tree species discrimination," *2014 IEEE Geoscience and Remote Sensing Symposium*, no. October 2015, pp. 1253–1256, 2014.

[125] H. Torabzadeh, R. Leiterer, M. E. Schaepman, and F. Morsdorf, "Optimal structural and spectral features for tree species classification using combined airborne laser scanning and hyperspectral data," *2015 IEEE International Geoscience and Remote Sensing Symposium (IGARSS)*, no. March, pp. 5399–5402, 2015.

[126] C. Sommer, S. Holzwarth, U. Heiden, and M. Heurich, "Feature-Based Tree Species Classification Using Hyperspectral and LiDAR Data," *EARSeL eProceedings 14, Special Issue*, no. 2, pp. 49–70, 2015.

[127] J. Lee, X. Cai, J. Lellmann, M. Dalponte, Y. Malhi, N. Butt, M. Morecroft, C.-B. Schonlieb, and D. Coomes, "Individual Tree Species Classification from Airborne Multisensor Imagery Using Robust PCA," *IEEE Journal of Selected Topics in Applied Earth Observations and Remote Sensing*, vol. 9, no. 6, pp. 2554–2567, 2016.

[128] Y. Dian, Y. Pang, Y. Dong, and Z. Li, "Urban Tree Species Mapping Using Airborne LiDAR and Hyperspectral Data," *Journal of the Indian Society of Remote Sensing*, vol. 44, no. 4, pp. 595–603, 2016.

[129] Z. Zhang, A. Kazakova, L. M. Moskal, and D. M. Styers, "Object-based tree species classification in urban ecosystems using LiDAR and hyperspectral data," *Forests*, vol. 7, no. 6, pp. 1–16, 2016.

[130] W. Liao, F. Van Coillie, L. Li, B. Zhao, L. Gao, W. Philips, and B. Zhang, "Fusion of multiscale hyperspectral and LiDAR features for tree species mapping," in *International Geoscience and Remote Sensing Symposium (IGARSS)*, vol. 2017-July, pp. 2879–2882, 2017.

[131] T. Sankey, J. Donager, J. McVay, and J. B. Sankey, "Uav lidar and hyperspectral fusion for forest monitoring in the southwestern usa," *Remote Sensing of Environment*, vol. 195, no. Supplement C, pp. 30 – 43, 2017.

[132] F. M. Van Coillie, W. Liao, P. Kempeneers, K. Vandekerkhove, S. Gautama, W. Philips, and R. R. De Wulf, "Optimized feature fusion of LiDAR and hyperspectral data for tree species mapping in closed forest canopies," in *Workshop on Hyperspectral Image and Signal Processing, Evolution in Remote Sensing*, vol. 2015-June, 2017.

[133] T. T. Sankey, J. McVay, T. L. Swetnam, M. P. McClaran, P. Heilman, and M. Nichols, "UAV hyperspectral and LiDAR data and their fusion for arid and semi-arid land vegetation monitoring," *Remote Sensing in Ecology and Conservation*, vol. 4, no. 1, pp. 20–33, 2018.

[134] G. P. Asner, D. E. Knapp, T. Kennedy-Bowdoin, M. O. Jones, R. E. Martin, J. Boardman, and R. F. Hughes, "Invasive species detection in Hawaiian rainforests using airborne imaging spectroscopy and LiDAR," *Remote Sensing of Environment*, vol. 112, no. 5, pp. 1942–1955, 2008.

[135] T. Matsuki, N. Yokoya, and A. Iwasaki, "Hyperspectral tree species classification of japanese complex mixed forest with the aid of lidar data," *IEEE Journal of Selected Topics in Applied Earth Observations and Remote Sensing*, vol. 8, pp. 2177–2187, May 2015.

[136] B. F. Leutner, B. Reineking, J. Müller, M. Bachmann, C. Beierkuhnlein, S. Dech, and M. Wegmann, "Modelling forest α-diversity and floristic composition - on the added value of LiDAR plus hyperspectral remote sensing," *Remote Sensing*, vol. 4, no. 9, pp. 2818–2845, 2012.

[137] M. Alonzo, J. P. McFadden, D. J. Nowak, and D. A. Roberts, "Mapping urban forest structure and function using hyperspectral imagery and LiDAR data," *Urban Forestry and Urban Greening*, vol. 17, pp. 135–147, 2016.

[138] A. Descals, L. Alonso, and G. Camps-Valls, "Predicting year of plantation with hyperspectral and LiDAR data," in *International Geoscience and Remote Sensing Symposium (IGARSS)*, vol. 2017-July, pp. 1780–1783, 2017.

[139] A. A. Plowright, N. C. Coops, C. M. Chance, S. R. Sheppard, and N. W. Aven, "Multiscale analysis of relationship between imperviousness and urban tree height using airborne remote sensing," *Remote Sensing of Environment*, vol. 194, pp. 391–400, 2017.

[140] C. R. Hakkenberg, K. Zhu, R. K. Peet, and C. Song, "Mapping multi-scale vascular plant richness in a forest landscape with integrated lidar and hyperspectral remote-sensing," *Ecology*, vol. 99, no. 2, pp. 474–487, 2018.

[141] C. R. Hakkenberg, R. K. Peet, D. L. Urban, and C. Song, "Modeling plant composition as community continua in a forest landscape with LiDAR and hyperspectral remote sensing:," *Ecological Applications*, vol. 28, no. 1, pp. 177–190, 2018.

[142] Y. Zhao, Y. Zeng, Z. Zheng, W. Dong, D. Zhao, B. Wu, and Q. Zhao, "Forest species diversity mapping using airborne LiDAR and hyperspectral data in a subtropical forest in China," *Remote Sensing of Environment*, vol. 213, no. January 2017, pp. 104–114, 2018.

[143] A. Ceballos, J. Hernández, P. Corvalán, and M. Galleguillos, "Comparison of airborne LiDAR and satellite hyperspectral remote sensing to estimate vascular plant richness in deciduous mediterranean forests of central Chile," *Remote Sensing*, vol. 7, no. 3, pp. 2692–2714, 2015.

[144] J. Lee, X. Cai, C. B. Schoenlieb, and D. Coomes, "Mapping individual trees from airborne multi-sensor imagery," *2015 IEEE International Geoscience and Remote Sensing Symposium (IGARSS)*, pp. 5411–5414, 2015.

[145] G. P. Asner, C. B. Anderson, R. E. Martin, R. Tupayachi, D. E. Knapp, and F. Sinca, "Landscape biogeochemistry reflected in shifting distributions of chemical traits in the Amazon forest canopy," *Nature Geoscience*, vol. 8, no. 7, pp. 567–575, 2015.

[146] G. P. Asner, R. E. Martin, C. B. Anderson, and D. E. Knapp, "Quantifying forest canopy traits: Imaging spectroscopy versus field survey," *Remote Sensing of Environment*, vol. 158, pp. 15–27, 2015.

[147] R. E. Martin, K. Dana Chadwick, P. G. Brodrick, L. Carranza-Jimenez, N. R. Vaughn, and G. P. Asner, "An approach for foliar trait retrieval from airborne imaging spectroscopy of tropical forests," *Remote Sensing*, vol. 10, no. 2, 2018.

[148] T. Jucker, B. Bongalov, D. F. Burslem, R. Nilus, M. Dalponte, S. L. Lewis, O. L. Phillips, L. Qie, and D. A. Coomes, "Topography shapes the structure, composition and function of tropical forest landscapes," *Ecology Letters*, vol. 21, no. 7, pp. 989–1000, 2018.

[149] R. E. Martin, G. P. Asner, E. Francis, A. Ambrose, W. Baxter, A. J. Das, N. R. Vaughn, T. Paz-Kagan, T. Dawson, K. Nydick, and N. L. Stephenson, "Remote measurement of canopy water content in giant sequoias (Sequoiadendron giganteum) during drought," *Forest Ecology and Management*, vol. 419-420, no. November 2017, pp. 279–290, 2018.

[150] M. Dalponte, L. Bruzzone, and D. Gianelle, "Fusion of hyperspectral and LiDAR remote sensing data for the estimation of tree stem diameters," *International Geoscience and Remote Sensing Symposium (IGARSS)*, vol. 2, pp. 1008–1011, 2009.

[151] P. H. La, Y. D. Eo, Q. M. Nguyen, and S. W. Kim, "Individual tree crown estimation using hyperspectral image and lidar data," in *2012 7th International Conference on Computing and Convergence Technology (ICCCT)*, pp. 1413–1416, Dec 2012.

[152] H. P. La, Y. D. Eo, A. Chang, and C. Kim, "Extraction of individual tree crown using hyperspectral image and LiDAR data," *KSCE Journal of Civil Engineering*, vol. 19, no. 4, pp. 1078–1087, 2015.

[153] M. Dalponte, L. Frizzera, and D. Gianelle, "Fusion of hyperspectral and LiDAR data for forest attributes estimation," *International Geoscience and Remote Sensing Symposium (IGARSS)*, pp. 788–791, 2014.

[154] C. Zhang, Y. Zhou, and F. Qiu, "Individual Tree Segmentation from LiDAR Point Clouds for Urban Forest Inventory," *Remote Sensing*, vol. 7, no. 6, pp. 7892–7913, 2015.

[155] K. Kandare, M. Dalponte, H. O. Ørka, L. Frizzera, and E. Næsset, "Prediction of species-specific volume using different inventory approaches by fusing airborne laser scanning and hyperspectral data," *Remote Sensing*, vol. 9, no. 5, pp. 1–19, 2017.

[156] J. Lee, D. Coomes, C.-B. Schonlieb, X. Cai, J. Lellmann, M. Dalponte, Y. Malhi, N. Butt, and M. Morecroft, "A graph cut approach to 3D tree delineation, using integrated airborne LiDAR and hyperspectral imagery," *Computer Vision and Pattern Recognition*, pp. 1–24, 2017.

[157] M. Dalponte, F. Reyes, K. Kandare, and D. Gianelle, "Delineation of individual tree crowns from ALS and hyperspectral data: A comparison among four methods," *European Journal of Remote Sensing*, vol. 48, pp. 365–382, 2015.

[158] D. Dutta, K. Wang, E. Lee, A. Goodwell, D. K. Woo, D. Wagner, and P. Kumar, "Characterizing Vegetation Canopy Structure Using Airborne Remote Sensing Data," *IEEE Transactions on Geoscience and Remote Sensing*, vol. 55, no. 2, pp. 1160–1178, 2017.

[159] M. Dalponte and D. A. Coomes, "Tree-centric mapping of forest carbon density from airborne laser scanning and hyperspectral data," *Methods in Ecology and Evolution*, vol. 7, no. 10, pp. 1236–1245, 2016.

[160] O. Brovkina, J. Novotny, E. Cienciala, F. Zemek, and R. Russ, "Mapping forest aboveground biomass using airborne hyperspectral and LiDAR data in the mountainous conditions of Central Europe," *Ecological Engineering*, vol. 100, pp. 219–230, 2017.

[161] M. Dalponte, L. Frizzera, H. O. Ørka, T. Gobakken, E. Næsset, and D. Gianelle, "Predicting stem diameters and aboveground biomass of individual trees using remote sensing data," *Ecological Indicators*, vol. 85, no. May 2017, pp. 367–376, 2018.

[162] C. S. Balzotti and G. P. Asner, "Biotic and Abiotic Controls Over Canopy Function and Structure in Humid Hawaiian Forests," *Ecosystems*, vol. 21, no. 2, pp. 331–348, 2018.

[163] W. Xiao, A. Zaforemska, M. Smigaj, Y. Wang, and R. Gaulton, "Mean shift segmentation assessment for individual forest tree delineation from airborne LiDAR data," *Remote Sensing*, vol. 11, no. 11, pp. 1–19, 2019.

[164] E. Tusa, J. Monnet, J. Barré, M. D. Mura, M. Dalponte, and J. Chanussot, "Individual tree segmentation based on mean shift and crown shape model for temperate forest," *IEEE Geoscience and Remote Sensing Letters*, pp. 1–5, 2020.

[165] C. Dechesne, C. Mallet, A. Le Bris, and V. Gouet-Brunet, "Semantic segmentation of forest stands of pure species combining airborne LiDAR data and very high resolution multispectral imagery," *ISPRS Journal of Photogrammetry and Remote Sensing*, vol. 126, pp. 129–145, 2017.

[166] W. Liao, J. Chanussot, and W. Philips, *Remote Sensing Data Fusion: Guided Filter-Based Hyperspectral Pansharpening and Graph-Based Feature-Level Fusion*, pp. 243–275. Cham: Springer International Publishing, 2018.

[167] W. Liao, F. Van Coillie, L. Gao, L. Li, B. Zhang, and J. Chanussot, "Deep learning for fusion of apex hyperspectral and full-waveform lidar remote sensing data for tree species mapping," *IEEE Access*, vol. 6, pp. 68716–68729, 2018.

[168] C. Pohl and J. L. V. Genderen, "Review article multisensor image fusion in remote sensing: Concepts, methods and applications," *International Journal of Remote Sensing*, vol. 19, no. 5, pp. 823–854, 1998.

[169] J. Jensen, *Introductory Digital Image Processing: A Remote Sensing Perspective*. Always Learning, Pearson Education, Incorporated, 2016.

[170] K. Kandare, H. O. Ørka, J. C.-W. Chan, and M. Dalponte, "Effects of forest structure and airborne laser scanning point cloud density on 3D delineation of individual tree crowns," *European Journal of Remote Sensing*, vol. 49, no. 1, pp. 337–359, 2016.

[171] J. Chapman, I.-k. Hung, and J. Tippen, "Evaluating Tiffs (Toolbox for LiDAR Data Filtering and Forest Studies) in deriving forest measurements from LiDAR data," *International Journal of Mathematical and Computational Forestry & Natural-Resource Sciences*, vol. 2, no. 2, pp. 145–152, 2010.

[172] R. J. McGaughey *et al.*, "Fusion/ldv: Software for lidar data analysis and visualization," *US Department of Agriculture, Forest Service, Pacific Northwest Research Station: Seattle, WA, USA*, vol. 123, no. 2, 2009.

[173] J. Roussel and D. Auty, "lidr: Airborne lidar data manipulation and visualization for forestry applications," 2017.

[174] A. Khosravipour, A. K. Skidmore, M. Isenburg, T. Wang, and Y. A. Hussin, "Generating pit-free canopy height models from airborne lidar," *Photogrammetric Engineering & Remote Sensing*, vol. 80, no. 9, pp. 863–872, 2014.

[175] X. Liu, Z. Zhang, J. Peterson, and S. Chandra, "LiDAR-derived high quality ground control information and DEM for image orthorectification," *GeoInformatica*, vol. 11, pp. 37–53, Jan. 2007.

[176] F. Gao, J. G. Masek, and R. E. Wolfe, "Automated registration and orthorectification package for Landsat and Landsat-like data processing," *Journal of Applied Remote Sensing*, vol. 3, no. 1, pp. 1 – 20, 2009.

[177] J. Xia, N. Yokoya, and A. Iwasaki, "Fusion of hyperspectral and lidar data with a novel ensemble classifier," *IEEE Geoscience and Remote Sensing Letters*, vol. 15, no. 6, pp. 957–961, 2018.

[178] et all Rogério dos Santos Alves; Alex Soares de Souza, "Medication image registration," *Igarss 2014*, no. 1, pp. 1–5, 2014.

[179] G. Brigot, E. Colin-Koeniguer, A. Plyer, and F. Janez, "Adaptation and evaluation of an optical flow method applied to coregistration of forest remote sensing images," *IEEE Journal of Selected Topics in Applied Earth Observations and Remote Sensing*, vol. 9, no. 7, pp. 2923–2939, 2016.

[180] M. Brell, C. Rogass, K. Segl, B. Bookhagen, and L. Guanter, "Improving Sensor Fusion: A Parametric Method for the Geometric Coalignment of Airborne Hyperspectral and LiDAR Data," *IEEE Transactions on Geoscience and Remote Sensing*, vol. 54, no. 6, pp. 3460–3474, 2016.

[181] G. Vaglio Laurin, Q. Chen, J. A. Lindsell, D. A. Coomes, F. D. Frate, L. Guerriero, F. Pirotti, and R. Valentini, "Above ground biomass estimation in an african tropical forest with lidar and hyperspectral data," *ISPRS Journal of Photogrammetry and Remote Sensing*, vol. 89, pp. 49 – 58, 2014.

[182] A. Roncat, C. Briese, and N. Pfeifer, "A comparison of LiDAR reflectance and radiometrically calibrated hyperspectral imagery," *International Archives of the Photogrammetry, Remote Sensing and Spatial Information Sciences - ISPRS Archives*, vol. 41, no. July, pp. 705–710, 2016.

[183] G. Kumar and P. K. Bhatia, "A detailed review of feature extraction in image processing systems," *International Conference on Advanced Computing and Communication Technologies, ACCT*, pp. 5–12, 2014.

[184] N. S. Goel and W. Qin, "Influences of canopy architecture on relationships between various vegetation indices and lai and fpar: A computer simulation," *Remote Sensing Reviews*, vol. 10, no. 4, pp. 309–347, 1994.

[185] J.-L. Roujean and F.-M. Breon, "Estimating par absorbed by vegetation from bidirectional reflectance measurements," *Remote sensing of Environment*, vol. 51, no. 3, pp. 375–384, 1995.

[186] Z. Yang, P. Willis, and R. Mueller, "Impact of band-ratio enhanced awifs image to crop classification accuracy," in *Proc. Pecora*, vol. 17, pp. 1–11, 2008.

[187] A. A. Gitelson and M. N. Merzlyak, "Remote sensing of chlorophyll concentration in higher plant leaves," *Advances in Space Research*, vol. 22, no. 5, pp. 689–692, 1998.

[188] M. Louhaichi, M. M. Borman, and D. E. Johnson, "Spatially located platform and aerial photography for documentation of grazing impacts on wheat," *Geocarto International*, vol. 16, no. 1, pp. 65–70, 2001.

[189] R. E. Crippen, "Calculating the vegetation index faster," *Remote sensing of Environment*, vol. 34, no. 1, pp. 71–73, 1990.

[190] A. Bannari, H. Asalhi, and P. M. Teillet, "Transformed difference vegetation index (tdvi) for vegetation cover mapping," in *IEEE International Geoscience and Remote Sensing Symposium*, vol. 5, pp. 3053–3055 vol.5, 2002.

[191] E. R. Hunt Jr., C. S. T. Daughtry, J. U. H. Eitel, and D. S. Long, "Remote sensing leaf chlorophyll content using a visible band index," *Agronomy Journal*, vol. 103, no. 4, pp. 1090–1099, 2011.

[192] C. J. Tucker, "Red and photographic infrared linear combinations for monitoring vegetation," *Remote Sensing of Environment*, vol. 8, no. 2, pp. 127 – 150, 1979.

[193] R. P. Sripada *et al.*, "Determining in-season nitrogen requirements for corn using aerial color-infrared photography," 2005.

[194] "Discrimination of growth and water stress in wheat by various vegetation indices through clear and turbid atmospheres," *Remote Sensing of Environment*, vol. 13, no. 3, pp. 187 – 208, 1983.

[195] A. Huete, K. Didan, T. Miura, E. P. Rodriguez, X. Gao, and L. G. Ferreira, "Overview of the radiometric and biophysical performance of the modis vegetation indices," *Remote sensing of environment*, vol. 83, no. 1-2, pp. 195–213, 2002.

[196] Z. Jiang, A. R. Huete, K. Didan, and T. Miura, "Development of a two-band enhanced vegetation index without a blue band," *Remote Sensing of Environment*, vol. 112, no. 10, pp. 3833 – 3845, 2008.

[197] E. Boegh, H. Soegaard, N. Broge, C. Hasager, N. Jensen, K. Schelde, and A. Thomsen, "Airborne multispectral data for quantifying leaf area index, nitrogen concentration, and photosynthetic efficiency in agriculture," *Remote Sensing of Environment*, vol. 81, no. 2, pp. 179 – 193, 2002.

[198] G. S. Birth and G. R. McVey, "Measuring the color of growing turf with a reflectance spectrophotometer1," *Agronomy Journal*, vol. 60, no. 6, pp. 640–643, 1968.

[199] J. M. Chen, "Evaluation of vegetation indices and a modified simple ratio for boreal applications," *Canadian Journal of Remote Sensing*, vol. 22, no. 3, pp. 229–242, 1996.

[200] R. P. Sripada, R. W. Heiniger, J. G. White, and A. D. Meijer, "Aerial color infrared photography for determining early in-season nitrogen requirements in corn," *Agronomy Journal*, vol. 98, no. 4, pp. 968–977, 2006.

[201] L. Waser, M. Küchler, K. Jütte, and T. Stampfer, "Evaluating the potential of worldview-2 data to classify tree species and different levels of ash mortality," *Remote Sensing*, vol. 6, p. 4515–4545, May 2014.

[202] D. B. Lobell and G. P. Asner, "Hyperion studies of crop stress in mexico," 2004.

[203] A. Huete, "A soil-adjusted vegetation index (savi). remote ssensing of environment, 25, 295-309," 1988.

[204] G. Rondeaux, M. Steven, and F. Baret, "Optimization of soil-adjusted vegetation indices," *Remote sensing of environment*, vol. 55, no. 2, pp. 95–107, 1996.

[205] J. Qi, A. Chehbouni, A. Huete, Y. Kerr, and S. Sorooshian, "A modified soil adjusted vegetation index," *Remote Sensing of Environment*, vol. 48, no. 2, pp. 119 – 126, 1994.

[206] A. A. Gitelson, Y. J. Kaufman, M. N. Merzlyak, *et al.*, "Use of a green channel in remote sensing of global vegetation from eos-modis," *Remote sensing of Environment*, vol. 58, no. 3, pp. 289–298, 1996.

[207] A. A. Gitelson, R. Stark, U. Grits, D. Rundquist, Y. Kaufman, and D. Derry, "Vegetation and soil lines in visible spectral space: A concept and technique for remote estimation of vegetation fraction," *International Journal of Remote Sensing*, vol. 23, no. 13, pp. 2537–2562, 2002.

[208] A. A. Gitelson, "Wide dynamic range vegetation index for remote quantification of biophysical characteristics of vegetation," *Journal of Plant Physiology*, vol. 161, no. 2, pp. 165 – 173, 2004.

[209] G. M. Henebry, A. Viña, and A. A. Gitelson, "The wide dynamic range vegetation index and its potential utility for gap analysis," 2004.

[210] O. Mutanga and A. K. Skidmore, "Narrow band vegetation indices overcome the saturation problem in biomass estimation," *International Journal of Remote Sensing*, vol. 25, no. 19, pp. 3999–4014, 2004.

[211] A. Gitelson and M. N. Merzlyak, "Spectral reflectance changes associated with autumn senescence of aesculus hippocastanum l. and acer platanoides l. leaves. spectral features and relation to chlorophyll estimation," *Journal of Plant Physiology*, vol. 143, no. 3, pp. 286 – 292, 1994.

[212] D. A. Sims and J. A. Gamon, "Relationships between leaf pigment content and spectral reflectance across a wide range of species, leaf structures and developmental stages," *Remote Sensing of Environment*, vol. 81, no. 2, pp. 337 – 354, 2002.

[213] B. Datt, "A new reflectance index for remote sensing of chlorophyll content in higher plants: Tests using eucalyptus leaves," *Journal of Plant Physiology*, vol. 154, no. 1, pp. 30 – 36, 1999.

[214] J. Vogelmann, B. Rock, and D. Moss, "Red edge spectral measurements from sugar maple leaves," *International Journal of Remote Sensing*, vol. 14, no. 8, pp. 1563–1575, 1993.

[215] G. Guyot, F. Baret, and D. Major, "High spectral resolution : determination of spectral shifts between the red and near infrared," in *ISPRS Congress*, (Kyoto, Japan), July 1988.

[216] Y. J. Kaufman and D. Tanre, "Atmospherically resistant vegetation index (arvi) for eos-modis," *IEEE Transactions on Geoscience and Remote Sensing*, vol. 30, no. 2, pp. 261–270, 1992.

[217] N. Broge and E. Leblanc, "Comparing prediction power and stability of broadband and hyperspectral vegetation indices for estimation of green leaf area index and canopy chlorophyll density," *Remote Sensing of Environment*, vol. 76, no. 2, pp. 156 – 172, 2001.

[218] J. Peñuelas, I. Filella, and J. A. Gamon

[219] J. A. Gamon, L. Serrano, and J. Surfus, "The photochemical reflectance index: an optical indicator of photosynthetic radiation use efficiency across species, functional types, and nutrient levels," *Oecologia*, vol. 112, no. 4, pp. 492–501, 1997.

[220] J. Peñuelas, F. Baret, and I. Filella, "Semi-empirical indices to assess carotenoids/chlorophyll a ratio from leaf spectral reflectance," *Photosynthetica*, vol. 31, no. 2, pp. 221–230, 1995.

[221] J. Gamon and J. Surfus, "Assessing leaf pigment content and activity with a reflectometer," *New Phytologist*, vol. 143, no. 1, p. 105–117, 1999.

[222] T. Zheng and J. M. Chen, "Photochemical reflectance ratio for tracking light use efficiency for sunlit leaves in two forest types," *ISPRS Journal of Photogrammetry and Remote Sensing*, vol. 123, pp. 47 – 61, 2017.

[223] M. N. Merzlyak, A. A. Gitelson, O. B. Chivkunova, and V. Y. Rakitin, "Non-destructive optical detection of pigment changes during leaf senescence and fruit ripening," *Physiologia Plantarum*, vol. 106, no. 1, pp. 135–141, 1999.

[224] R. M. Haralick, K. Shanmugam, and I. Dinstein, "Textural features for image classification," *IEEE Transactions on Systems, Man, and Cybernetics*, vol. SMC-3, pp. 610–621, Nov 1973.

[225] G. Tochon, J. Féret, S. Valero, R. Martin, D. Knapp, P. Salembier, J. Chanussot, and G. Asner, "On the use of binary partition trees for the tree crown segmentation of tropical rainforest hyperspectral images," *Remote Sensing of Environment*, vol. 159, pp. 318 – 331, 2015.

[226] P. Ghamisi, J. A. Benediktsson, and S. Phinn, "Land-cover classification using both hyperspectral and LiDAR data," *International Journal of Image and Data Fusion*, vol. 6, no. 3, pp. 189–215, 2015.

[227] Y. Liu, S. T. Monteiro, and E. Saber, "An approach for combining airborne LiDAR and high-resolution aerial color imagery using Gaussian processes," *SPIE Remote Sensing*, p. 96430Z, 2015.

[228] W. Liao, M. Dalla Mura, J. Chanussot, and A. Pižurica, "Fusion of spectral and spatial information for classification of hyperspectral remote-sensed imagery by local graph," *IEEE Journal of Selected Topics in Applied Earth Observations and Remote Sensing*, vol. 9, no. 2, pp. 583–594, 2016.

[229] W. Liao, A. Pižurica, R. Bellens, S. Gautama, and W. Philips, "Generalized graph-based fusion of hyperspectral and lidar data using morphological features," *IEEE Geoscience and Remote Sensing Letters*, vol. 12, no. 3, pp. 552–556, 2015.

[230] B. Schölkopf, A. Smola, and K.-R. Müller, "Nonlinear component analysis as a kernel eigenvalue problem," *Neural Computation*, vol. 10, no. 5, pp. 1299–1319, 1998.

[231] F. E. Fassnacht, H. Latifi, K. Stereńczak, A. Modzelewska, M. Lefsky, L. T. Waser, C. Straub, and A. Ghosh, "Review of studies on tree species classification from remotely sensed data," *Remote Sensing of Environment*, vol. 186, pp. 64 – 87, 2016.

[232] A. Ghosh, F. Fassnacht, P. Joshi, and B. Kochb, "A framework for mapping tree species combining hyperspectral and lidar data: Role of selected classifiers and sensor across three spatial scales," *International Journal of Applied Earth Observation and Geoinformation*, vol. 26, no. 1, pp. 49–63, 2014.

[233] L. Ballanti, L. Blesius, E. Hines, and B. Kruse, "Tree species classification using hyperspectral imagery: A comparison of two classifiers," *Remote Sensing*, vol. 8, no. 6, 2016.

[234] L. Ene, E. Næsset, and T. Gobakken, "Single tree detection in heterogeneous boreal forests using airborne laser scanning and area-based stem number estimates," *International Journal of Remote Sensing*, vol. 33, no. 16, pp. 5171–5193, 2012.

[235] J. Hyyppä, O. Kelle, M. Lehikoinen, and M. Inkinen, "A segmentation-based method to retrieve stem volume estimates from 3-D tree height models produced by laser scanners," *IEEE Transactions on Geoscience and Remote Sensing*, vol. 39, no. 5, pp. 969–975, 2001.

[236] M. Dalponte, "R package'itcsegment': User manual," 2016.

[237] M. Malakini, S. Makungwa, W. Mwase, and A. M. Maganga, "Allometric models for estimating above- and below- ground tree carbon for community managed miombo woodlands: A case of miyobe village forest area in northern malawi," *Trees, Forests and People*, vol. 2, p. 100024, 2020.

[238] A. N. Djomo and C. D. Chimi, "Tree allometric equations for estimation of above, below and total biomass in a tropical moist forest: Case study with application to remote sensing," *Forest Ecology and Management*, vol. 391, pp. 184 – 193, 2017.

[239] S.-I. Aiba and T. Kohyama, "Tree species stratification in relation to allometry and demography in a warm-temperate rain forest," *Journal of Ecology*, vol. 84, no. 2, pp. 207–218, 1996.

[240] S. C. Popescu, R. H. Wynne, and R. F. Nelson, "Estimating plot-level tree heights with LiDAR: local filtering with a canopy-height based variable window size," *Computers and Electronics in Agriculture*, vol. 37, no. 1, pp. 71 – 95, 2002.

[241] J.-M. Monnet, *Caractérisation des forêts de montagne par scanner laser aéroporté: estimation de paramètres de peuplement par régression SVM et apprentissage non supervisé pour la détection de sommets*. PhD thesis, Université de Grenoble, 2011.

[242] "Orchamp." https://orchamp.osug.fr/sites/4. (Accessed on 10/01/2020).

[243] R. G. D'Eon, R. Serrouya, G. Smith, and C. O. Kochanny, "Gps radiotelemetry error and bias in mountainous terrain," *Wildlife Society Bulletin (1973-2006)*, vol. 30, no. 2, pp. 430–439, 2002.

[244] R. Valbuena, F. Mauro, R. R.-S. Suárez, and J. Manzanera, "Accuracy and precision of gps receivers under forest canopies in a mountainous environment," *Spanish Journal of Agricultural Research*, no. 4, pp. 1047–1057, 2010.

[245] J.-M. Monnet and Mermin, "Cross-correlation of diameter measures for the co-registration of forest inventory plots with airborne laser scanning data," *Forests*, vol. 5, p. 2307–2326, Sep 2014.

[246] R. Reid and P. Stephen, *The Farmer's log 1999*. University of Melbourne, Dept. of Forestry, 1999.

[247] P. West, *Tree and Forest Measurement*. 2015.

[248] B. Leverett and D. Bertolette, "Measuring guidelines handbook," *American Forest. american forests. org/wp-content/uploads/2014/12/AF-Tree-Measuring-Guidelines_LR*, 2015.

[249] M. Maltamo, J. Hyyppä, and J. Malinen, "A comparative study of the use of laser scanner data and field measurements in the prediction of crown height in boreal forests," *Scandinavian Journal of Forest Research*, vol. 21, no. 3, pp. 231–238, 2006.

[250] H. Pretzsch, P. Biber, E. Uhl, J. Dahlhausen, and T. R "Crown size and growing space requirement of common tree species in urban centres, parks, and forests," *Urban Forestry & Urban Greening*, vol. 14, no. 3, pp. 466 – 479, 2015.

[251] K. Parthiban, S. Vennila, S. Kanna, and P. Durairasu, *Objective Forestry : For All Competitive Examination, 2Nd Ed.* SCIENTIFIC PUBLISHER (IND., 2015.

[252] E. Tusa, A. Laybros, J.-M. Monnet, M. D. Mura, J.-B. Barré, G. Vincent, M. Dalponte, J.-B. Féret, and J. Chanussot, "Chapter 2.11 - Fusion of hyperspectral imaging and LiDAR for forest monitoring," in *Hyperspectral Imaging* (J. M. Amigo, ed.), vol. 32 of *Data Handling in Science and Technology*, pp. 281 – 303, Elsevier, 2020.

[253] E. Tusa, J.-M. Monnet, J.-B. Barré, M. Dalla Mura, and J. Chanussot, "Fusion of lidar and hyperspectral data for semantic segmentation of forest tree species," *The International Archives of Photogrammetry, Remote Sensing and Spatial Information Sciences*, vol. 43, pp. 487–494, 2020.

[254] D. Schläpfer and R. Richter, "Geo-atmospheric processing of airborne imaging spectrometry data. part 1: Parametric orthorectification," *International Journal of Remote Sensing*, vol. 23, no. 13, pp. 2609–2630, 2002.

[255] R. Richter and D. Schläpfer, "Geo-atmospheric processing of airborne imaging spectrometry data. part 2: Atmospheric/topographic correction," *International Journal of Remote Sensing*, vol. 23, no. 13, pp. 2631–2649, 2002.

[256] D. Schläpfer, R. Richter, and T. Feingersh, "Operational brdf effects correction for wide-field-of-view optical scanners (brefcor)," *IEEE Transactions on Geoscience and Remote Sensing*, vol. 53, no. 4, pp. 1855–1864, 2015.

[257] M. Chi, A. Plaza, J. A. Benediktsson, Z. Sun, J. Shen, and Y. Zhu, "Big Data for Remote Sensing: Challenges and Opportunities," *Proceedings of the IEEE*, vol. 104, no. 11, pp. 2207–2219, 2016.

[258] T. W. Crowther, H. B. Glick, K. R. Covey, C. Bettigole, D. S. Maynard, S. M. Thomas, J. R. Smith, G. Hintler, M. C. Duguid, G. Amatulli, *et al.*, "Mapping tree density at a global scale," *Nature*, vol. 525, no. 7568, pp. 201–205, 2015.

[259] L. Eysn, M. Hollaus, E. Lindberg, F. Berger, J.-M. Monnet, M. Dalponte, M. Kobal, M. Pellegrini, E. Lingua, D. Mongus, and N. Pfeifer, "A Benchmark of Lidar-Based Single Tree Detection Methods Using Heterogeneous Forest Data from the Alpine Space," *Forests*, vol. 6, no. 5, pp. 1721–1747, 2015.

[260] C. A. Silva, A. T. Hudak, L. A. Vierling, E. L. Loudermilk, J. J. O'Brien, J. K. Hiers, S. B. Jack, C. Gonzalez-Benecke, H. Lee, M. J. Falkowski, and A. Khosravipour, "Imputation of Individual Longleaf Pine (*Pinus palustris* Mill.) Tree Attributes from Field and LiDAR Data," *Canadian Journal of Remote Sensing*, vol. 42, no. 5, pp. 554–573, 2016.

[261] M. Aubry-Kientz, R. Dutrieux, A. Ferraz, S. Saatchi, H. Hamraz, J. Williams, D. Coomes, A. Piboule, and G. Vincent, "A comparative assessment of the performance of individual tree crowns delineation algorithms from ALS data in tropical forests," *Remote Sensing*, vol. 11, no. 9, pp. 1–21, 2019.

[262] D. Comaniciu and P. Meer, "Mean shift: A robust approach toward feature space analysis," *IEEE Transactions on Pattern Analysis and Machine Intelligence*, vol. 24, no. 5, pp. 603–619, 2002.

[263] D. Comaniciu, "An algorithm for data-driven bandwidth selection," *IEEE Transactions on Pattern Analysis and Machine Intelligence*, vol. 25, no. 2, pp. 281–288, 2003.

[264] W. Xiao, S. Xu, S. O. Elberink, and G. Vosselman, "Individual Tree Crown Modeling and Change Detection from Airborne Lidar Data," *IEEE Journal of Selected Topics in Applied Earth Observations and Remote Sensing*, vol. 9, no. 8, pp. 3467–3477, 2016.

[265] A. Yilmaz, "Object Tracking by Asymmetric Kernel Mean Shift with Automatic Scale and Orientation Selection," in *2007 IEEE Conference on Computer Vision and Pattern Recognition*, (Minneapolis, US), pp. 1–6, June 2007.

[266] C. A. Silva, R. Valbuena, E. R. Pinagé, M. Mohan, D. R. A. de Almeida, E. North Broadbent, W. S. W. M. Jaafar, D. de Almeida Papa, A. Cardil, and C. Klauberg, "Forestgapr: An r package for forest gap analysis from canopy height models," *Methods in Ecology and Evolution*, vol. 10, no. 8, pp. 1347–1356, 2019.

[267] M. Dalponte, L. Frizzera, and D. Gianelle, "Individual tree crown delineation and tree species classification with hyperspectral and LiDAR data," *PeerJ*, vol. 6, p. e6227, 2019.

[268] C. B. Anderson, "The CCB-ID approach to tree species mapping with airborne imaging spectroscopy," *PeerJ*, vol. 6, p. e5666, 2018.

[269] E. Tusa, A. Reynolds, D. M. Lane, N. M. Robertson, H. Villegas, and A. Bosnjak, "Implementation of a fast coral detector using a supervised machine learning and gabor wavelet feature descriptors," in *2014 IEEE Sensor Systems for a Changing Ocean (SSCO).*, pp. 1–6, 2014.

[270] S. Brunton and J. Kutz, *Data-driven science and engineering: Machine learning, dynamical systems, and control*. Cambridge University Press, 2019.

[271] A. Laybros, M. Aubry-Kientz, J.-B. Féret, C. Bedeau, O. Brunaux, G. Derroire, and G. Vincent, "Quantitative airborne inventories in dense tropical forest using imaging spectroscopy," *Remote Sensing*, vol. 12, no. 10, p. 1577, 2020.

[272] C. A. Baldeck and G. P. Asner, "Improving remote species identification through efficient training data collection," *Remote Sensing*, vol. 6, no. 4, pp. 2682–2698, 2014.

[273] C. Albon, *Machine learning with python cookbook: Practical solutions from preprocessing to deep learning*. O'Reilly Media, Inc., 2018.

[274] L. Drumetz, J. Chanussot, and A. Iwasaki, "Endmembers as directional data for robust material variability retrieval in hyperspectral image unmixing," in *2018 IEEE International Conference on Acoustics, Speech and Signal Processing (ICASSP)*, pp. 3404–3408, 2018.

[275] T. Uezato, M. Fauvel, and N. Dobigeon, "Hyperspectral image unmixing with lidar data-aided spatial regularization," *IEEE Transactions on Geoscience and Remote Sensing*, vol. 56, no. 7, pp. 4098–4108, 2018.

[276] M. Malfante, *Automatic classification of natural signals for environmental monitoring*. Theses, Université Grenoble Alpes, Oct. 2018.

[277] A. Laybros, D. Schläpfer, J.-B. Féret, L. Descroix, C. Bedeau, M.-J. Lefevre, and G. Vincent, "Across date species detection using airborne imaging spectroscopy," *Remote Sensing*, vol. 11, no. 7, p. 789, 2019.

List of Figures

List of Tables

A

Thesis publications

This annex presents the list of paper publications derived from this PhD work.

A.1 Journal paper

Tusa, E., Monnet, J. M., Barré, J. B., Dalla Mura, M., Dalponte, M., Chanussot, J. (2020). Individual Tree Segmentation Based on Mean Shift and Crown Shape Model for Temperate Forest. *IEEE Geoscience and Remote Sensing Letters*.

A.2 Conference proceeding

Tusa, E., Monnet, J. M., Barré, ,J.B., M, D. M., Chanussot, J. (2020). Fusion Of Lidar And Hyperspectral Data For Semantic Segmentation Of Forest Tree Species. *Int. Arch. Photogramm. Remote Sens. Spatial Inf. Sci., XLIII-B3-2020, 487–494, 2020*. doi:http://dx.doi.org/10.5194/isprs-archives-XLIII-B3-2020-487-2020

A.3 Book chapter

TUSA, E., LAYBROS, A., MONNET, J. M., DALLA MURA, M., BARRÉ, J. B., VINCENT, G., DALPONTE, M., FÉRET, J. B. CHANUSSOT, J. (2020). FUSION OF HYPERSPECTRAL IMAGING AND LIDAR FOR FOREST MONITORING. IN *Data Handling in Science and Technology* (VOL. 32, PP. 281-303). ELSEVIER.

A.4 Poster presentations

- Tusa, E., Monnet, J.-M., Dalla Mura, M., Barré, J.-B., Dalponte, M. and Chanussot, J. 2018. Comparison of tree segmentation schemes based on LiDAR and hyperspectral data. In: SFPT-GH-2018 : 6ème colloque scientifique SFPT-Groupe Hyperspectral, Montpellier, France, 17-18 mai. handle: http://hdl.handle.net/10449/48795.
- Tusa, E., Laybros, A., Monnet, J.-M., Dalla Mura, M., Barré, J.-B.,Dalponte, M., Féret, J.-B., Vincent, G. and Chanussot, J. 2018. Fusion of hyperspectral images and Lidar data for forestry applications - a review. 9th Workshop on Hyperspectral Image and Signal Processing: Evolution in Remote Sensing, Amsterdam, The Netherlands, 23-26 Sept.
- Tusa, E., Monnet, J.-M., Dalla Mura, M., Barré, J.-B., Dalponte, M., and Chanussot, J. 2018. Delineación automática de árboles utilizando una nube de puntos 3D. Semana de la Ciencia UTMACH 2018 ISBN 978-9942-24-130-6. Machala, Ecuador, 6-9 nov. http://repositorio.utmachala.edu.ec/handle/48000/14197
- Tusa, E., Laybros, A., Barré, J.-B, Monnet, J.-M, Dalla Mura, M., Dalponte, M., Vincent, G., Chanussot, J., and Berger, F. 2019. Fusion of LiDAR and Hyperspectral Imaging for Forest Applications. Geophysical Research Abstracts. Vol. 21, EGU2019-17585, 2019. EGU General Assembly.

- Tusa, E., Barré, J.-B, Monnet, J.-M, Dalla Mura, M., Dalponte, M., Aussenac, R. and Chanussot, J.2019. "Forest stand 3D segmentation at the tree level from fused airborne LiDAR and Hyperspectral data" XXV IUFRO World Congress 2019, Curitiba, Brazil, 29 Sept-5 Oct. https://app.oxfordabstracts.com/events/691/program-app/submission/95581

- Tusa, E., Barré, J.-B, Monnet, J.-M, Dalla Mura, M., Berger, F. and Chanussot, J. 2019. Fusion of LiDAR and hyperspectral data for 3D segmentation of individual trees. In: SFPT-GH-2019 : 7ème colloque scientifique SFPT-Groupe Hyperspectral, Toulouse, France, 9-10 juillet.

- Tusa, E., Monnet, J.-M., Dalla Mura, M., Barré, J.-B., Berger, F. and Chanussot, J. 2019. Pixelwise classification using hyperspectral and lidar data for forest tree specie identification. 10th Workshop on Hyperspectral Image and Signal Processing: Evolution in Remote Sensing, Amsterdam, The Netherlands, 24-26 Sept.

B
Feature descriptors

This annex presents the equations for deriving vegetation indices (VI) and for computing LiDAR features, such as density, shape and statistical metrics.

B.1 Hyperspectral images

B.1.1 Vegetation indices

In this section, we detail the equations to compute the vegetation indices (VI) from hyperspectral data by organizing in 5 groups in the next tables: broadband greenness in Tables B.1 and B.2, narrowband greenness in Table B.3, light use efficiency in Table B.4, leaf pigments in Table B.5, dry or senescent carbon in Table B.6 and canopy water content in Table B.7. The reflectance values for the blue band ρ_{BLUE} is in the range 440 - 510 *nm* [53], for the green band ρ_{GREEN} is in 540 - 560 *nm* [54], for the red band ρ_{RED} is in 630 - 685 *nm* [53], for red-edge band ρ_{REDGE} is in 690 - 710 *nm* [54] and for near-infrared band ρ_{NIR} is in the range 760 - 850 *nm* [53]. For the reflectance band ρ_i, i represents the wavelength value in *nm* associated to this band.

B.2 LiDAR data

If we consider a 3D LiDAR point coordinate $\mathbf{x_i} = (X_i, Y_i, Z_i)$ and I_i is the intensity associated to $\mathbf{x_i}$, the following LiDAR features are computed at point-level and these are based on the work of Clément Dechesne et al. [165].

B.2.1 Density features

Two vegetation density features, D_1 and D_2 are computed by using three different cylindrical neighborhoods of $\mathbf{x_i}$. The first one is based on the number of local height maxima within the neighborhoods. The second one is related to the number of non-ground points within the neighborhoods. These features are calculated as follows:

$$D_{1,r_c} = \sum_{r_f \in \{1,2,3\}} Nt_{r_c,r_f} \tag{B.1}$$

$$D_{2,r_c} = \frac{Ns_{r_c}}{Ntot_{r_c}} \tag{B.2}$$

where Nt_{r_c,r_f} is the number of local maxima retrieved from a r_f maximum filter within the cylindrical neighborhood of radius $r_c \in \{1,2,3\}$. Ns_r is the number of points classified as ground points within the cylindrical neighborhood of radius r_c and $Ntot_{r_c}$ is the total number of points within the cylindrical neighborhood of radius r_c. D_1 describes how trees are close to each other and gives information about the tree crown width. D_2 provides information on the penetration rate of the LiDAR beam.

B.2.2 Shape featueres

The scatter S and the planarity P features are computed for every LiDAR point by following the equations:

$$S_{r_c} = \frac{\lambda_{3,r_c}}{\lambda_{1,r_c}} \tag{B.3}$$

$$P_{r_c} = 2 \times (\lambda_{2,r_c} - \lambda_{3,r_c}) \tag{B.4}$$

where $\lambda_{1,r_c} \geq \lambda_{2,r_c} \geq \lambda_{3,r_c}$ are the eigenvalues of the covariance matrix within the cylindrical neighborhood of $\mathbf{x_i}$ with radius $r_c \in \{1,2,3\}$, which are retrieved by applying PCA.

Table B.1: Equations for broadband greenness vegetation indices

No.	VI	Equation	Ref.
1	Normalized Difference Vegetation Index	$NDVI = \frac{\rho_{NIR}-\rho_{RED}}{\rho_{NIR}+\rho_{RED}}$	[69, 72–76]
2	Non-Linear Index	$NLI = \frac{\rho_{NIR}{}^2-\rho_{RED}}{\rho_{NIR}{}^2+\rho_{RED}}$	[184]
3	Renormalized Difference Vegetation Index	$RDVI = \frac{\rho_{NIR}-\rho_{RED}}{\sqrt{\rho_{NIR}+\rho_{RED}}}$	[158, 185]
4	Modified Non-Linear Index	$MNLI = \frac{(\rho_{NIR}{}^2-\rho_{RED})(1+L)}{\rho_{NIR}{}^2+\rho_{RED}+L}$, $L = 0.5$	[186]
5	Green Normalized Difference Vegetation Index	$GNDVI = \frac{\rho_{NIR}-\rho_{GREEN}}{\rho_{NIR}+\rho_{GREEN}}$	[69, 73, 76, 80, 187]
6	Green Leaf Index	$GLI = \frac{(\rho_{GREEN}-\rho_{RED})+(\rho_{GREEN}-\rho_{BLUE})}{2\rho_{GREEN}+\rho_{RED}+\rho_{BLUE}}$	[188]
7	Infrared Percentage Vegetation Index	$IPVI = \frac{\rho_{NIR}}{\rho_{NIR}+\rho_{RED}}$	[73, 76, 189]
8	Transformed Difference Vegetation Index	$TDVI = 1.5\frac{\rho_{NIR}-\rho_{RED}}{\sqrt{\rho_{NIR}{}^2+\rho_{RED}+0.5}}$	[190]
9	Triangular Greenness Index	$TGI = 0.5(\lambda_{RED}-\lambda_{BLUE})(\rho_{RED}-\rho_{GREEN}) - 0.5(\lambda_{RED}-\lambda_{GREEN})(\rho_{RED}-\rho_{BLUE})$	[191]
10	Difference Vegetation Index	$DVI = \rho_{NIR}-\rho_{RED}$	[73, 76, 192]
11	Green Difference Vegetation Index	$GDVI = \rho_{NIR}-\rho_{GREEN}$	[193]
12	Green Red Difference Index	$GRDI = \frac{\rho_{GREEN}-\rho_{RED}}{\rho_{GREEN}+\rho_{RED}}$	[192]
13	Difference Difference Vegetation Index	$DDVI = (2\rho_{948}-\rho_{751})-(\rho_{649}-\rho_{547})$	[76, 194]
14	Enhanced Vegetation Index 1	$EVI1 = 2.5\frac{\rho_{NIR}-\rho_{RED}}{\rho_{NIR}+6.0\rho_{RED}-7.5\rho_{BLUE}+1}$	[69, 73, 74, 76, 128, 195]
15	Enhanced Vegetation Index 2	$EVI2 = 2.5\frac{\rho_{NIR}-\rho_{RED}}{\rho_{NIR}+2.4\rho_{RED}+1}$	[76, 196]
16	Leaf Area Index	$LAI = 3.618EVI1-0.118$	[197]

Table B.2: Equations for broadband greenness vegetation indices

No.	VI	Equation	Ref.
17	Simple Ratio Vegetation Index 1	$SRVI1 = \frac{\rho_{NIR}}{\rho_{RED}}$	[69, 73–76, 126, 198]
18	Modified Simple Ratio	$MSR = \frac{\frac{\rho_{NIR}}{\rho_{RED}}-1}{\sqrt{\frac{\rho_{NIR}}{\rho_{RED}}+1}}$	[199]
19	Green Chlorophyll Index	$GCI = \frac{\rho_{NIR}}{\rho_{GREEN}} - 1$	[54, 67–69]
20	Green Ratio Vegetation Index	$GRVI = \frac{\rho_{NIR}}{\rho_{GREEN}}$	[200]
21	Green Red Ratio Vegetation Index	$GRRVI = \frac{\rho_{GREEN}}{\rho_{RED}}$	[76, 201]
22	Blue Ratio Vegetation Index	$BRVI = \frac{\rho_{RED}}{\rho_{BLUE}} \frac{\rho_{GREEN}}{\rho_{BLUE}} \frac{\rho_{REDGE}}{\rho_{BLUE}} \frac{\rho_{NIR}}{\rho_{BLUE}}$	[76, 201]
23	Red Ratio Vegetation Index	$RRVI = \frac{\rho_{NIR}}{\rho_{RED}} \frac{\rho_{GREEN}}{\rho_{RED}} \frac{\rho_{NIR}}{\rho_{REDGE}}$	[76, 201]
24	Sum Green Index	$SGI = \frac{1}{n}\sum_{i=1}^{n}\rho_i,\ \rho_i \in [500, 600]$	[69, 202]
25	Soil Adjusted Vegetation Index	$SAVI = (1+L)\frac{\rho_{NIR}-\rho_{RED}}{\rho_{NIR}+\rho_{RED}+L},\ L = 0.5$	[69, 74, 75, 203]
26	Optimized Soil Adjusted Vegetation Index	$OSAVI = (1+L)\frac{\rho_{NIR}-\rho_{RED}}{\rho_{NIR}+\rho_{RED}+L},\ L = 0.16$	[74, 204]
27	Modified Soil Adjusted Vegetation Index 2	$MSAVI2 = \rho_{NIR} + 0.5 - 0.5\sqrt{(2\rho_{NIR}+1)^2 - 8(\rho_{NIR}-\rho_{RED})}$	[74, 75, 158, 205]
28	Green Soil Adjusted Vegetation Index	$GSAVI = (1+L)\frac{\rho_{NIR}-\rho_{GREEN}}{\rho_{NIR}+\rho_{GREEN}+L},\ L = 0.5$	[193]
29	Green Optimized Soil Adjusted Vegetation Index	$GOSAVI = (1+L)\frac{\rho_{NIR}-\rho_{GREEN}}{\rho_{NIR}+\rho_{GREEN}+L},\ L = 0.16$	[193]
30	Green Atmospherically Resistant Index	$GARI = \frac{\rho_{NIR}-(\rho_{GREEN}-\gamma(\rho_{BLUE}-\rho_{RED}))}{\rho_{NIR}+(\rho_{GREEN}-\gamma(\rho_{BLUE}-\rho_{RED}))},\ \gamma = 1.7$	[76, 206]
31	Visible Atmospherically Resistant Index	$VARI = \frac{\rho_{GREEN}-\rho_{RED}}{\rho_{GREEN}+\rho_{RED}-\rho_{BLUE}}$	[76, 207]
32	Wide Dynamic Range Vegetation Index	$WDRVI = \frac{\alpha\rho_{NIR}-\rho_{RED}}{\alpha\rho_{NIR}+\rho_{RED}},\ \alpha = 0.2$	[208, 209]

Table B.3: Equations for narrowband greenness vegetation indices

No.	VI	Equation	Ref.
33	Modified Normalized Difference Vegetation Index	$MNDVI = \frac{\rho_{755}-\rho_{741}}{\rho_{755}+\rho_{741}}$	[74, 210]
34	Red Edge Normalized Difference Vegetation Index	$RENDVI = \frac{\rho_{NIR}-\rho_{REDGE}}{\rho_{NIR}+\rho_{REDGE}}$	[76, 80, 126, 211, 212]
35	Modified Red Edge Normalized Difference Vegetation Index	$MRENDVI = \frac{\rho_{NIR}-\rho_{REDGE}}{\rho_{NIR}+\rho_{REDGE}-2\rho_{445}}$	[69, 76, 212]
36	Simple Ratio Vegetation Index 2	$SRVI2 = \frac{\rho_{755}}{\rho_{712}}$	[74, 210]
37	Modified Red Edge Simple Ratio	$MRESR = \frac{\rho_{NIR}-\rho_{445}}{\rho_{REDGE}-\rho_{445}}$	[73, 76, 212, 213]
38	Red Edge Chlorophyll Index	$RECI = \frac{\rho_{NIR}}{\rho_{REDGE}} - 1$	[68, 69]
39	Vogelmann Red Edge Index 1	$VREI1 = \frac{\rho_{740}}{\rho_{720}}$	[73, 214]
40	Vogelmann Red Edge Index 2	$VREI2 = \frac{\rho_{734}-\rho_{747}}{\rho_{715}+\rho_{726}}$	[214]
41	Red Edge Inflection Point	$REIP = 700 + 40\left(\frac{\frac{\rho_{670}+\rho_{780}}{2}-\rho_{700}}{\rho_{741}-\rho_{700}}\right)$	[74, 126, 215]
42	Atmospherically Resistant Vegetation Index	$ARVI = \frac{\rho_{NIR}-(\rho_{RED}-(\rho_{BLUE}-\rho_{RED}))}{\rho_{NIR}+(\rho_{RED}-(\rho_{BLUE}-\rho_{RED}))}$	[73, 74, 76, 216]
43	Modified Chlorophyll Absorption Ratio Index 1	$MCARI1 = ((\rho_{700}-\rho_{670})-0.2(\rho_{700}-\rho_{550}))\frac{\rho_{700}}{\rho_{670}}$	[70]
44	Modified Chlorophyll Absorption Ratio Index 2	$MCARI2 = \frac{1.5(2.5(\rho_{800}-\rho_{670})-1.3(\rho_{800}-\rho_{550}))}{\sqrt{(2\rho_{800}+1)^2-(6\rho_{800}-5\sqrt{\rho_{670}})-0.5}}$	[71]
45	Transformed Chlorophyll Absorption Reflectance Index	$TCARI = 3((\rho_{700}-\rho_{670})-0.2(\rho_{700}-\rho_{550})\frac{\rho_{700}}{\rho_{670}})$	[69, 71]
46	Triangular Vegetation Index	$TVI = \frac{1}{2}(120(\rho_{750}-\rho_{550})-200(\rho_{670}-\rho_{550}))$	[217]
47	Modified Triangular Vegetation Index 1	$MTVI1 = 1.2(1.2(\rho_{800}-\rho_{550})-2.5(\rho_{670}-\rho_{550}))$	[71]
48	Modified Triangular Vegetation Index 2	$MTVI2 = \frac{1.5(1.2(\rho_{800}-\rho_{550})-2.5(\rho_{670}-\rho_{550}))}{\sqrt{(2\rho_{800}+1)^2-(6\rho_{800}-5\sqrt{\rho_{670}})-0.5}}$	[71, 158]

Table B.4: Equations for light use efficiency vegetation indices

No.	VI	Equation	Ref.
49	Photochemical Reflectance Index	$PRI = \frac{\rho_{531}-\rho_{570}}{\rho_{531}+\rho_{570}}$	[69, 76, 126, 218, 219]
50	Structure Insensitive Pigment Index	$SIPI = \frac{\rho_{800}-\rho_{445}}{\rho_{800}-\rho_{680}}$	[69, 73, 220]
51	Red Green Ratio Index	$RGRI = \frac{\frac{1}{n}\sum_i^n \rho_i}{\frac{1}{m}\sum_j^m \rho_j}$, $\rho_i \in [600, 700)$, $\rho_j \in [500, 600)$	[69, 221]
52	Photochemical Reflectance Ratio	$PRR = \frac{\rho_{531}}{\rho_{570}}$	[69, 222]

Table B.5: Equations for leaf pigments vegetation indices

No.	VI	Equation	Ref.
53	Anthocyanin Reflectance Index 1	$ARI1 = \frac{1}{\rho_{GREEN}} - \frac{1}{\rho_{REDGE}}$	[69, 73, 81]
54	Anthocyanin Reflectance Index 2	$ARI2 = \left(\frac{1}{\rho_{GREEN}} - \frac{1}{\rho_{REDGE}}\right)\rho_{NIR}$	[69, 73, 81]
55	Carotenoid Reflectance Index 1	$CRI1 = \frac{1}{\rho_{510}} - \frac{1}{\rho_{GREEN}}$	[69, 73, 82]
56	Carotenoid Reflectance Index 2	$CRI2 = \frac{1}{\rho_{510}} - \frac{1}{\rho_{REDGE}}$	[69, 73, 82]
57	Carotenoid Reflectance Index 3	$CRI3 = \left(\frac{1}{\rho_{510}} - \frac{1}{\rho_{GREEN}}\right)\rho_{NIR}$	[68]
58	Carotenoid Reflectance Index 4	$CRI4 = \left(\frac{1}{\rho_{510}} - \frac{1}{\rho_{REDGE}}\right)\rho_{NIR}$	[54, 68]
59	Plant Pigment Ratio	$PPR = \frac{\rho_{550}-\rho_{450}}{\rho_{550}+\rho_{450}}$	[69, 83]

Table B.6: Equations for dry or senescent carbon vegetation indices

No.	VI	Equation	Ref.
60	Plant Senescence Reflectance Index	$PSRI = \frac{\rho_{680}-\rho_{550}}{\rho_{750}}$	[73, 76, 223]

Table B.7: Equations for canopy water content vegetation indices

No.	VI	Equation	Ref.
61	Water Band Index	$WBI = \frac{\rho_{970}}{\rho_{900}}$	[73, 84]

B.2.3 Statistical features

Let $\mathbf{x_j} = (X_j, Y_j, Z_j)$ the 3D coordinate and I_j the intensity of all the points within the cylindrical neighborhood of radius r_c of point $\mathbf{x_i}$, where $j = 1, ..., m_c$, we can define $\{\mathbf{x_j}\}_{j=1}^{m_c}$ as the set of neighbors of $\mathbf{x_i}$. Then, the following list of statistical features is described in Table B.8 [276].

No.	Metric	Equation
1	Minimum	$min_Z = min_j(\{Z_j\}_{j=1}^{m_c})$
2	Maximum	$max_Z = max_j(\{Z_j\}_{j=1}^{m_c})$
3	Mean of intensity	$\bar{I} = \frac{\sum_{j=1}^{m_c} I_j}{m_c}$
4	Mean of height	$mean_Z(\{Z_j\}_{j=1}^{m_c}) = \frac{\sum_{j=1}^{m_c} Z_j}{m_c}$ $\bar{Z} = mean_Z(\{Z_j\}_{j=1}^{m_c})$
5	Median	$med_Z(\{Z_j\}_{j=1}^{m_c}) = \frac{1}{2}\left(Z_{\lfloor (m_c+1)/2 \rfloor} + Z_{\lceil (m_c+1)/2 \rceil}\right)$ $\tilde{Z} = med_Z(\{Z_j\}_{j=1}^{m_c})$
6	Standard deviation	$s_Z = \sqrt{\frac{1}{m_c}\sum_{j=1}^{m_c}(Z_j - \mu_Z)^2}$
7	Median absolute deviation from median	$Medmed_Z = med_Z(\{\lvert Z_j - \tilde{Z}\rvert\}_{j=1}^{m_c})$
8	Mean absolute deviation from median	$Meanmed_Z = mean_Z(\{\lvert Z_j - \tilde{Z}\rvert\}_{j=1}^{m_c})$
9	Skewness	$S_Z = \frac{1}{m_c}\sum_{j=1}^{m_c}\left(\frac{Z_j - \bar{Z}}{s_Z}\right)^3$
10	Kurtosis	$K_Z = \frac{1}{m_c}\sum_{j=1}^{m_c}\left(\frac{Z_j - \bar{Z}}{s_Z}\right)^4$

Table B.8: Statistical features

where $\lfloor . \rfloor$ $\lceil . \rceil$ denote the floor and ceiling functions, respectively. In addition to these metrics, the 10^{th}, 20^{th}, 30^{th}, 40^{th}, 50^{th}, 60^{th}, 70^{th}, 80^{th}, 90^{th} and 95^{th} percentiles were computed for the heights Z_j of the points in the neighborhood of $\mathbf{x_i}$.

C

ITC Delineation results

In this annex, we present the results of the 3D segmentation in the 22 forest plots. Histograms of heights for the true positive (TP), false negative (FN) and false positive (FP) trees are presented for the 7 plots from the Chamrousse site and the 15 plots from Pellizzano site. Besides, the field-LiDAR height and crown radius scatterplots are presented for every plot.

C.1 Tree matching

In this section, we show the results of the 3D segmentation by applying the 3D Adaptive Mean Shift (AMS3D) algorithm with ellipsoid crown shape model and superellipsoid kernel profile. The ITC segmentation is shown in (a), the matched trees or true positive (TP) detections distribution in the DSM is shown (b), and the false negative (FN) detections are presented in (c).

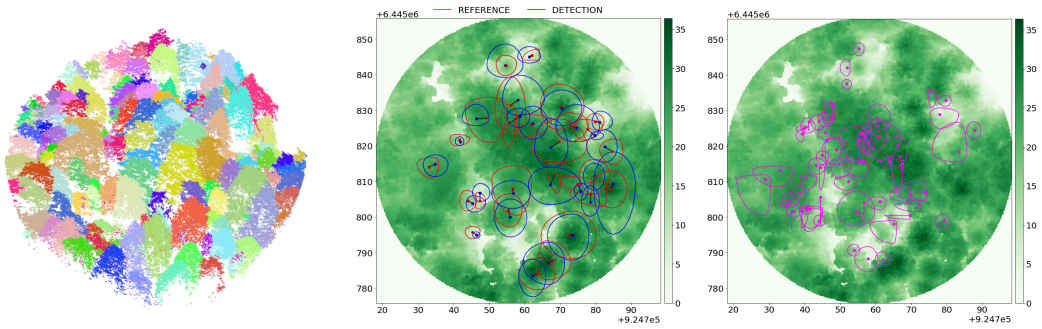

(a) Chamrousse - PC1 (b) PC1: 27 TP out of 92 trees. (c) PC1: 65 FN out of 92 trees.

Figure C.1: Plot 1 from Chamrousse site: (a) 3D segmentation output, (b) Matched trees or true positive (TP) detection distribution and (c) false negative (FN) detections.

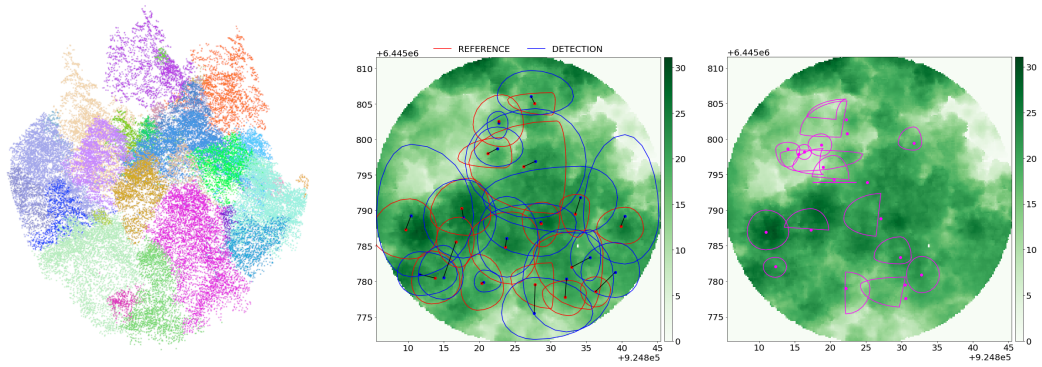

(a) Chamrousse - PC1b (b) PC1b: 17 TP out of 36 trees. (c) PC1b: 19 FN out of 36 trees.

Figure C.2: Plot 1b from Chamrousse site: (a) 3D segmentation output, (b) Matched trees or true positive (TP) detection distribution and (c) false negative (FN) detections.

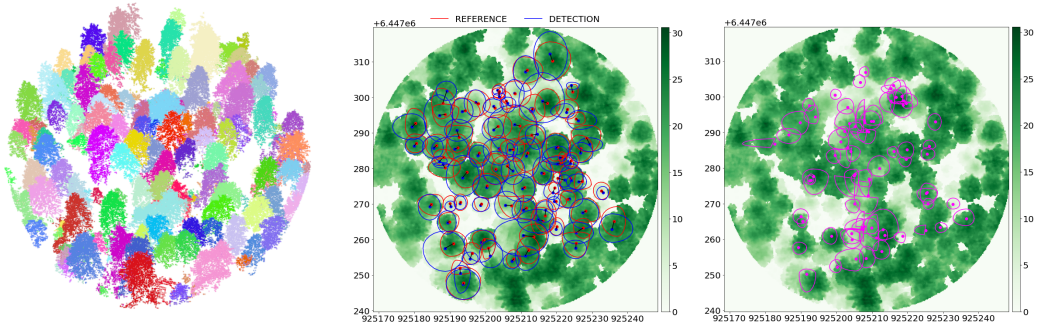

(a) Chamrousse - PC2 (b) PC2: 72 TP out of 144 trees. (c) PC2: 72 FN out of 144 trees.

Figure C.3: Plot 2 from Chamrousse site: (a) 3D segmentation output, (b) Matched trees or true positive (TP) detection distribution and (c) false negative (FN) detections.

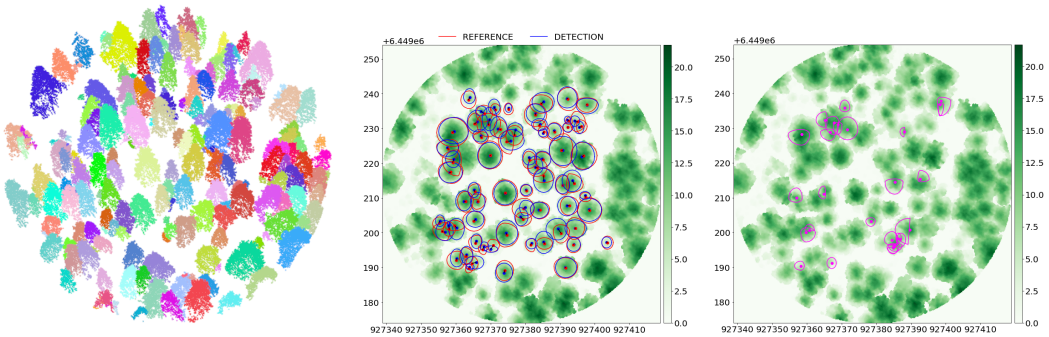

(a) Chamrousse - PC3 (b) PC3: 66 TP out of 92 trees. (c) PC3: 26 FN out of 92 trees.

Figure C.4: Plot 3 from Chamrousse site: (a) 3D segmentation output, (b) Matched trees or true positive (TP) detection distribution and (c) false negative (FN) detections.

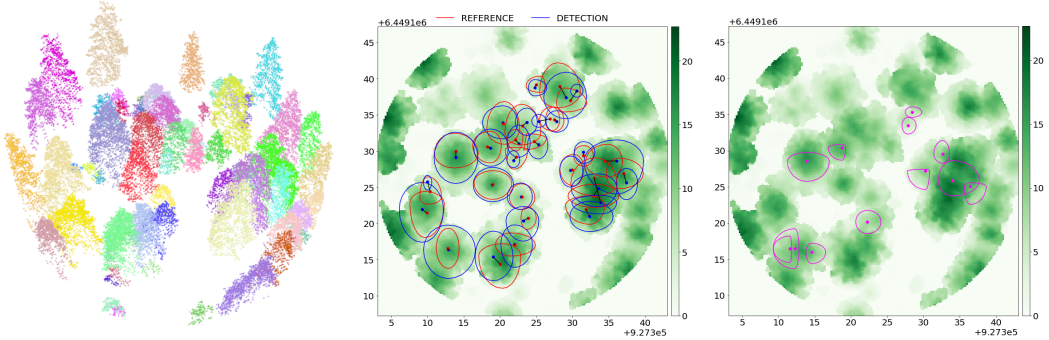

(a) Chamrousse - PC3b (b) PC3b: 27 TP out of 39 trees. (c) PC3b: 12 FN out of 39 trees.

Figure C.5: Plot 3b from Chamrousse site: (a) 3D segmentation output, (b) Matched trees or true positive (TP) detection distribution and (c) false negative (FN) detections.

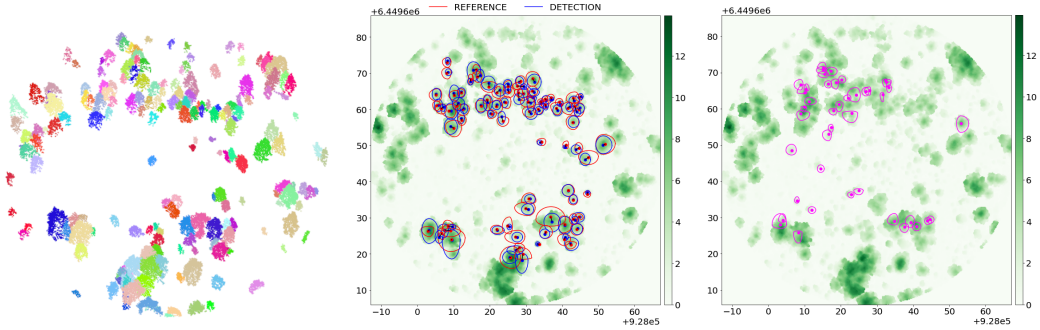

(a) Chamrousse - PC4 (b) PC4: 77 TP out of 119 trees. (c) PC4: 42 FN out of 119 trees.

Figure C.6: Plot 4 from Chamrousse site: (a) 3D segmentation output, (b) Matched trees or true positive (TP) detection distribution and (c) false negative (FN) detections.

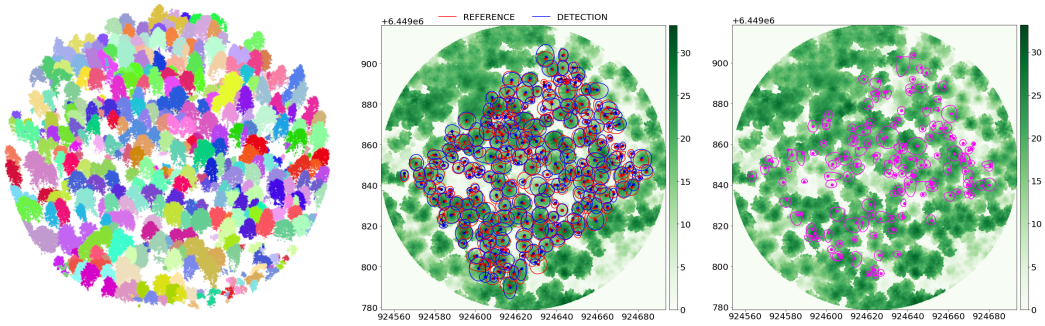

(a) Chamrousse - PCPremol (b) PCPremol: 220 TP out of 372 trees. (c) PCPremol: 152 FN out of 372 trees.

Figure C.7: Plot Premol from Chamrousse site: (a) 3D segmentation output, (b) Matched trees or true positive (TP) detection distribution and (c) false negative (FN) detections.

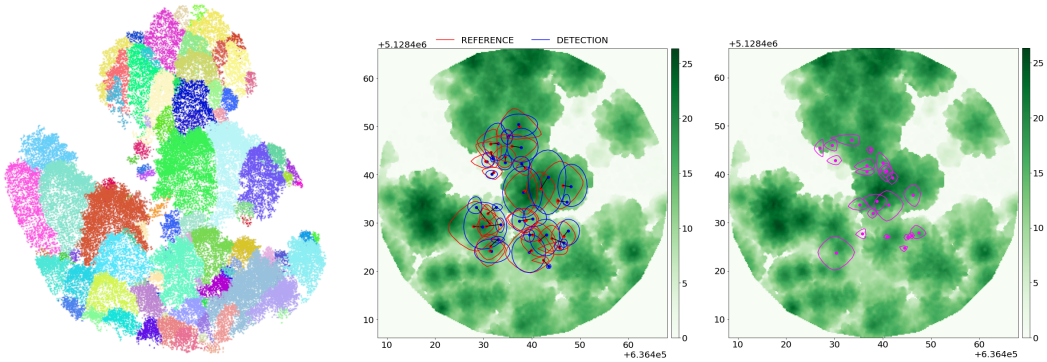

(a) Pellizzano - PP1 (b) PP1: 28 TP out of 51 trees. (c) PP1: 23 FN out of 51 trees.

Figure C.8: Plot 1 from Pellizzano site: (a) 3D segmentation output, (b) Matched trees or true positive (TP) detection distribution and (c) false negative (FN) detections.

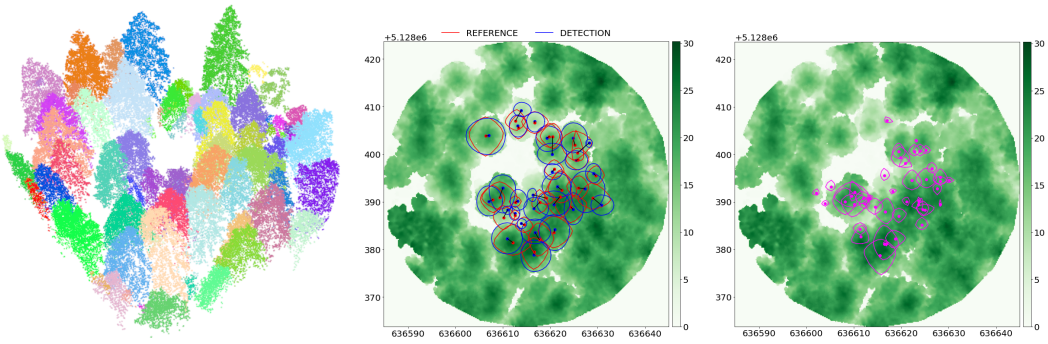

(a) Pellizzano - PP2 (b) PP2: 28 TP out of 71 trees. (c) PP2: 43 FN out of 71 trees.

Figure C.9: Plot 2 from Pellizzano site: (a) 3D segmentation output, (b) Matched trees or true positive (TP) detection distribution and (c) false negative (FN) detections.

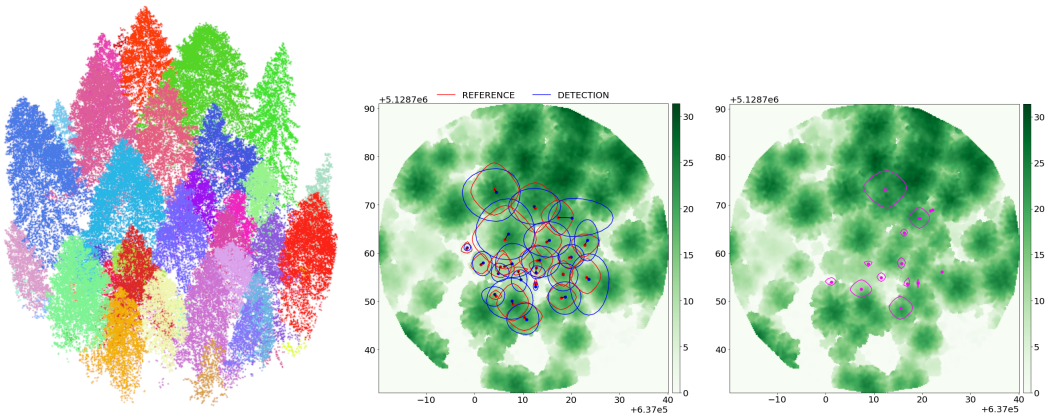

(a) Pellizzano - PP3 (b) PP3: 21 TP out of 35 trees. (c) PP3: 14 FN out of 35 trees.

Figure C.10: Plot 3 from Pellizzano site: (a) 3D segmentation output, (b) Matched trees or true positive (TP) detection distribution and (c) false negative (FN) detections.

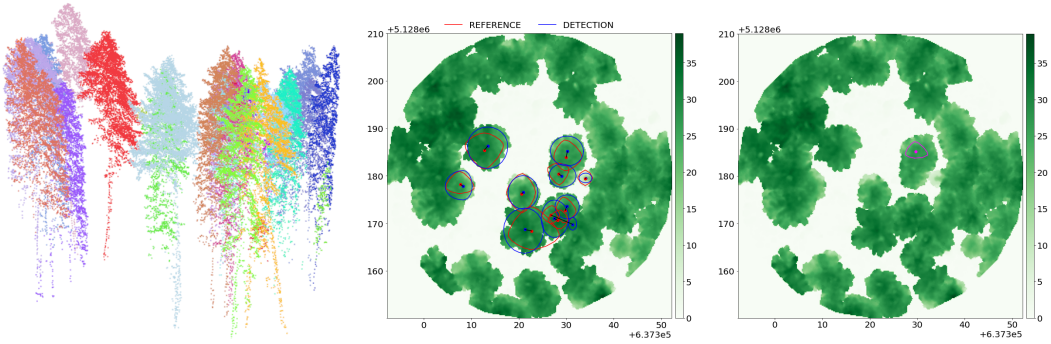

(a) Pellizzano - PP4 (b) PP4: 10 TP out of 11 trees. (c) PP4: 1 FN out of 11 trees.

Figure C.11: Plot 4 from Pellizzano site: (a) 3D segmentation output, (b) Matched trees or true positive (TP) detection distribution and (c) false negative (FN) detections.

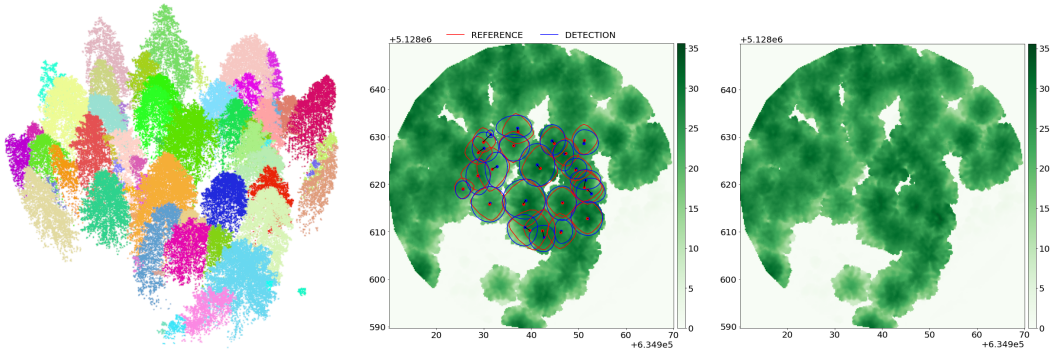

(a) Pellizzano - PP5 (b) PP4: 21 TP out of 21 trees. (c) PP4: 0 FN out of 21 trees.

Figure C.12: Plot 5 from Pellizzano site: (a) 3D segmentation output, (b) Matched trees or true positive (TP) detection distribution and (c) false negative (FN) detections.

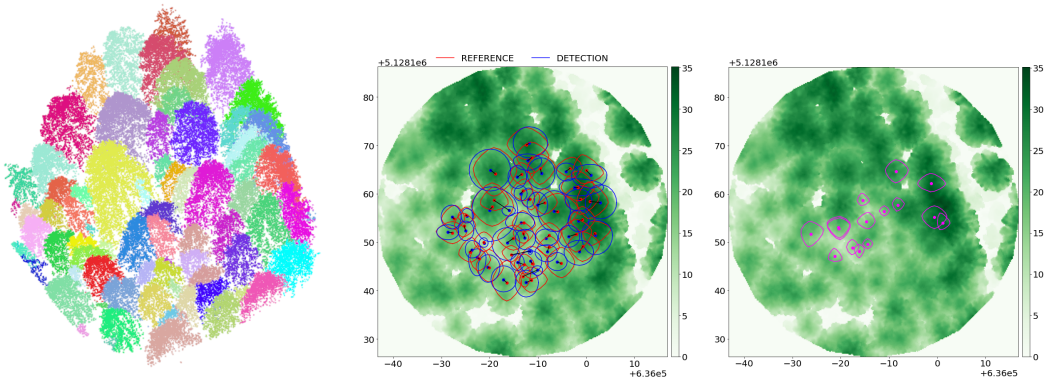

(a) Pellizzano - PP6 (b) PP6: 40 TP out of 55 trees. (c) PP6: 15 FN out of 55 trees.

Figure C.13: Plot 6 from Pellizzano site: (a) 3D segmentation output, (b) Matched trees or true positive (TP) detection distribution and (c) false negative (FN) detections.

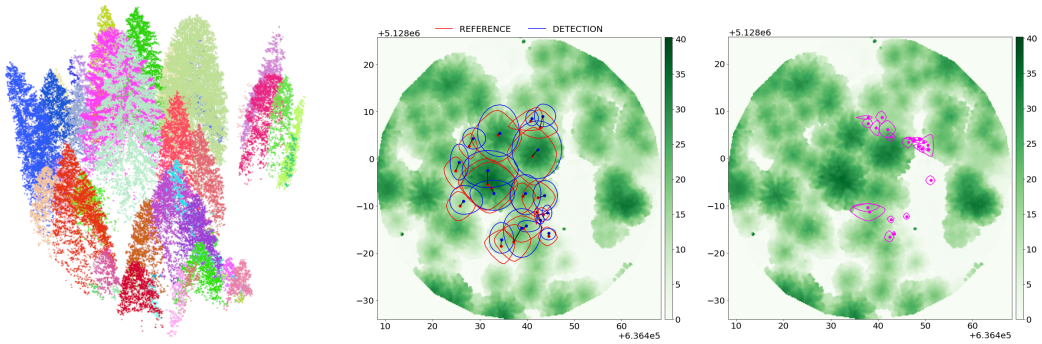

(a) Pellizzano - PP7 (b) PP7: 17 TP out of 39 trees. (c) PP7: 22 FN out of 39 trees.

Figure C.14: Plot 7 from Pellizzano site: (a) 3D segmentation output, (b) Matched trees or true positive (TP) detection distribution and (c) false negative (FN) detections.

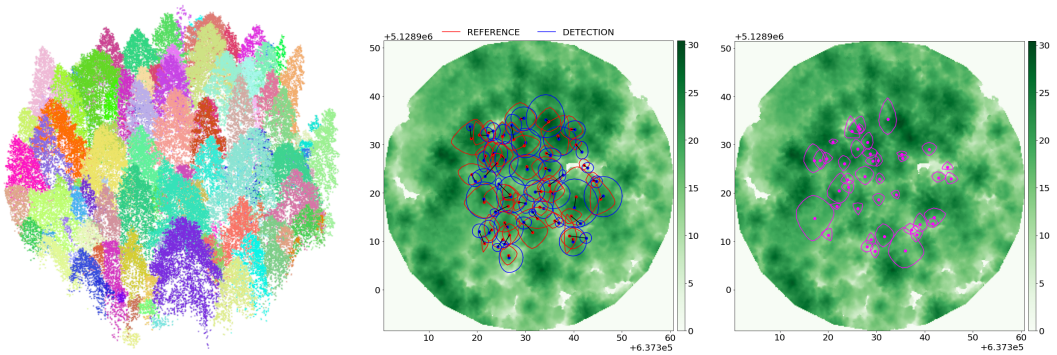

(a) Pellizzano - PP8 (b) PP8: 44 TP out of 85 trees. (c) PP8: 41 FN out of 85 trees.

Figure C.15: Plot 8 from Pellizzano site: (a) 3D segmentation output, (b) Matched trees or true positive (TP) detection distribution and (c) false negative (FN) detections.

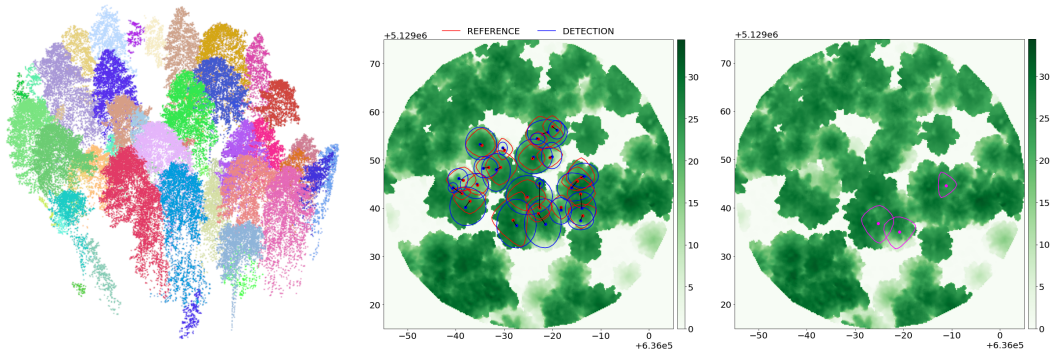

(a) Pellizzano - PP9 (b) PP9: 22 TP out of 25 trees. (c) PP9: 3 FN out of 25 trees.

Figure C.16: Plot 9 from Pellizzano site: (a) 3D segmentation output, (b) Matched trees or true positive (TP) detection distribution and (c) false negative (FN) detections.

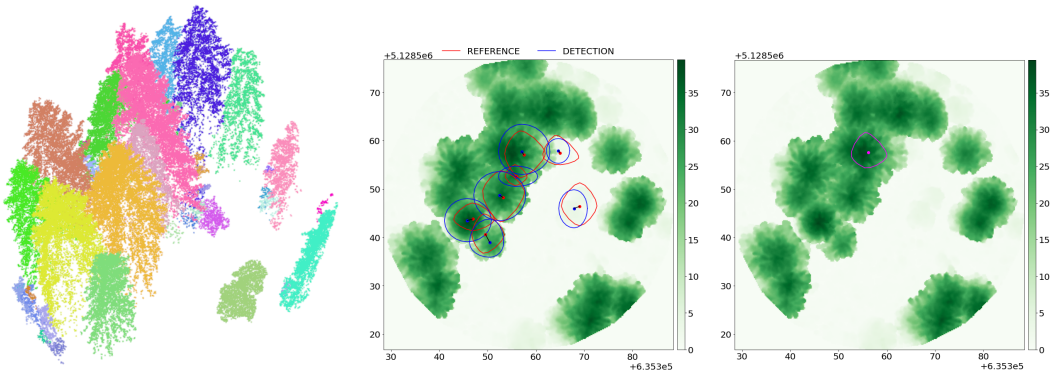

(a) Pellizzano - PP10 (b) PP10: 7 TP out of 8 trees. (c) PP10: 1 FN out of 8 trees.

Figure C.17: Plot 10 from Pellizzano site: (a) 3D segmentation output, (b) Matched trees or true positive (TP) detection distribution and (c) false negative (FN) detections.

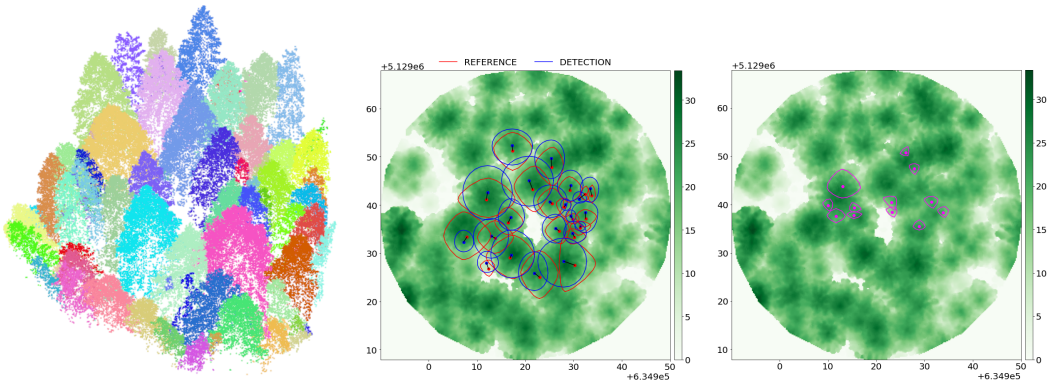

(a) Pellizzano - PP11 (b) PP11: 21 TP out of 33 trees. (c) PP11: 12 FN out of 33 trees.

Figure C.18: Plot 11 from Pellizzano site: (a) 3D segmentation output, (b) Matched trees or true positive (TP) detection distribution and (c) false negative (FN) detections.

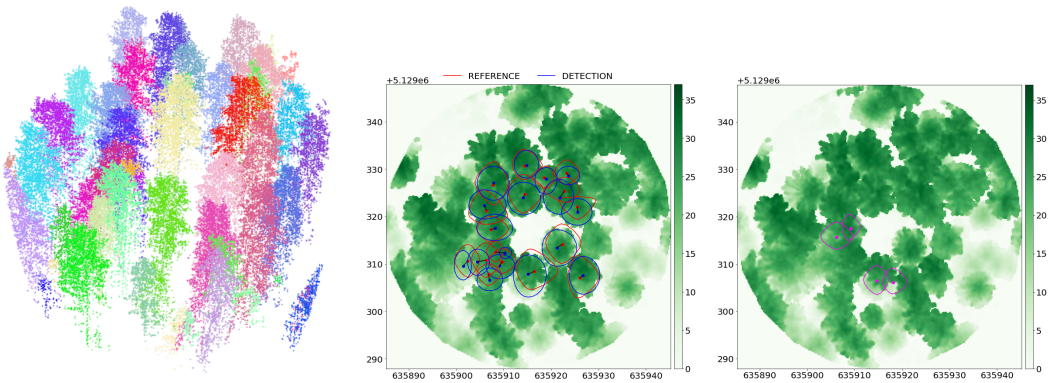

(a) Pellizzano - PP12 (b) PP12: 17 TP out of 21 trees. (c) PP12: 4 FN out of 21 trees.

Figure C.19: Plot 12 from Pellizzano site: (a) 3D segmentation output, (b) Matched trees or true positive (TP) detection distribution and (c) false negative (FN) detections.

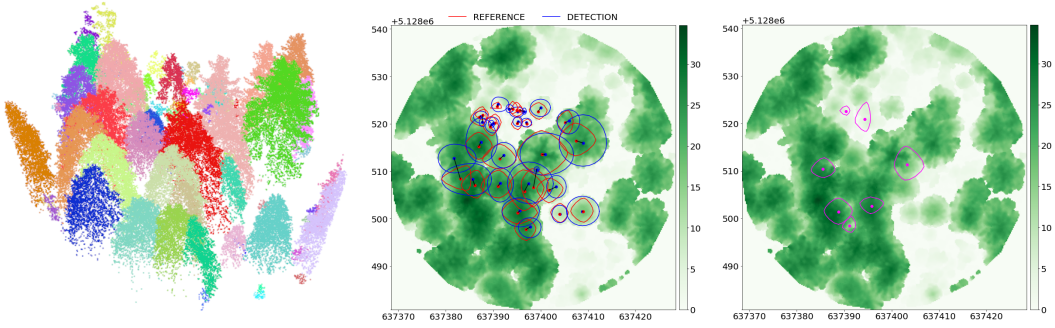

(a) Pellizzano - PP13 (b) PP13: 26 TP out of 33 trees. (c) PP13: 7 FN out of 33 trees.

Figure C.20: Plot 13 from Pellizzano site: (a) 3D segmentation output, (b) Matched trees or true positive (TP) detection distribution and (c) false negative (FN) detections.

(a) Pellizzano - PP14

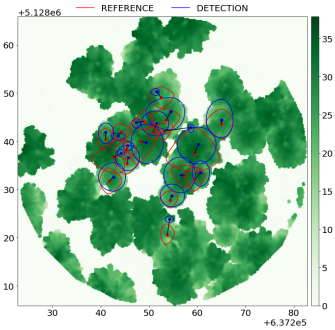

(b) PP14: 18 TP out of 20 trees.

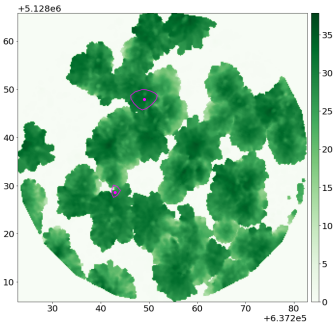

(c) PP14: 2 FN out of 20 trees.

Figure C.21: Plot 14 from Pellizzano site: (a) 3D segmentation output, (b) Matched trees or true positive (TP) detection distribution and (c) false negative (FN) detections.

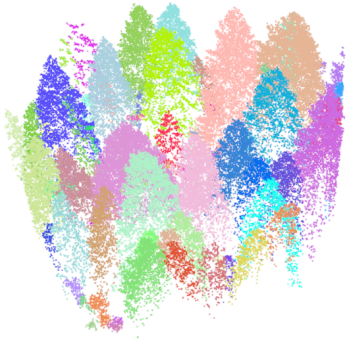

(a) Pellizzano - PP15

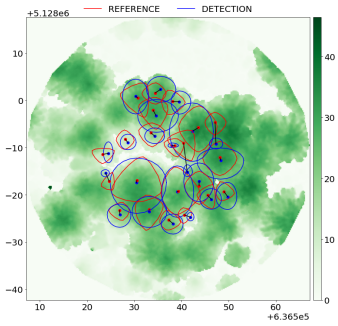

(b) PP15: 22 TP out of 35 trees.

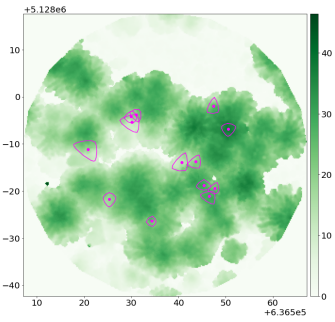

(c) PP15: 13 FN out of 35 trees.

Figure C.22: Plot 15 from Pellizzano site: (a) 3D segmentation output, (b) Matched trees or true positive (TP) detection distribution and (c) false negative (FN) detections.

C.2 Height histograms

Table C.23 presents the results of height histograms for tree detection in the Chamrousse site. The gap area percentage (GAP) is estimated from the rate between the gap area given by a height threshold every 1 *m* and the maximum gap area surface (approximately the forest plot surface) calculated in an R package *ForestGapR* [266]. Tables C.24 and C.25 present the results of height histograms for tree detection in the Pellizzano site.

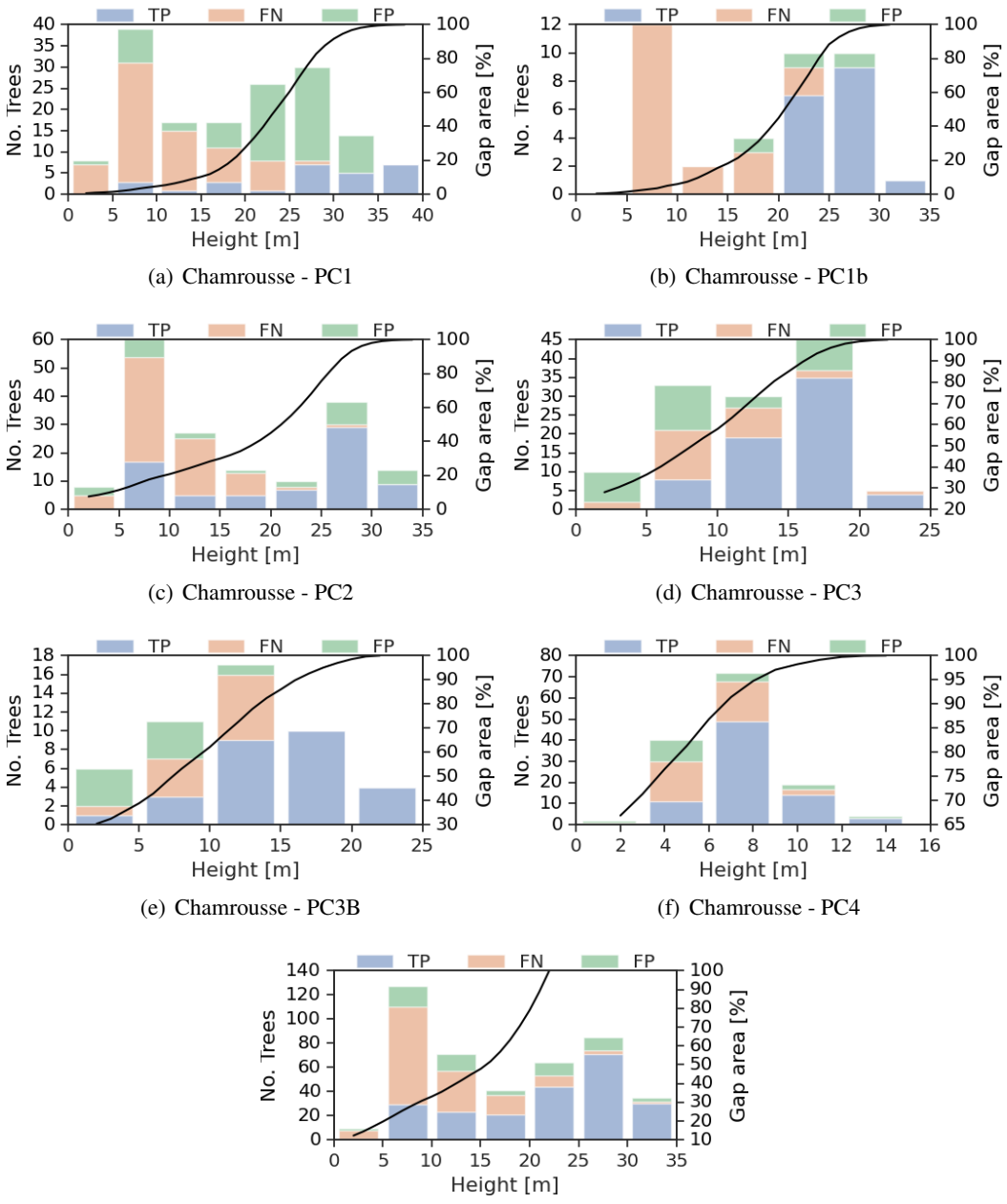

(a) Chamrousse - PC1

(b) Chamrousse - PC1b

(c) Chamrousse - PC2

(d) Chamrousse - PC3

(e) Chamrousse - PC3B

(f) Chamrousse - PC4

(g) Chamrousse - PCPremol

Figure C.23: Histograms of heights for the true positive (TP), false negative (FN) and false positive (FP) trees in the Chamrousse site. The GAP curve is represented in black.

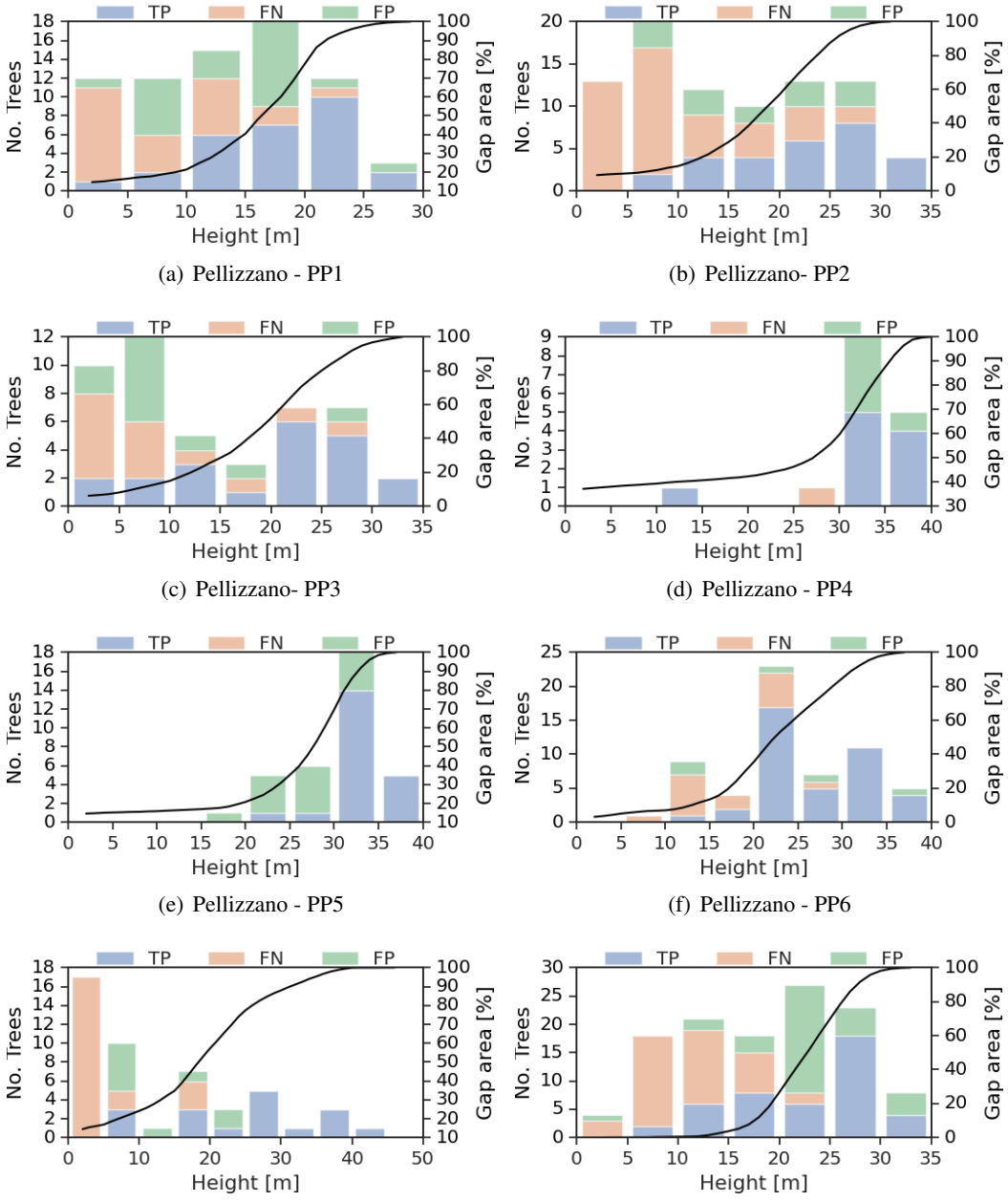

(a) Pellizzano - PP1

(b) Pellizzano- PP2

(c) Pellizzano- PP3

(d) Pellizzano - PP4

(e) Pellizzano - PP5

(f) Pellizzano - PP6

(g) Pellizzano - PP7

(h) Pellizzano - PP8

Figure C.24: Histograms of heights for the true positive (TP), false negative (FN) and false positive (FP) trees in the Pellizzano site. The GAP curve is represented in black.

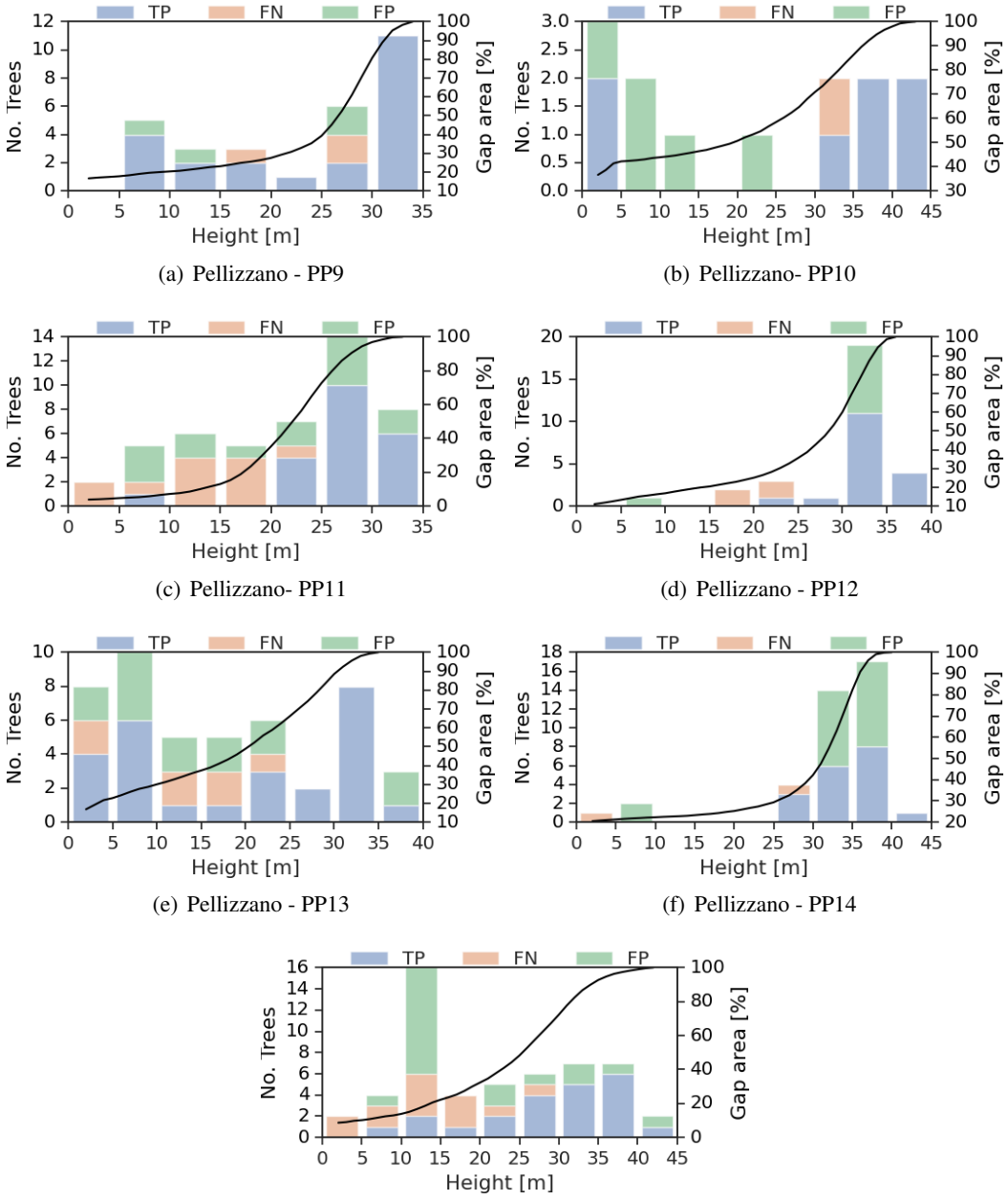

(a) Pellizzano - PP9

(b) Pellizzano- PP10

(c) Pellizzano- PP11

(d) Pellizzano - PP12

(e) Pellizzano - PP13

(f) Pellizzano - PP14

(g) Pellizzano - PP15

Figure C.25: Histograms of heights for the true positive (TP), false negative (FN) and false positive (FP) trees in the Pellizzano site. The GAP curve is represented in black.

C.3 Field-LiDAR height scatterplots

Field measured height of correctly detected trees plotted against LiDAR height for the Chamrousse site is presented in Figure C.26 and for the Pellizzano site is in Figures C.27 and C.28.

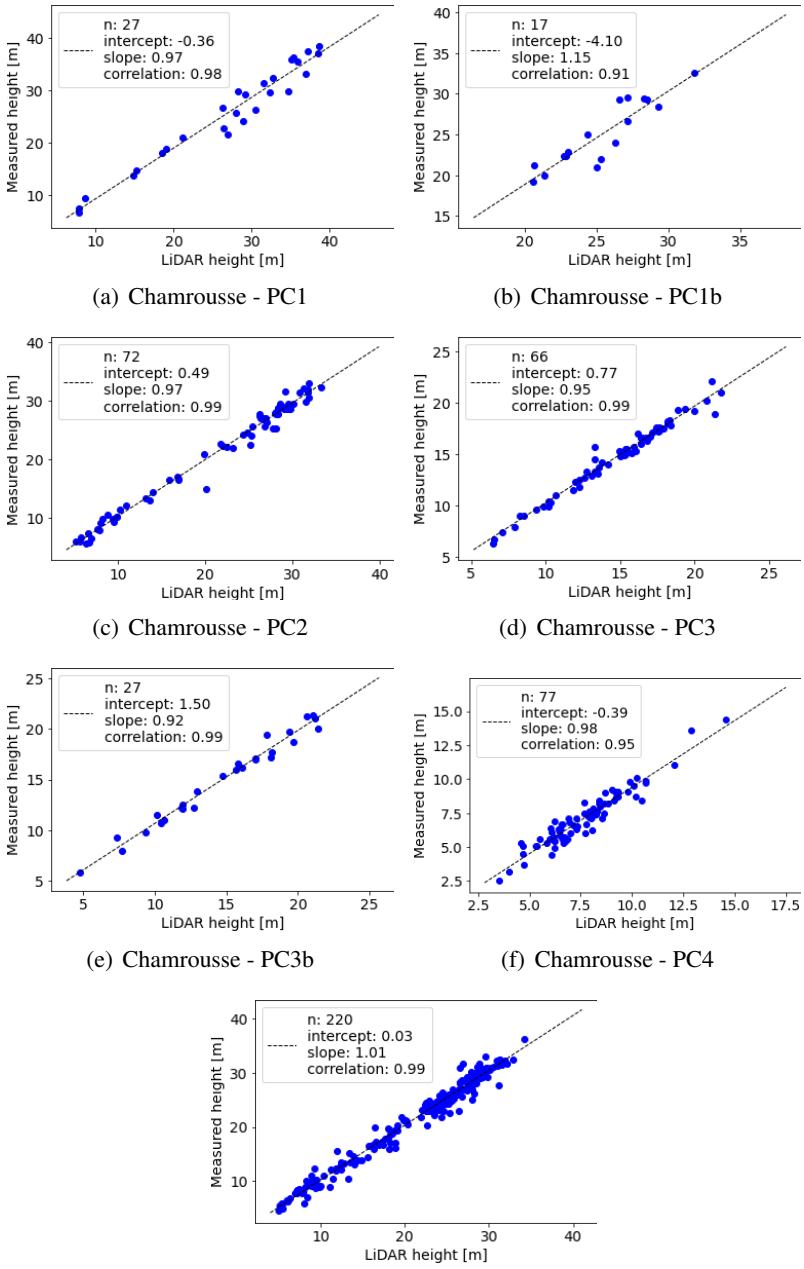

(a) Chamrousse - PC1

(b) Chamrousse - PC1b

(c) Chamrousse - PC2

(d) Chamrousse - PC3

(e) Chamrousse - PC3b

(f) Chamrousse - PC4

(g) Chamrousse - PCPremol

Figure C.26: Field measured height of correctly detected trees plotted against LiDAR height. Regression model is indicated with the corresponding adj-R^2 and the number of detected trees.

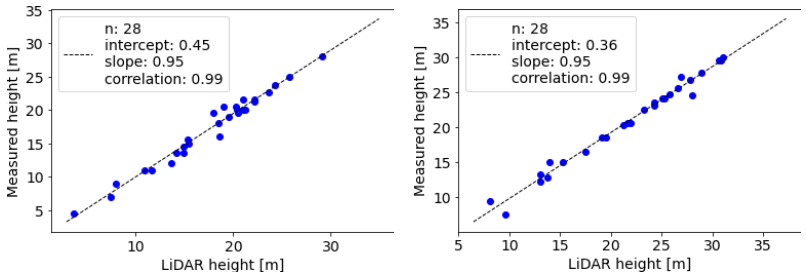

(a) Pellizzano - PP1

(b) Pellizzano - PP2

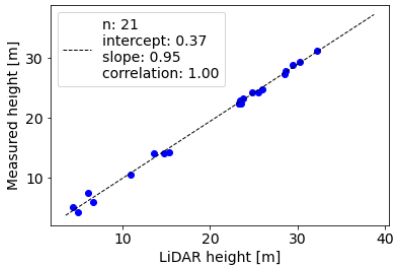

(c) Pellizzano - PP3

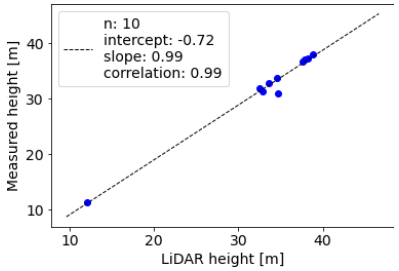

(d) Pellizzano - PP4

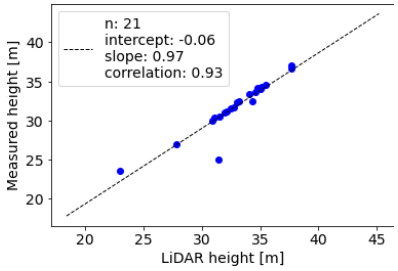

(e) Pellizzano - PP5

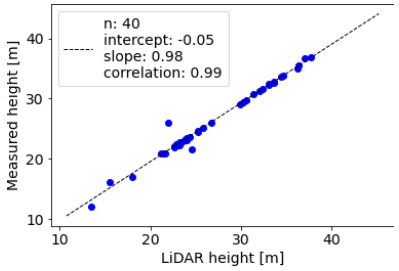

(f) Pellizzano - PP6

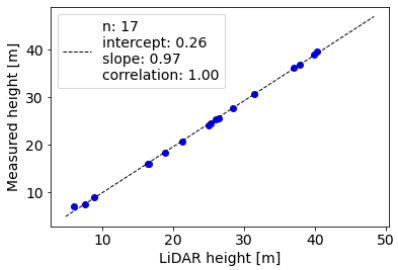

(g) Pellizzano - PP7

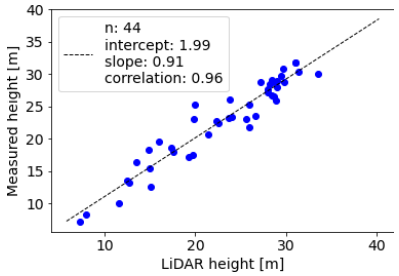

(h) Pellizzano - PP8

Figure C.27: Field measured height of correctly detected trees plotted against LiDAR height. Regression model is indicated with the corresponding adj-R^2 and the number of detected trees.

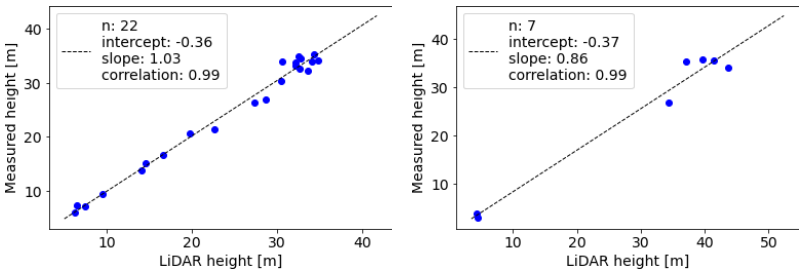

(a) Pellizzano - PP9

(b) Pellizzano - PP10

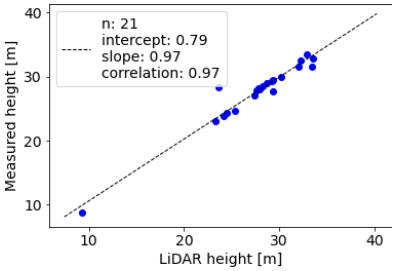

(c) Pellizzano - PP11

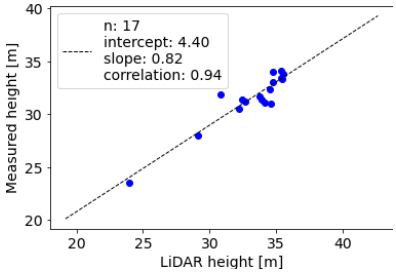

(d) Pellizzano - PP12

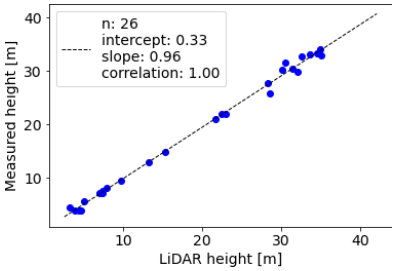

(e) Pellizzano - PP13

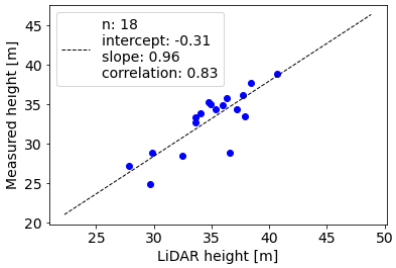

(f) Pellizzano - PP14

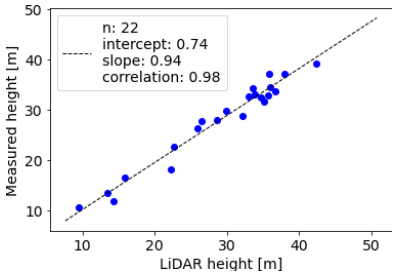

(g) Pellizzano - PP15

Figure C.28: Field measured height of correctly detected trees plotted against LiDAR height. Regression model is indicated with the corresponding adj-R^2 and the number of detected trees.

C.4 Field-LiDAR crown radius scatterplots

Field measured crown radius of correctly detected trees vs LiDAR crown radius for the Chamrousse site is presented in Figure C.29 and for the Pellizzano site is in Figures C.30 and C.31.

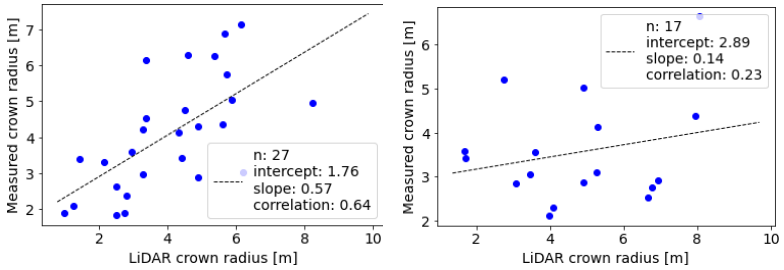

(a) Chamrousse - PC1

(b) Chamrousse - PC1b

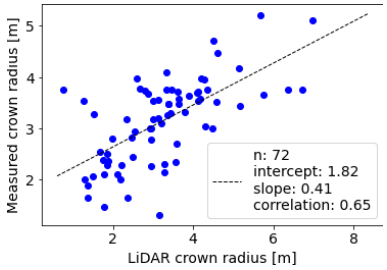

(c) Chamrousse - PC2

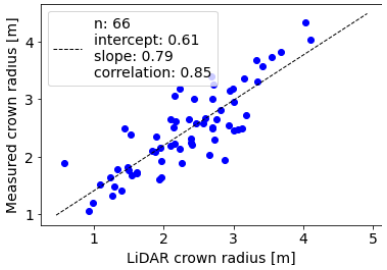

(d) Chamrousse - PC3

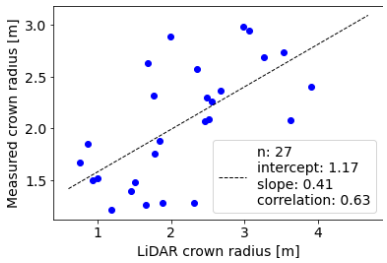

(e) Chamrousse - PC3b

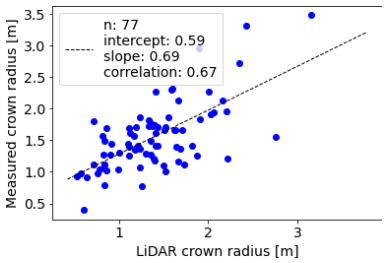

(f) Chamrousse - PC4

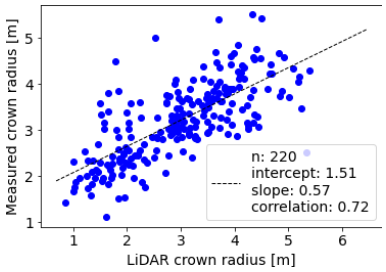

(g) Chamrousse - PCPremol

Figure C.29: Field measured crown radius of correctly detected trees plotted against LiDAR crown radius. Regression model is indicated with the corresponding adj-R^2 and the number of detected trees.

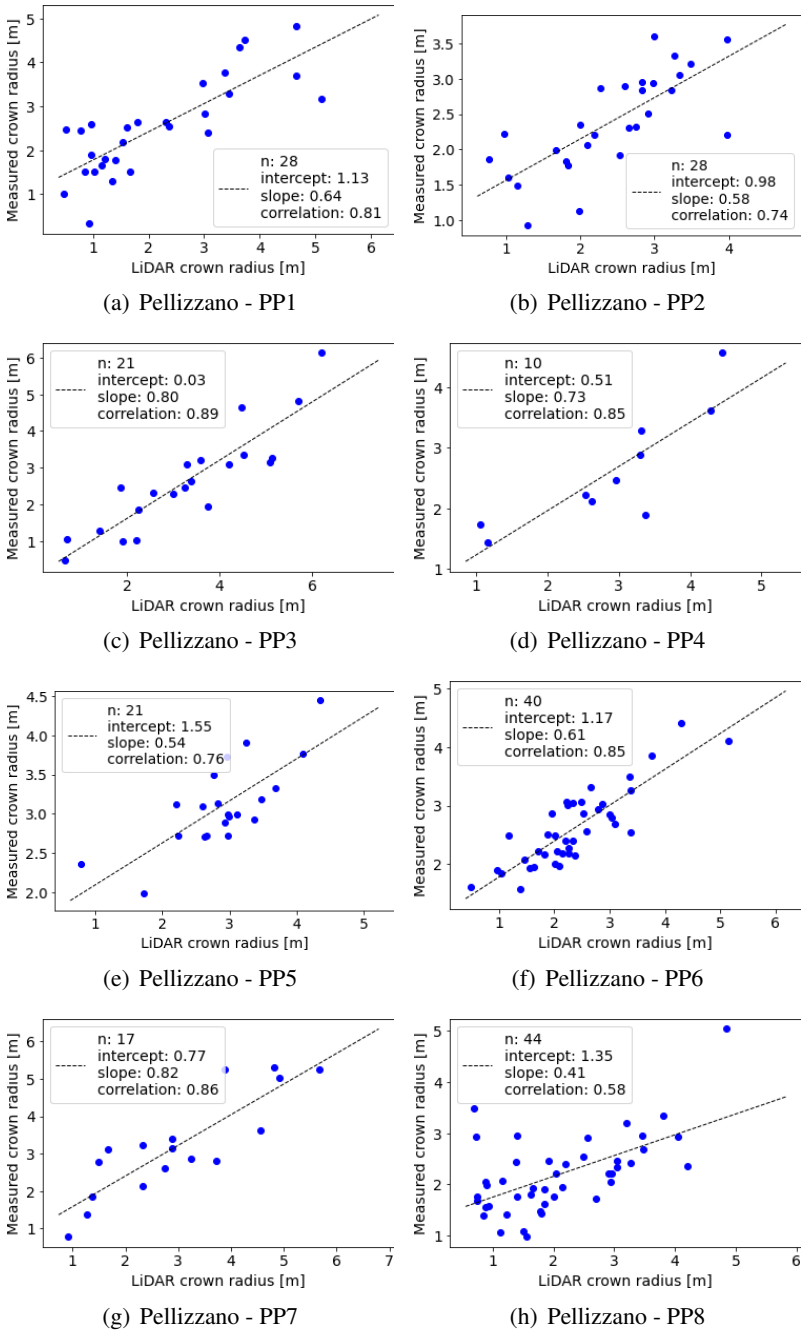

(a) Pellizzano - PP1 (b) Pellizzano - PP2

(c) Pellizzano - PP3 (d) Pellizzano - PP4

(e) Pellizzano - PP5 (f) Pellizzano - PP6

(g) Pellizzano - PP7 (h) Pellizzano - PP8

Figure C.30: Field measured crown radius of correctly detected trees plotted against LiDAR crown radius. Regression model is indicated with the corresponding adj-R^2 and the number of detected trees.

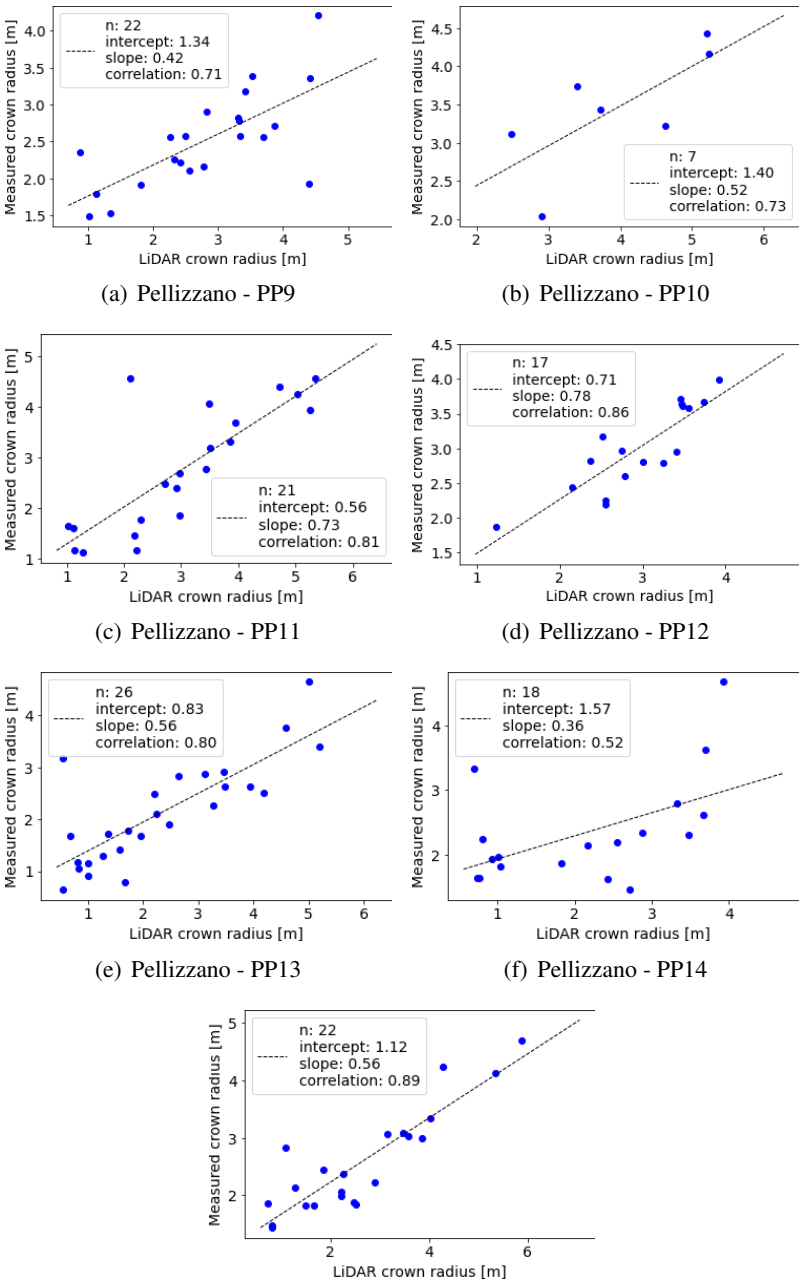

(a) Pellizzano - PP9 (b) Pellizzano - PP10

(c) Pellizzano - PP11 (d) Pellizzano - PP12

(e) Pellizzano - PP13 (f) Pellizzano - PP14

(g) Pellizzano - PP15

Figure C.31: Field measured crown radius of correctly detected trees plotted against LiDAR crown radius. Regression model is indicated with the corresponding adj-R^2 and the number of detected trees.

D

Graph-based fusion

In this annex, we present the preliminary result of data fusion at feature-level by using graph-based approach. So far, the scheme of feature selection presented in chapter 5 generates a higher overall accuracy than this approach.

Sommaire

D.1 Introduction

The workflow of the graph-based approach is presented in Figure D.1, it is based on the contribution given by Liao *et al.* [229]. The original approach uses as feature descriptors: the hyperspectral images (HI), the morphological profiles (MPs) derived from two principal components (PC) from HI and the DSM from LiDAR data. The inputs of our workflow are based on the HI, 25 vegetation indices derived from chapter 5 and the LiDAR features explained in the same chapter, in the subsection 5.3.4.

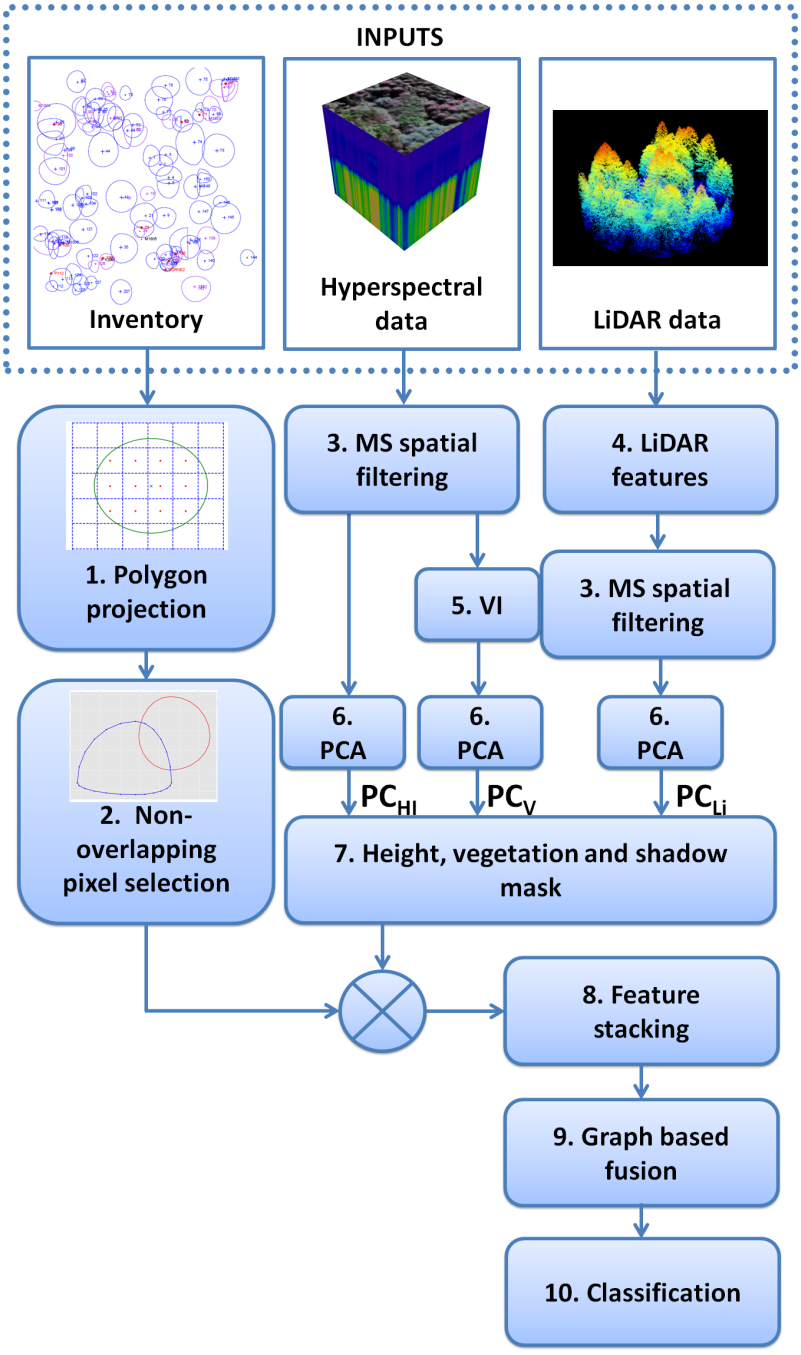

Figure D.1: Flowchart for integrating graph-based approach for tree species classification.

D.2 Assumption

We implement mean shift (MS) algorithm [262] to create local similarity among the pixels in HI and LiDAR features to enhance the classification results. According to [277], a strategy for reducing local noise and improving class separability can be implemented through the spatial filtering. Conventionally, a mean filtering is computed by moving a windows of 3×3 over each band. In [165], three circular neighborhoods of radius $r_f \in \{1.0, 3.0, 5.0\}$ m are applied to compute the mean value of every pixel in each band. Since the pixel center coordinate (x_c, y_c) is known, the pixels whose centers are inside of the circular neighborhood of each pixel, are selected for averaging the reflectance in each band. Finally, the three mean values of all pixel associated to each r_f are averaged.

In this annex, the spatial filtering is implemented through MS approach by using a spectral kernel based on the spectral angle between the spectral signatures. Since every pixel is evaluated, a circular neighborhood of radius r_f is used to filter the spectral signatures by considering the neighbor's information. Besides, an horizontal kernel given by a Gaussian function is also considered in the weighting process. For the LiDAR features, the similarity is given by the euclidean distance and the horizontal kernel. After performing MS over each feature set in each forest plot, we build our dataset to evaluate the overall accuracy by using random forests (RF). The overall accuracy for three radius r_f are presented in Table D.1. We noticed that the result obtained with $r_f = 1$ is better even than the original information for HI. For LiDAR information, we do not perceive a significant improvement.

Table D.1: Overall accuracy [%] of HI and LiDAR features after applying MS spatial filtering with three different r_f values.

r_f [m]	$\mathbf{D_{HI}}$	$\mathbf{D_{Li}}$
Original	70.6	63.9
1	**72.2**	**64**
3	69.5	63.7
5	63.6	60.5

D.3 Graph-based approach

After filtering the hyperspectral information and the LiDAR features with $r_f = 1$, we compute 25 VI in order to extract the PC from each feature set. The number of components is selected to be 25 for the purpose of providing same importance to the three sources of information. These components are stacked and then, these are the inputs of the graph-based fusion stage. The resulting features are classified in the RF classifier.

Although the overall accuracy is 2.8 points of percentage lower than the result obtained with feature selection, we notice that all species decreased their producer's accuracy with exception of the specie PIAB, which is the class with the greatest amount of samples. The graph-based approach creates local similarities by using KNN algorithm. A perspective in this work resides in understanding the way in which the edges of the graph are being defined to establish similarities.

Table D.2: Species classification results at pixel-level obtained by the integrating of HI and LiDAR features by using a graph-based approach

Ground truth							
Tree species	ABAL	FASY	PIAB	PIUN	Other	Total	Producer's acc. [%]
ABAL	1717	126	919	0	2	2764	62.1
FASY	62	1280	467	0	13	1822	70.3
PIAB	235	160	4098	25	11	4529	90.5
PIUN	1	0	54	211	0	266	79.3
Other	22	100	223	3	75	423	17.7
Total	2037	1666	5761	239	101	9804	
User's acc.	84.3	76.8	71.1	88.3	74.3		75.3

Apport de la fusion LiDAR - hyperspectral pour la caractérisation géométrique et radiométrique des arbres.

Fusion of 3D point clouds and hyperspectral data for the extraction of geometric and radiometric features of trees

Résumé

Cette thèse de doctorat porte sur la fusion de LiDAR et de données hyperspectrales pour caractériser les arbres forestiers individuels. L'idée maîtresse est d'améliorer les méthodes pour obtenir des informations forestières au niveau de l'arbre en extrayant des caractéristiques géométriques et radiométriques. Les contributions de ce travail de recherche reposent sur: i) un examen mis à jour des méthodes de fusion de données de LiDAR et des données hyperspectrales pour la surveillance des forêts, ii) un algorithme de segmentation 3D amélioré pour délimiter les couronnes d'arbres individuelles basé sur Adaptive Mean Shift (AMS3D) et un ellipsoïde modèle de forme de couronne, iii) un critère de sélection des caractéristiques basé sur le score aléatoire des forêts (RF), cross-validation à 5 folds et une fonction d'erreur cumulative pour la classification des espèces d'arbres forestiers. Les deux principales méthodes utilisées pour obtenir des informations forestières au niveau des arbres sont testées avec des données de télédétection acquises dans les Alpes françaises.

Mots-clés : LiDAR, forêt, hyperspectral, télédétection, AMS3D, classification.

Abstract

This PhD thesis deals with the fusion of LiDAR and hyperspectral data to characterize individual forest trees. The leading idea is to improve methods to derive forest information at tree-level by extracting geometric and radiometric features. The contributions of this research work relies on: i) an updated review of data fusion methods of LiDAR and hyperspectral data for forest monitoring, ii) an improved 3D segmentation algorithm for delineating individual tree crowns based on Adaptive Mean Shift (AMS3D) and an ellipsoid crown shape model, iii) a criterion for feature selection based on random forests (RF) score, 5-fold cross validation and a cumulative error function for forest tree species classification. The two main methods used to derive forest information at tree level are tested with remote sensing data acquired in the French Alps.

Keywords : LiDAR, forest, hyperspectral, remote sensing, AMS3D, classification.